



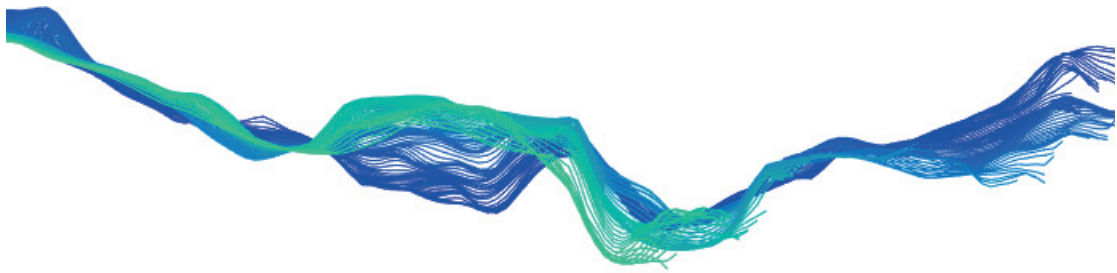
Max-Planck-Institut
für Meteorologie

MAX PLANCK
GESELLSCHAFT



International Max Planck Research School
on Earth System Modelling

Variability of the Contemporary Southern Ocean Carbon Fluxes and Storage



Lydia Keppler

Hamburg 2020

Hinweis

Die Berichte zur Erdsystemforschung werden vom Max-Planck-Institut für Meteorologie in Hamburg in unregelmäßiger Abfolge herausgegeben.

Sie enthalten wissenschaftliche und technische Beiträge, inklusive Dissertationen.

Die Beiträge geben nicht notwendigerweise die Auffassung des Instituts wieder.

Die "Berichte zur Erdsystemforschung" führen die vorherigen Reihen "Reports" und "Examensarbeiten" weiter.

Anschrift / Address

Max-Planck-Institut für Meteorologie
Bundesstrasse 53
20146 Hamburg
Deutschland

Tel./Phone: +49 (0)40 4 11 73 - 0
Fax: +49 (0)40 4 11 73 - 298

name.surname@mpimet.mpg.de
www.mpimet.mpg.de

Notice

The Reports on Earth System Science are published by the Max Planck Institute for Meteorology in Hamburg. They appear in irregular intervals.

They contain scientific and technical contributions, including Ph. D. theses.

The Reports do not necessarily reflect the opinion of the Institute.

The "Reports on Earth System Science" continue the former "Reports" and "Examensarbeiten" of the Max Planck Institute.

Layout

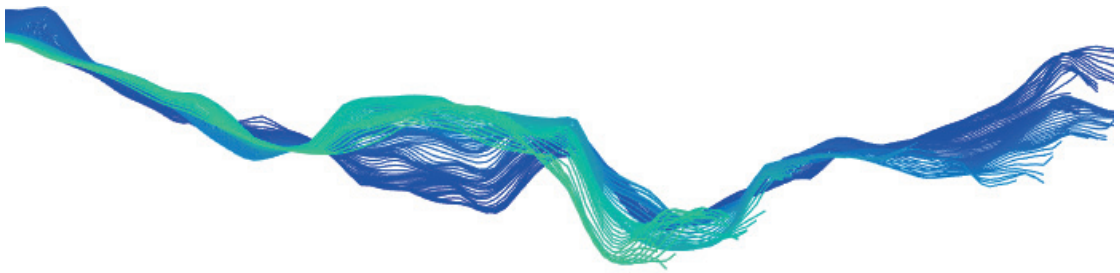
Bettina Diallo and Norbert P. Noreiks
Communication

Copyright

Photos below: ©MPI-M
Photos on the back from left to right:
Christian Klepp, Jochem Marotzke,
Christian Klepp, Clotilde Dubois,
Christian Klepp, Katsumasa Tanaka



Variability of the Contemporary Southern Ocean Carbon Fluxes and Storage



Lydia Keppler

Hamburg 2020

Lydia Keppler

aus Stuttgart, Deutschland

Max-Planck-Institut für Meteorologie
The International Max Planck Research School on Earth System Modelling
(IMPRS-ESM)
Bundesstrasse 53
20146 Hamburg

Universität Hamburg
Geowissenschaften
Meteorologisches Institut
Bundesstr. 55
20146 Hamburg

Tag der Disputation: 16. Juni 2020

Folgende Gutachter empfehlen die Annahme der Dissertation:

Dr. Peter Landschützer
Prof. Dr. Johanna Baehr

Vorsitzender des Promotionsausschusses:

Prof. Dr. Dirk Gajewski

Dekan der MIN-Fakultät:

Prof. Dr. Heinrich Graener

The figure on the front page depicts dissolved inorganic carbon at the surface ocean (y-axis) as a function of latitude (x-axis) and longitude (color). Although not bursting with useful information, it passes as a piece of modern art. A slightly modified version of this figure won the Clim*Art Contest of the 2019 MPI-M annual retreat.

“Humanity is currently enacting a narrative that nature is ours to abuse and exploit and pollute as we see fit, forgetting that we are a part of it. We are part of the web of life, and when we harm one part of that web, we harm ourselves. We urgently need a new narrative, where instead of hubris we have humility. Instead of rapacious destruction we have respect and stewardship. Instead of disconnection, we have deep connection - to nature, to each other, to ourselves, and to our future.”

Roz Savage

Abstract

Around half of the ocean's uptake of anthropogenic carbon from the atmosphere currently takes place in the Southern Ocean. However, the variability of this important carbon sink, as well as the drivers behind this variability, are still debated and it is unclear if the Southern Ocean will remain a carbon sink in the future. Until this PhD project, the development of the Southern Ocean carbon uptake at the air-sea interface was unknown based on observations beyond 2011. Furthermore, the seasonal to interannual variability of dissolved inorganic carbon (DIC) in the interior Southern Ocean had not been analyzed based on observations at regional scale. This dissertation closes these research gaps.

In the first part of my dissertation (Appendix A), I investigate the Southern Ocean carbon flux and its drivers until 2016 using an updated observation-based air-sea carbon flux estimate. After a stagnation period in the 1990s, and a reinvigoration in the 2000s, I find that the Southern Ocean carbon uptake weakened again since about 2011. My study reveals that the Southern Annular Mode, the dominant mode of climate variability in the southern high latitudes, is not the driver behind this weakening due to opposing effects that cancel each other out. Instead, regional shifts in surface wind velocity modulate the recent evolution of the carbon uptake in the Southern Ocean. In the second part (Appendix B), I develop a monthly climatology of global mapped interior DIC fields using a neural-network mapping approach. Using this new data product, I describe the seasonal carbon dynamics at global scale, including the phase and amplitude of the surface seasonal cycle, how deep seasonal signals are detectable, and I estimate the net community production. In the third part (Appendix C), I increase the temporal resolution of my new data product to resolve monthly fields from 2004 through 2017. I then re-focus on the Southern Ocean to investigate the interannual variability of DIC in the water column and determine the potential drivers behind this variability. Using this second new data product, I demonstrate that sub-surface DIC is subject to significant decadal fluctuations. These fluctuations extend to at least 500 m and could be linked to changes in the Meridional Overturning Circulation.

The methods and the publicly available data products I developed provide an opportunity for further analysis of the global carbon cycle. The findings from my PhD project represent an updated estimate of the carbon uptake and storage in the Southern Ocean and enable an improved description of the processes and drivers of variability. This knowledge forms an essential part of our understanding of the global carbon cycle and can, therefore, contribute to more accurate climate projections, forming an important basis for political decisions aimed at reducing carbon emissions.

Zusammenfassung

Im Südpolarmeer findet derzeit etwa die Hälfte der ozeanischen Aufnahme von anthropogenem Kohlenstoff aus der Atmosphäre statt. Über die Variabilität dieser wichtigen Kohlenstoffsенke sowie die Einflussfaktoren dieser Variabilität wird jedoch debattiert, und es ist unklar, ob das Südpolarmeer auch in der Zukunft eine Kohlenstoffsенke bleiben wird. Vor diesem Promotionsprojekt fehlte eine Abschätzung der atmosphärischen Kohlenstoffaufnahme des Südpolarmeers basierend auf Beobachtungsdaten die nach 2011 erhoben wurden. Des Weiteren wurde die saisonale und zwischenjährliche Variabilität des gelösten anorganischen Kohlenstoffs (DIC) im tiefen Südpolarmeer bisher noch nicht anhand von Beobachtungsdaten auf regionaler Ebene analysiert. Diese Dissertation schließt die bestehenden Forschungslücken.

Im ersten Teil meiner Dissertation (Anhang A) untersuche ich die ozeanische Kohlenstoffaufnahme aus der Atmosphäre und deren Einflussfaktoren im Südpolarmeer bis 2016 anhand aktualisierter Beobachtungsdaten, die an der Meeresoberfläche erhoben wurden. Nach einer Stagnationsphase in den 1990er Jahren und einem Wiedererstarken in den 2000er Jahren, ermittle ich, dass die Kohlenstoffaufnahme im Südpolarmeer seit ca. 2011 erneut nachgelassen hat. Meine Studie zeigt, dass der Southern Annular Mode, der dominante Modus von Klimaschwankungen in den südlichen hohen Breitengraden, nicht der Einflussfaktor hinter diesem Abschwächen der Senke ist, da sich gegensätzliche Effekte aufheben. Stattdessen kontrollieren regionale Verschiebungen der Oberflächenwindgeschwindigkeit die jüngste Entwicklung der Kohlenstoffsенke im Südpolarmeer. Im zweiten Teil (Anhang B) etabliere ich ein Verfahren, das es erlaubt, mithilfe neuronaler Netzwerke die globale Tiefenverteilung von gelöstem anorganischen Kohlenstoff als monatliche Klimatologie abzubilden. Mit diesem neu entwickelten Datenprodukt beschreibe ich die saisonale DIC-Dynamik auf globaler Ebene. Diese Beschreibung erstreckt sich auf die Phase und Amplitude des saisonalen Zyklus an der Oberfläche und dessen Tiefenausdehnung, sowie eine Abschätzung der Nettoproduktion von organischem Kohlenstoff durch marine Lebensgemeinschaften. Im dritten Teil (Anhang C) erhöhe ich die zeitliche Auflösung dieses Datenprodukts, um auch die zwischenjährlichen Veränderungen der monatlichen DIC-Felder von 2004 bis Ende 2017 aufzulösen. Für die inhaltliche Interpretation der neu generierten Datensätze lege ich den Schwerpunkt erneut auf das Südpolarmeer, um hier die zwischenjährliche Variabilität des gelösten anorganischen Kohlenstoffs in der Wassersäule zu beschreiben und die möglichen Einflussfaktoren für diese Variabilität zu bestimmen. Anhand dieses zweiten neuen Datenprodukts zeige ich, dass der gelöste anorganische Kohlenstoff unterhalb der Meeresoberfläche signifikanten

dekadischen Schwankungen unterliegt. Diese Schwankungen erstrecken sich mindestens über die oberen 500 m der Wassersäule und könnten mit Änderungen der meridionalen Umwälzzirkulation verbunden sein.

Die von mir entwickelten Methoden und öffentlich zur Verfügung gestellten Datenprodukte eröffnen diverse Möglichkeiten zur weiteren Analyse des globalen Kohlenstoffkreislaufs. Die Ergebnisse meines Promotionsprojekts stellen eine aktualisierte Abschätzung der Kohlenstoffaufnahme und -speicherung im Südpolarmeer dar und ermöglichen eine erheblich verbesserte Beschreibung der beteiligten Prozesse und Einflussfaktoren. Dieses Wissen ist ein wesentlicher Bestandteil unseres Verständnisses des globalen Kohlenstoffkreislaufs und kann somit zu genaueren Klimaprojektionen beitragen. Damit bilden die Befunde auch eine wichtige Grundlage für politische Entscheidungen, die auf die Reduzierung der Kohlenstoffemissionen abzielen.

Parts of this dissertation pre-published or intended for publication

Keppler, L. and P. Landschützer (2019). "Regional Wind Variability Modulates the Southern Ocean Carbon Sink". In: *Scientific Reports* 9, 7384. <https://doi.org/10.1038/s41598-019-43826-y>. **Appendix A**

Keppler, L., P. Landschützer, N. Gruber, S.K. Lauvset, I. Stemmler (in review). "Seasonal Carbon Dynamics in the Global Ocean based on a Neural-Network Mapping of Observations". *In review at Global Biogeochemical Cycles*. **Appendix B**

Keppler, L. and P. Landschützer (in prep.). "Temporary Reduction in Southern Ocean sub-surface Dissolved Inorganic Carbon". *To be submitted to Geophysical Research Letters*. **Appendix C**

Acknowledgments

I have received an incredible amount of support from many people, for which I am extremely grateful.

First, I would like to thank my main supervisor. Thank you, Peter Landschützer, for giving me this opportunity, your positive attitude, always having my back, and everything I learned from you. I also am extremely grateful for my co-advisors, Jochem Marotzke and Birgit Klein, for their invaluable input and support. Many thanks also to Johanna Baehr for her well-thought-out advice during our panel meetings. I could not have asked for better support and guidance from my advisory panel throughout my PhD.

I would also like to thank my colleagues and friends from the MPI-M, with special thanks to the Ocean Department, the OAS and DRO groups, the Journal Club and LunchBytes, and the IMPRS. I have been privileged to work with you all and am grateful for the many lessons learned, the interesting discussions and seminars, as well as the coffee breaks, lunches, Feierabendbiere, and other fun activities. Thank you also for all the administrative and moral support from Antje, Connie, Michaela, and Kornelia.

I am also very grateful for my co-authors—Niki Gruber, Siv Lauvset, and Irene Stemmler. It has been a fantastic experience to write a paper with you. I also want to thank the people that have provided feedback to this thesis—Laura, Rike, Jens, and Hauke. I am extremely grateful for your valuable contributions.

Last but not least, I want to thank my family and friends for their support and friendship. Our chats and meet-ups have meant a lot to me. Thank you for the laughs, discussions, and the reminders to focus on self-care. Thank you, Shupiwe, for your incredible support, moving to Hamburg with me, always believing in me, your editing, and your love. Finally, I want to thank my grandmother, Oma Evchen. Thank you for all the inspiration, your remarkable optimism, and your love. I got my passion for the ocean from you, and I know how proud you would have been.

Contents

Abstract	iii
Zusammenfassung	iv
Publications	vi
Acknowledgments	vii
Lists of Figures and Abbreviations	ix
Unifying Essay	1
1 Background	1
1.1 Basics of the oceanic carbon system	1
1.2 Biogeochemical and physical drivers	3
1.3 The relevance of the Southern Ocean	4
2 Current Knowledge and Research Gaps	4
2.1 Observations of the carbon system in the Southern Ocean	4
2.2 The mean Southern Ocean carbon uptake	6
2.3 Southern Ocean carbon uptake variability	8
2.4 Variability in interior Southern Ocean DIC	9
3 Machine Learning	10
3.1 Terminology	10
3.2 SOM-FFN	11
3.3 Approaches developed and used in this study	13
4 Summary of Key Results	14
4.1 Interannual variability of Southern Ocean carbon fluxes	14
4.2 Monthly climatology of global interior DIC	15
4.3 Interannual variability of interior Southern Ocean DIC	17
4.4 Drivers of variability at the surface and below	17
5 Outlook and Implications	18
Appendices	20
A Regional Wind Variability Modulates the Southern Ocean Carbon Sink	21
B Seasonal Carbon Dynamics in the Global Ocean based on a Neural-Network Mapping of Observations	37
C Temporary Reduction in Southern Ocean sub-surface Dissolved Inorganic Carbon	71
Bibliography	86
Declaration of Oath	94

List of Figures

1	Marine Carbon Chemistry	2
2	Location of recent Southern Ocean carbon measurements . . .	6
3	Temporal mean Southern Ocean carbon flux	7
4	Zonal mean Southern Ocean circulation	7
5	Evolution of the Southern Ocean Carbon sink until 2011 . . .	8
6	Schematic of SOM clustering	12
7	Schematic of a generic FFN configuration	13
8	Extension of the evolution of the Southern Ocean carbon flux	15
9	Seasonal characteristics of DIC	16
10	Change in DIC over time and depth	18
A.1	Recent Southern Ocean carbon sink variability	25
A.2	The SAM's effect on the Southern Ocean carbon sink	27
A.3	Physical sea surface properties and the carbon flux	29
A.4	Regional shifts in sea level pressure and surface winds	32
B.1	Ship measurements of DIC	41
B.2	Spatial distribution of DIC	49
B.3	Comparison with Lauvset	50
B.4	Comparison with HAMOCC (time-mean)	52
B.5	Seasonal cycle in climate regions	53
B.6	Amplitude and phase of the seasonal cycle	54
B.7	Regional response function	55
B.8	Comparison with HAMOCC (seasonal cycle)	56
B.9	Comparison with HOT time-series	57
B.10	Comparison with BATS time-series	58
B.11	Comparison with SOCCOM floats	59
B.12	Nodal depth of DIC	60
B.13	Spatial distribution of summer NCP	61
B_SI.1	Location and variability of SOM clusters	66
B_SI.2	Schematic of our FFN configuration	68
B_SI.3	Time or location as predictor	69
B_SI.4	Summary of validation tests	70
C.1	Change in DIC over time and depth	76
C.2	Temporal sub-surface reduction in direct DIC measurements .	77
C.3	Comparison with independent data	79
C.4	Physical drivers of the interior DIC	81
C_SI.1	Time-mean of DIC in the Southern Ocean	84
C_SI.2	Timeline of the recent SAM	85

List of Abbreviations

ACC	Antarctic Circumpolar Current
AOU	Apparent Oxygen Utilization
BATS	Bermuda Atlantic Time Series Study
BGC	Biogeochemical
CLIVAR	Climate Variability and Predictability
CMIP(5)	Coupled Model Intercomparison Project (phase 5)
CO ₂	Carbon Dioxide
DIC	Dissolved Inorganic Carbon
FFN	Feed-Forward Network
fCO ₂	Fugacity of CO ₂
GLODAP	Global Ocean Data Analysis Project for Carbon
HOT	Hawaii Ocean Time-Series
MLD	Mixed Layer Depth
MLRs	Multi-Linear Regressions
MOC	Meridional Overturning Circulation
MSE	Mean Squared Error
OSP	Ocean Station Papa
NCP	Net Community Production
pCO ₂	Partial Pressure of Carbon Dioxide
ΔpCO ₂	Difference between Oceanic pCO ₂ and Atmospheric pCO ₂
PF	Polar Front
RMSE	Root Mean Squared Error
SAM	Southern Annular Mode
SLP	Sea Level Pressure
SOCAT	Surface Ocean CO ₂ Atlas
SOCCOM	Southern Ocean Carbon and Climate Observations and Modeling project
SOMs	Self-Organizing Maps
SSS	Sea Surface Salinity
SST	Sea Surface Temperature
STF	Subtropical Front
WOA18	World Ocean Atlas 2018
WOCE	World Ocean Circulation Experiment
xCO ₂	Mole Fraction of Carbon Dioxide
ZW1/3	Zonal Wavenumber 1/3

Unifying Essay

This thesis is structured as a cumulative dissertation, where the Unifying Essay precedes three Appendices containing the research articles I produced as part of my PhD. The Unifying Essay first introduces my PhD project by providing the scientific background knowledge and then putting my research into the broader literature context, presenting the current knowledge and related research gaps. After describing some of the methods I developed and applied during this PhD, I present my main research findings and a brief overview of how this study may affect subsequent research and the implications of my findings.

1 Background

1.1 Basics of the oceanic carbon system

Of the carbon dioxide (CO_2) emitted annually by humans, currently, only about half accumulates in the atmosphere, whereas the land and ocean take up the rest. Specifically, the Global Carbon Budget (Friedlingstein et al., 2019) estimates, that between 2009 and 2018, the ocean took up $2.5 \pm 0.6 \text{ PgC yr}^{-1}$ from the atmosphere, which is approximately 23% of the annual anthropogenic emissions for that period (1 PgC = 1 petagram carbon = 10^{15} grams of carbon). Due to this oceanic uptake of anthropogenic carbon, the ocean plays an important mitigating role in climate change (Ciais et al., 2014).

The oceanic uptake of CO_2 from the atmosphere occurs at the air sea-interface (Fig. 1). When gaseous CO_2 dissolves in the ocean, the now aqueous CO_2 reacts chemically with water molecules (H_2O) and forms carbonic acid (H_2CO_3), which can dissociate twice into bicarbonate ions (HCO_3^-) and carbonate ions (CO_3^{2-}) (Sarmiento and Gruber, 2006; Zeebe and Wolf-Gladrow, 2001). These 'species' of inorganic carbon in seawater are collectively referred to as dissolved inorganic carbon (DIC). In its dissolved form, the carbon can be transported through currents and turbulent mixing (Heinze et al., 2015). However, the chemical equilibrium reactions described here, can occur in both directions and so, carbon can be taken up by the ocean and stored as DIC, but DIC can also outgas into the atmosphere.

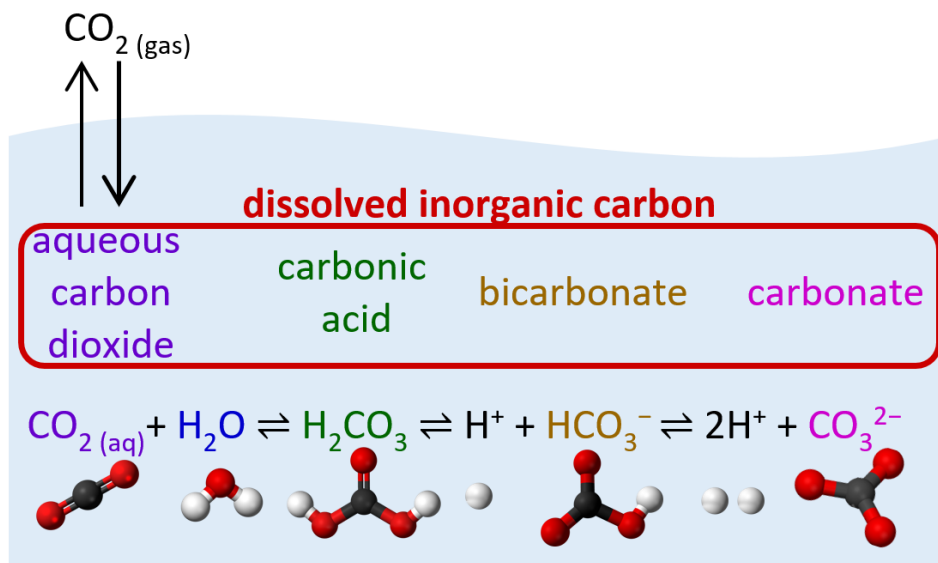


FIGURE 1: Schematic of marine carbon chemistry, demonstrating the uptake of atmospheric CO₂ and its reaction in seawater that form the different 'species' of carbon that form the DIC pool. Based on McNeil and Matsumoto (2019) and Sarmiento and Gruber (2006).

The magnitude and sign of the air-sea CO₂ exchange, also referred to as CO₂ flux, depend on various factors. Henry's Law states that "at a constant temperature, the amount of a given gas that dissolves in a given type and volume of liquid is directly proportional to the partial pressure of that gas in equilibrium with that liquid" (Henry and Banks, 1803). Technically, CO₂ does not behave like an ideal gas, and so the observed relationship between its temperature, volume, and pressure is not accurately described by the gas laws, such as Henry's law. Therefore, the fugacity of CO₂ (f_{CO_2}), which is the partial pressure of CO₂ (p_{CO_2}), corrected for the non-ideal behavior of CO₂, is commonly used for chemical thermodynamic calculations. However, due to the nearly ideal behavior of CO₂, f_{CO_2} and p_{CO_2} are numerically very similar, and so, both terms are commonly used to calculate the air-sea carbon flux (Takahashi et al., 1997). The gas exchange also depends on temperature, because CO₂ is more soluble in colder water than in warmer water, and on the kinetic gas transfer velocity, associated with the surface wind speed (Wanninkhof et al., 2013). Overall, the air-sea gas exchange of CO₂ (F_{CO_2}) can be expressed by Eq. 1, following Deacon (1977) and Sarmiento and Gruber (2006) :

$$F_{\text{CO}_2} = k_w \cdot S_{\text{CO}_2} \cdot \Delta p_{\text{CO}_2} \quad (1)$$

where k_w is the kinetic transfer velocity, S_{CO_2} the mainly temperature-driven solubility of CO₂, and Δp_{CO_2} the difference between the p_{CO_2} at the sea surface and the atmosphere above it.

As part of the natural carbon cycle, there are regions of carbon uptake, and regions of outgassing, which are nearly balanced in a steady-state climate. A slight disequilibrium still exists as the result of riverine input of carbon into the ocean; the ocean releases this additional carbon into the

atmosphere (Resplandy et al., 2018). In addition to the natural carbon cycle, the release of anthropogenic CO₂ into the atmosphere creates a partial pressure gradient that results in net oceanic uptake of carbon (Ciais et al., 2014).

Compared to the ocean, CO₂ in the atmosphere is relatively well-mixed, meaning that the concentration does not vary as much around the globe. However, different factors modulate the oceanic pCO₂, resulting in large variations that are orders of magnitude larger than the variations in atmospheric pCO₂. Subsequently, at the regional scale, the sea surface pCO₂ largely controls the sign and magnitude of the flux (Landschützer et al., 2014). Different physical and biogeochemical processes drive the variability in the air-sea carbon flux, and these are superimposed on the positive trend of increased carbon uptake due to the anthropogenic perturbation (Sarmiento and Gruber, 2006; Takahashi et al., 2002).

The positive effect of the oceans abating climate change by absorbing anthropogenic CO₂ (Friedlingstein et al., 2019) does not occur without negative side effects: the reaction of CO₂ in sea-water releases hydrogen ions (H⁺, Fig. 1), directly lowering the pH of the seawater (Sarmiento and Gruber, 2006; Zeebe and Wolf-Gladrow, 2001). Subsequently, additional DIC in the ocean lowers its pH, a process called ocean acidification (Doney et al., 2009). In more acidic water, calcifying organisms such as calcareous plankton, corals, and mollusks, struggle to produce calcium carbonate structures. Thus, ocean acidification endangers these species (Sarmiento and Gruber, 2006; Zeebe and Wolf-Gladrow, 2001). A decline or loss in calcifying organisms can then affect species on higher trophic levels and threaten the ecosystem stability (IPCC, 2013).

1.2 Biogeochemical and physical drivers

Biological activity affects the oceanic pCO₂ through photosynthesis, respiration, and remineralization. At the sea surface, organisms such as phytoplankton consume CO₂, forming organic carbon. This biological-driven process leaves the surface water under-saturated with inorganic carbon and allows for additional uptake. Sinking particles and fecal matter transport the organic carbon from the surface to the interior ocean. Conversely, remineralization, that is the break-down of organic matter by microbial organisms, and respiration by organisms ranging from bacteria to large mammals, dominate below the surface. Both remineralization and respiration release CO₂ back into the inorganic carbon pool (Sarmiento and Gruber, 2006). The overall biological draw-down of inorganic carbon is referred to as net community production (NCP) of organic matter. Changes in light availability and nutrients, for example through seasonal changes in insolation, riverine input of nutrients, or upwelling of nutrient-rich waters, affect the biological uptake of carbon (Heinze et al., 2015).

The main physical processes affecting the oceanic $p\text{CO}_2$, and thereby the carbon flux, are linked to ocean circulation and temperature. Upwelling brings deep carbon-rich water to the surface, resulting in a super-saturation of the surface water, leading to outgassing. Temperature affects the uptake of CO_2 ; for example, poleward flowing waters are cooled, increasing the solubility of CO_2 in these waters, thus under-saturating them and allowing for carbon uptake (Takahashi et al., 2002). Similarly, warming through seasonal forcing increases the oceanic $p\text{CO}_2$, which over-saturates the surface water, leading to outgassing, while cooling under-saturates the surface water, leading to carbon uptake (Sarmiento and Gruber, 2006).

1.3 The relevance of the Southern Ocean

The Southern Ocean is a key region of both carbon uptake and outgassing, and variability on various timescales considerably alters the mean field in this region. In pre-industrial times, the outgassing in upwelling regions in the Southern Ocean dominated over the carbon uptake, and so, the Southern Ocean was a net carbon source to the atmosphere (Gruber et al., 2009). However, due to the anthropogenic perturbation of the carbon cycle, the mean concentration gradient between the ocean and the atmosphere has changed direction, resulting in net carbon uptake. The Southern Ocean is the only basin that has turned from being a net carbon source in pre-industrial times, to a net carbon sink at present.

The Southern Ocean covers about 1/3 of the world's ocean, but approximately 1/2 of the oceanic uptake of anthropogenic carbon takes place in this region (Landschützer et al., 2016) and approximately 40% of the anthropogenic carbon that was stored in the ocean until 2008 was taken up in the Southern Ocean (Khatiwala et al., 2009). In the following section, I will focus on the processes dominating the air-sea carbon fluxes and storage in this dynamic region.

2 Current Knowledge and Research Gaps

2.1 Observations of the carbon system in the Southern Ocean

The Southern Ocean is a historically under-sampled region due to its remote location, and cold, windy, and rough weather conditions (Rintoul et al., 2012). In addition, excessive cloud cover and darkness in the high southern latitudes in austral winter render optical satellite data unavailable in this region (Pope et al., 2017). However, the number of available in-situ measurements of carbonate system parameters, such as $p\text{CO}_2$, DIC, pH, and alkalinity, has increased substantially in recent years due to a collective effort in the scientific community.

For the sea surface, the Surface Ocean CO_2 Atlas (SOCAT, Bakker et al., 2016) compiles and quality controls measurements from global underway ships, as well as fixed moorings and drifting buoys (Fig. 2a). The large

majority of these measurements are collected from programs such as Voluntary Observing Ships and among other variables, this database contains $p\text{CO}_2$ data that are used to compute the air-sea carbon flux. Most of the SOCAT measurements are taken autonomously using an equilibrator with a continuous sea-water flow (Bakker et al., 2016). Here, the $p\text{CO}_2$ is not measured directly, but the mole fraction of CO_2 ($x\text{CO}_2$ in parts per million) is measured, from which the $p\text{CO}_2$ (in μatm) can be inferred.

For the water column, the Global Ocean Data Analysis Project for Carbon (GLODAP, Olsen et al., 2019; Key et al., 2015) compiles and quality controls global ship measurements of carbonate system parameters at depth (Fig. 2b). The DIC is directly measured using bottled sea-water samples that are analyzed in the laboratory. There are some research cruises as part of GLODAP that did not measure the DIC directly; there, the DIC was calculated based on pH and alkalinity measurements from bottled samples. As the system of measuring DIC is not autonomous, there are substantially fewer measurements of DIC available than of the surface carbon parameters, such as $p\text{CO}_2$ (Fig. 2). However, locations with measurements have often been sampled multiple times through the repeat hydrography surveys that include the World Ocean Circulation Experiment (WOCE, <http://woceatlas.ucsd.edu/>) in the 1990s and CLIVAR (<http://www.clivar.org/>) since the 2000s (Talley et al., 2016).

Since 2014, Argo floats equipped with biogeochemical sensors, as a new type of in-situ observing platform, have substantially increased the number of carbon measurements in the Southern Ocean. As part of the Southern Ocean Carbon and Climate Observations and Modeling project (SOCCOM, <https://socom.princeton.edu/>, Fig. 2c), these robotic floats measure temperature, conductivity (for salinity), pressure (for depth), pH, oxygen, nitrate, and bio-optics. The DIC can then be calculated using the CO_2SYS analysis tool (Heuven et al., 2011) with pH measurements from the floats and total alkalinity estimated, for example, with temperature and salinity measurements and the LIAR algorithm (Carter et al., 2018). Approximately 200 of these autonomous floats have been deployed in the Southern Ocean to complement shipboard measurements. In the four years from 2014 through 2017, the SOCCOM floats have already considerably increased the spatio-temporal resolution of carbon measurements in the Southern Ocean (Fig. 2).

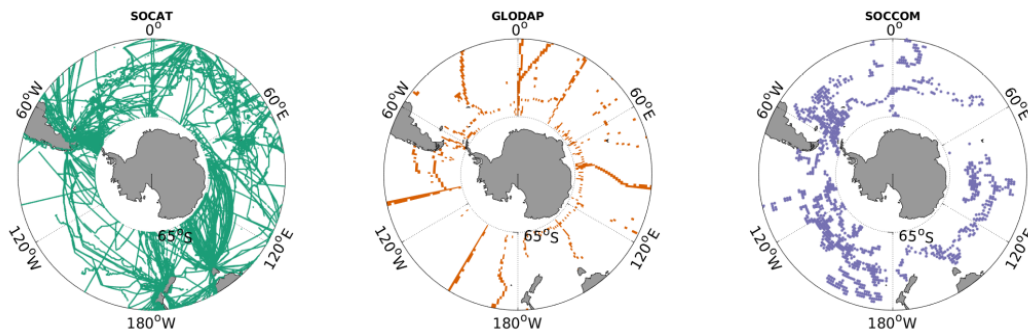


FIGURE 2: Location of recent carbon measurements in the Southern Ocean between 35°S and 65°S. (a) SOCATv2019 (at the surface, from 2004 through 2017); (b) GLODAPv2.2019 (at 10 m, from 2004 through 2017); (c) SOCCOM floats (at 10 m, from 2014 through 2017).

2.2 The mean Southern Ocean carbon uptake

Although the available measurements have helped to understand the mean processes in the Southern Ocean, recent studies have demonstrated that the Southern Ocean is not zonally uniform and many processes in this region occur in 'hot spots' (Rintoul, 2018). For example, the downward transport of anthropogenic carbon tends to cluster in some key subduction regions within the Southern Ocean (Sallée et al., 2012). Further, dominant fronts in the Southern Ocean create inter-frontal zones with distinctly different physical and biogeochemical properties (Freeman et al., 2016; Orsi et al., 1995) (Fig. 3).

Different, often opposing, processes affect the carbon uptake in the Southern Ocean (Fig. 3-4). A unique feature in this region is the Antarctic Circumpolar Current (ACC), which flows eastward near the Polar Front, unhindered by any continents. Northward Ekman transport at the ACC creates a divergence of surface waters, resulting in the upwelling of aged, carbon-rich water to the surface, causing outgassing around the ACC (Lovenduski et al., 2015). North of the ACC, poleward flowing warm waters mix with the cold subpolar waters; the cooling of these warm waters under-saturates them, allowing for carbon uptake. This water is then subducted north of the Subtropical Front and transported northward (Takahashi et al., 2002). In addition, near the Antarctic coast, freezing sea-water forms the cold and saline Antarctic Bottom Water through brine rejection during sea-ice formation (Talley et al., 2011). As this dense water mass cools, it under-saturates with carbon, allowing for carbon uptake; it then sinks, transporting DIC downward. Overall, the Southern Ocean currently takes up approximately 1 PgC yr^{-1} (Landschützer et al., 2016, Fig. 3).

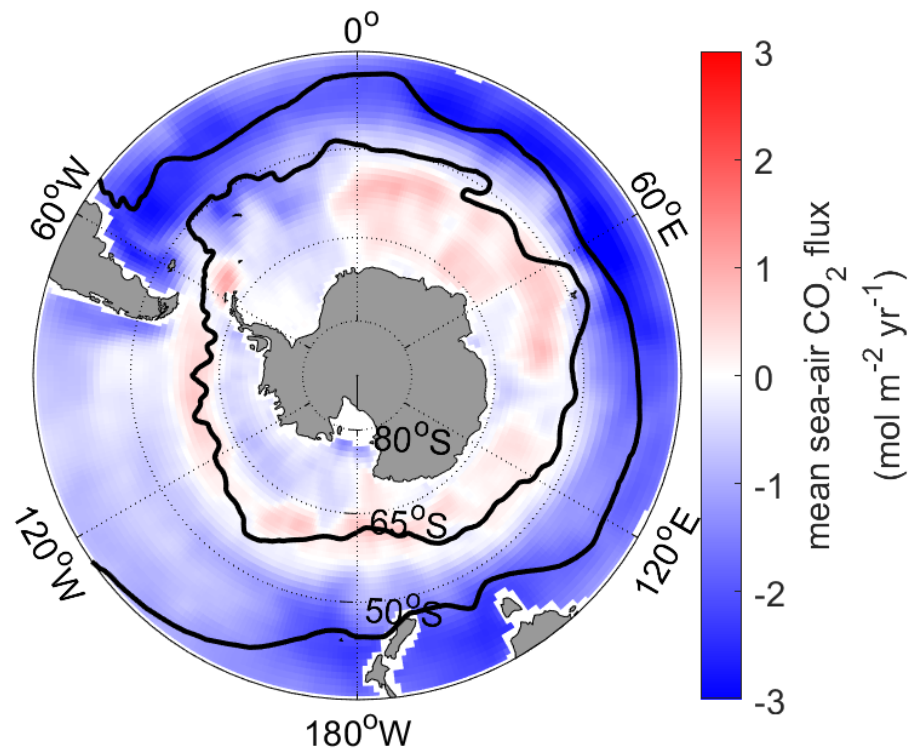


FIGURE 3: Temporal mean Southern Ocean carbon flux from 1982 through 2016 (blue: oceanic carbon uptake; red: outgassing). The Polar Front (~55°) and the Subtropical Front (~40°S) from Orsi et al., 1995 are illustrated as black lines. The air-sea carbon flux data from Landschützer et al. (2014) was used to produce this Figure.

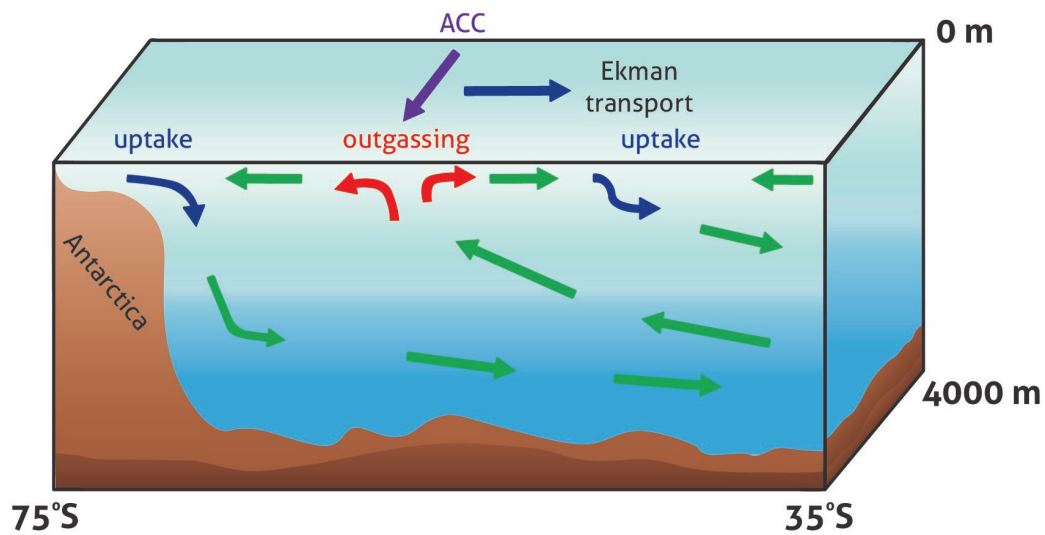


FIGURE 4: Simplified zonal mean circulation and carbon fluxes in the Southern Ocean. See in-text description. Modified from Talley et al. (2011).

2.3 Southern Ocean carbon uptake variability

While the processes involving the mean Southern Ocean carbon sink are generally well understood, the variability of these processes is not. Recent studies of the CO₂ uptake in the Southern Ocean have suggested a large carbon sink variability on interannual to decadal timescales, which is not captured by models (Frölicher et al., 2015) and the physical processes and drivers contributing to this variability in the various sectors of the Southern Ocean are still debated (DeVries et al., 2017; Landschützer et al., 2015; Le Quéré et al., 2007).

A study by Le Quéré et al. (2007) found that in the 1990s, the net Southern Ocean carbon uptake was not increasing any longer, but had stagnated despite the continued atmospheric increase in CO₂, causing concern that this crucial carbon sink had saturated. Nearly a decade later, Landschützer et al. (2015) found that between the early 2000s and 2011, the Southern Ocean carbon sink had reinvigorated and was taking up as much carbon from the atmosphere again as would be expected based on the atmospheric increase (Fig. 5). Observation-based estimates of the net carbon uptake in the Southern Ocean beyond 2011 had not been established until this PhD thesis. Consequently, in Appendix A, I answer the following Research Question:

A.1 How has the Southern Ocean carbon sink developed after 2011?

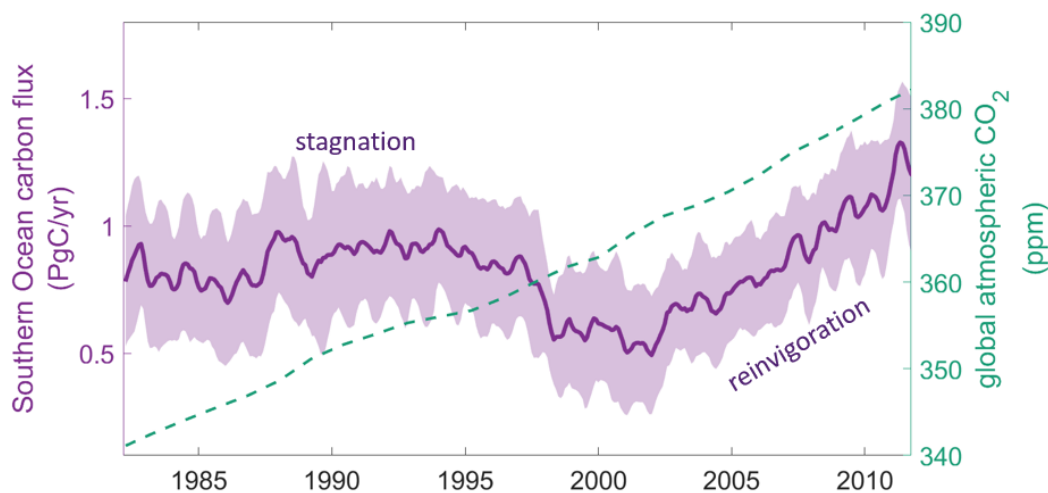


FIGURE 5: The evolution of the integrated air-sea carbon flux in the Southern Ocean between 35°S and the Antarctic coast from 1982 through 2011 (purple, left y-axis), illustrating the mean (solid line) and one standard deviation around the mean (shading). Here, larger numbers mean more oceanic uptake. The dashed green line (right y-axis) demonstrates the annual global mean atmospheric marine surface CO₂ over the same time period. Data used to produce this Figure: air-sea carbon flux data from Landschützer et al. (2014), seasonal cycle removed and ESRL globally averaged marine surface annual mean data from https://www.esrl.noaa.gov/gmd/ccgg/trends/gl_data.html.

Several different processes have been proposed as potential drivers for this large interannual to decadal variability. The Southern Annular Mode (SAM), defined as the zonal pressure difference between 40°S and 65°S, is the dominant mode of climate variability in the southern high latitudes (Marshall, 2003). There has been a positive trend in the SAM in recent decades, causing a strengthening and poleward shift of the westerly winds (Hall and Visbeck, 2002). These strengthened winds lead to enhanced outgassing which Le Quéré et al. (2007) argued led to the stagnation of the net Southern Ocean carbon uptake in the 1990s. However, the positive trend in the SAM has continued beyond the stagnation period, but the Southern Ocean carbon sink did not continue to stagnate. Another proposed driver of the Southern Ocean carbon sink variability is based on recently observed changes in the upper Meridional Overturning Circulation (MOC, DeVries et al., 2017). That study argued that a slow-down in the MOC had led to an overall increase in oceanic carbon uptake in the 1990s through less outgassing of natural carbon. That weakening was followed by a stronger MOC in the 2000s, which decreased the net carbon uptake through enhanced outgassing. In addition, the reinvigoration in the 2000s has also been also linked to a zonally asymmetric atmospheric circulation that enhanced the CO₂ uptake in that period (Landschützer et al., 2015). Gregor et al. (2018) argued that biological activity drives the Southern Ocean carbon sink variability in austral summer, and wind stress in austral winter. Bronselaer et al. (2020) found that besides the positive trend in the SAM, increased melting of the Antarctic ice sheet in recent years has led to increases in oceanic carbon content in the water column. The relative importance of the potential drivers of the carbon uptake variability in the Southern Ocean is, however, still debated. Thus, in Appendix A, I address the following Research Question:

A.2 What are the drivers behind the recent interannual variability of the Southern Ocean carbon sink?

2.4 Variability in interior Southern Ocean DIC

Previous studies of changes in the oceanic carbon at depth have focused on the uptake of anthropogenic carbon and the decadal changes thereof (Clement and Gruber, 2018; Gruber et al., 2019b; Khatiwala et al., 2009; Sabine et al., 2004). Most recently, Gruber et al. (2019b) found that although the Southern Ocean took up approximately 1 PgC yr⁻¹, between 1994 and 2007, only approximately 0.6 PgC yr⁻¹ was stored in this region as DIC, while the rest was transported northward, leaving the Southern Ocean (DeVries, 2014; Gruber et al., 2019a; Mikaloff Fletcher et al., 2006).

Due to different processes being dominant in sub-regions of the Southern Ocean, regional studies taking mapped fields into consideration are necessary to fully reflect the different processes in the Southern Ocean. This study is the first observation-based study that includes the Southern Ocean at regional scale to investigate the temporal changes in DIC on time-scales

shorter than decadal, or changes in contemporary (natural + anthropogenic) DIC on any time-scale. Subsequently, in Appendices B and C, I answer the following Research Questions:

B.1 Can we map time-varying fields of DIC using sparse ship data to create a monthly climatology?

C.1 Can we map time-varying fields of DIC in the Southern Ocean at interannual monthly resolution?

Knowing about the changes in Southern Ocean DIC allows for an analysis of these changes, thereby contributing to our collective understanding of the global carbon cycle and the processes involved. Thus, in Appendix C, I delve into the data estimate of monthly DIC from 2004 through 2017 to answer the following Research Questions:

C.2 What is the extent of the variability of DIC in the water column?

C.3 What are the drivers behind the variability of DIC at the surface and below?

3 Machine Learning

As traditional interpolation methods, such as optimal interpolations, had been unable to resolve time-varying global mapped fields of surface carbon measurements, various interpolation and mapping methods have recently emerged, ranging from statistical auto-correlation techniques to machine learning approaches (Jones et al., 2015; Landschützer et al., 2013; Rödenbeck et al., 2015). In the field of machine learning, computational algorithms are statistically trained to classify, predict, cluster, or discover patterns in a dataset (Reichstein et al., 2019). Neural networks, a sub-branch of machine learning, can be used to reconstruct and map data that have spatio-temporal gaps (Gardner and Dorling, 1998).

3.1 Terminology

As the terms *gridded*, *interpolated*, and *mapped data* are often used interchangeably, I first briefly define them here, following the work by Lauvset et al. (2016).

Observations are often projected onto a regular grid, using binning and averaging, but without interpolation or calculations to fill empty grid cells. One such example is the gridded dataset of SOCAT data (Bakker et al., 2016) by Sabine et al. (2013). In a classical interpolation, the original observations do not change, and values are only added between the data gaps, hence there are no residuals in interpolations. One such example is the vertical interpolation commonly performed to bring ship-based observations onto

standard depth levels and Cubic Hermite functions are commonly used for these interpolations. In a mapped data product, observational gaps are filled using some form of interpolation or other mapping approaches to produce a gap-filled map. In some mapping approaches, such as the one described below, each grid cell, including those containing the original gridded observations, is computed. In such an approach there are residuals between the observations and the mapped values, which are set to be minimal.

3.2 SOM-FFN

Landschützer et al. (2013) developed a two-step neural network mapping approach to overcome the low spatio-temporal density of surface carbon measurements. In their SOM-FFN approach, the authors first use self-organizing maps (SOMs) to cluster the oceans into regions of similar biogeochemical properties, and in a second step, they run a feed-forward network (FFN) in each of the clusters to compute and apply the statistical relationship between $p\text{CO}_2$ and specific predictor data. The predictor data are more numerous and spread more evenly around the world than the target data ($p\text{CO}_2$), thereby helping to overcome the low spatio-temporal density of surface carbon measurements.

SOMs are a type of unsupervised machine learning technique to cluster data (Kohonen, 1989; Kohonen, 2001). During unsupervised learning, the algorithm looks for patterns in a data set, that were not labeled as such before. The SOM-clustering process is as follows (Fig. 6): the variables that are to be clustered—in the schematic temperature and salinity—are usually first normalized (Fig. 6a) and the user prescribes the number of desired clusters (in the schematic: three). The algorithm begins by placing proposed cluster centers randomly in the grid space around the input variables and calculates the Euclidean distance between the input variables and their closest cluster center (Fig. 6b). Next, the centers are iteratively moved around to minimize the sum of the distances of all the input variables to their closest cluster center (Fig. 6c-f). The user prescribes a maximum number of iterations, but the algorithm stops before that number is reached if the distances cannot be minimized further (Fig. 6f).

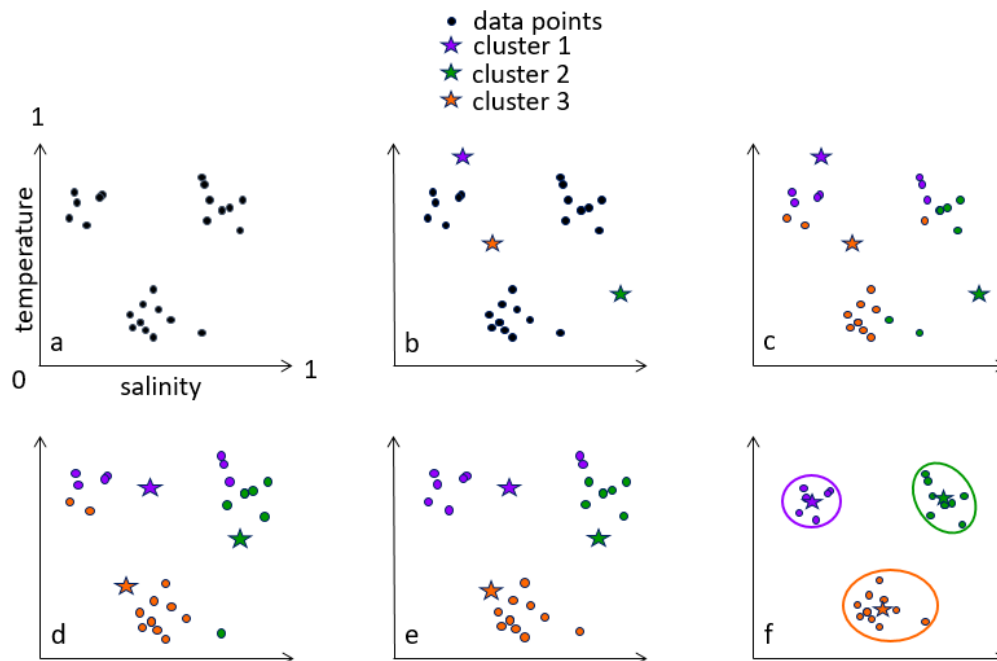


FIGURE 6: Schematic of the SOM clustering process. The x and y-axes are normalized salinity and temperature for each subfigure (a-f), extending from 0 to 1. In c-f, the color of the data points matches the color of their closest cluster center. See in-text for an explanation of the SOM-clustering process. Inspired by Luis Serrano ('A Friendly Introduction to Machine Learning', <https://www.youtube.com/watch?reload=9&v=IpGxLW0IZy4>).

FFNs are a type of supervised machine learning technique used to approximate a function describing the relationship between variables (Gardner and Dorling, 1998). During supervised learning, the algorithm uses a training data-set from which it can learn a statistical pattern, which it then applies. FFNs have similar purposes as multi-linear regressions (MLRs): they approximate and apply the statistical relationship between multiple predictor and target variables. One of the differences to MLRs is that in the neural network method, the relationships are allowed to be non-linear, potentially capturing the complex relationships between the variables more accurately (Olden and Jackson, 2002).

During the training-step of an FFN that is used for mapping (Fig. 7), the predictor data (mapped variables) are connected to the target data (a gridded variable with gaps) by a transfer function that describes their statistical relationship. The set-up in Fig. 7 has two layers, where the predictors are first connected to a chosen number of neurons by a transfer function (e.g., a sigmoid function), and then these neurons are connected by a second transfer function (e.g., a linear function) to the target data and the network multiplies each connection with random initial weights. The output produced with the initial set-up is then compared to the target data, and the mean squared error (MSE) of the residuals is calculated. The training step is then iteratively repeated, where the connection weights are adjusted in each iteration until the MSE reaches a minimum.

To avoid over-fitting, usually only a subset of the training data is used (e.g., 80%), while the remaining data are used for validation. During this early-stopping approach, the network stops when the MSE between the training and the validation data does not decrease any more. Next, the network applies the learned relationship in combination with the mapped predictor data to infer the target data on the same map grid as the predictor data.

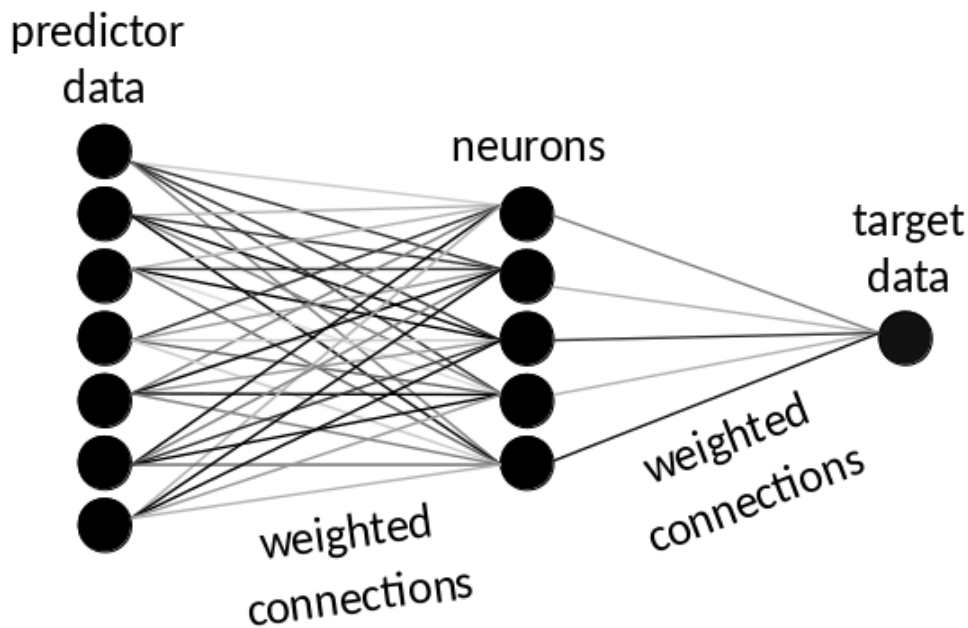


FIGURE 7: Schematic of a generic 2-layer FFN configuration. Illustrating 7 predictor variables, that are each joined to five neurons by weighted connections. Each of the neurons is then joined to the target variable by weighted connections (weight illustrated by the intensity of the grayscale). Based on Olden and Jackson (2002) and Hsieh (2009).

3.3 Approaches developed and used in this study

To investigate the continued development of the Southern Ocean carbon sink after 2011, I use an updated version of the mapped air-sea CO₂ product by Landschützer et al. (2015), which is based on the SOM-FFN approach and extends until December 2016 (Appendix A).

Next, I developed a monthly climatology of global fields of DIC in the interior ocean, from the surface until 2000 m (Appendix B). As the SOM-FFN had been demonstrated to work at the surface, I built on that approach, extending the method from three dimensions (latitude, longitude, and month) to four dimension (latitude, longitude, month, and depth). I describe the SOM-FFN approach in more detail in Appendix B, along with the data used and various validation tests I conducted with independent data.

To investigate the interannual variability of DIC in the interior Southern Ocean, I further built on the method from Appendix B, increasing the temporal resolution to create a second data set, which consists of global mapped fields of interior DIC with monthly temporal resolution from 2004 through 2017, from the surface until 500 m (Appendix C).

In my SOM-FFN set-up, the target data of the FFN are the sparse ship measurements of DIC, while the predictor data are better-constrained variables that are related to DIC (e.g., temperature, salinity, dissolved oxygen, and nutrients). These variables exist at a higher spatio-temporal density than DIC measurements, and so, mapped time-varying data products of these variables have been produced using traditional interpolation techniques, such as optimal interpolations.

Mapping the interior DIC poses additional challenges compared to mapping the surface $p\text{CO}_2$. First, the DIC measurements at depth are even sparser than surface carbon measurements (Fig. 2). Second, while many predictors can be used at the surface, for example, from satellite observations, very few variables are available as predictors at depth. Despite these challenges, the method passes relevant validation tests and can adequately map the time-varying DIC fields, as demonstrated in Appendices B and C.

4 Summary of Key Results

4.1 Interannual variability of Southern Ocean carbon fluxes

After a stagnation of the Southern Ocean carbon sink in the 1990s and a reinvigoration in the early 2000s, I demonstrate in Appendix A, that this globally important carbon sink has weakened again since 2011 (Fig. 8). I found that, although previously the uptake in the three sectors of the Southern Ocean—the Atlantic, Pacific, and Indian Ocean sectors—had followed the same trend, from 2008 the sectors differ: while the uptake in the Atlantic and Indian sectors weakened, the uptake in the Pacific sector stagnated during this period. This answers my Research Question A.1: ‘How has the Southern Ocean carbon sink developed after 2011?’

I further demonstrate in Appendix A, that locally within the Southern Ocean, the SAM plays an essential role on the carbon uptake variability over the last 35 years, where positive SAM phases enhance outgassing in upwelling regions, and enhance carbon uptake in subduction regions. These opposing local effects, however, cancel each other out, leading to a net-zero effect of the SAM on the overall Southern Ocean carbon trends. Instead, I find that regional shifts in sea level pressure and the induced changes in surface wind velocity modulate the recent Southern Ocean carbon sink. This answers Research Question A.2: ‘What are the drivers behind the recent interannual variability of the Southern Ocean carbon sink?’

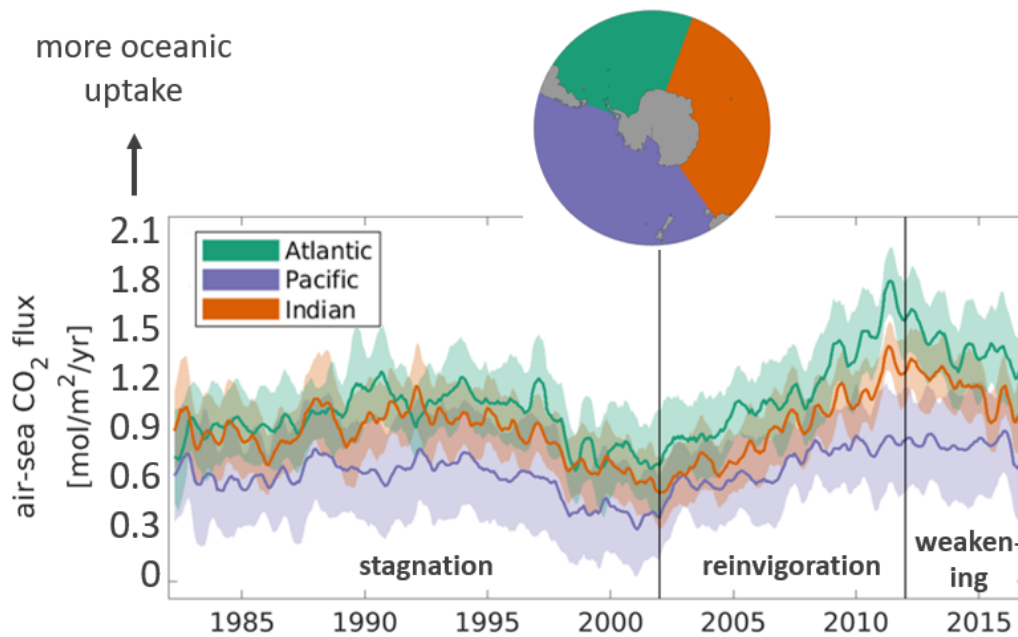


FIGURE 8: Extension of the evolution of the Southern Ocean carbon flux per unit area, between 35°S and the Antarctic coast from 1982 through 2016 in the Atlantic (green), Pacific (purple), and Indian (orange) sectors.

4.2 Monthly climatology of global interior DIC

In Appendix B, I demonstrate that it is possible to map time-varying fields of interior DIC using sparse ship data. I created a monthly climatology of DIC from the sea-surface to 2000 m, using a 2-step neural-network-based mapping technique and DIC measurements from the GLODAPv2.2019 data product. Various tests with an ocean biogeochemistry model, and with independent observations that were not used to train the network demonstrate that the method can capture the seasonal cycle of DIC at global scale with an average root mean squared error (RMSE) of approximately 20 $\mu\text{mol kg}^{-1}$. This answers my Research Question B.1: 'Can we map time-varying fields of DIC using sparse ship data to create a monthly climatology?'

In addition to answering the main research questions in this dissertation, I also describe the global seasonal carbon dynamics using my new data product in Appendix B. As the largest signal in the changes in DIC is the seasonal cycle, it considerably affects the amount of carbon taken up by the ocean. A study by Mongwe et al. (2018) demonstrated that the Coupled Model Intercomparison Project phase 5 (CMIP5) models disagree on the phase and amplitude of Southern Ocean inorganic carbon, while Nevison et al. (2016) highlighted that the seasonal carbon dynamics in the CMIP5 models significantly affect their climate projections. Thus, understanding the seasonal carbon dynamics and the underlying processes forms an important part of climate research.

The phase of the surface seasonal cycle is approximately opposite in the two hemispheres and the highest surface DIC concentrations occur in hemispheric spring (Fig. 9a). In these months, the mixed layer tends to be deepest (Holte et al., 2017), bringing carbon-rich waters to the surface. I find the amplitude of this surface seasonal cycle to be between 5 and 20 $\mu\text{mol kg}^{-1}$ throughout most of the global oceans (Fig. 9b) and the largest amplitudes are in the northern high latitudes of the Pacific and Atlantic Oceans. Opposing processes of photosynthesis near the surface and respiration and remineralization below, result in a phase shift of the seasonal cycle of DIC with depth. The surface seasonal pattern described above extends to a depth of several hundred meters in the subtropics and less than 50 m in the tropics. Below that depth, named the DIC nodal depth, the seasonal cycle tends to have a shifted phase compared to the surface, but with a smaller amplitude (Fig. 9c). Using the change in DIC concentration between hemispheric spring and autumn, I estimate the summer NCP in the water column (Fig. 9d). I find the largest summer NCP in the North Atlantic and the Labrador Sea and estimate that globally, the summer NCP is $6.1 \pm 0.9 \text{ PgC}$.

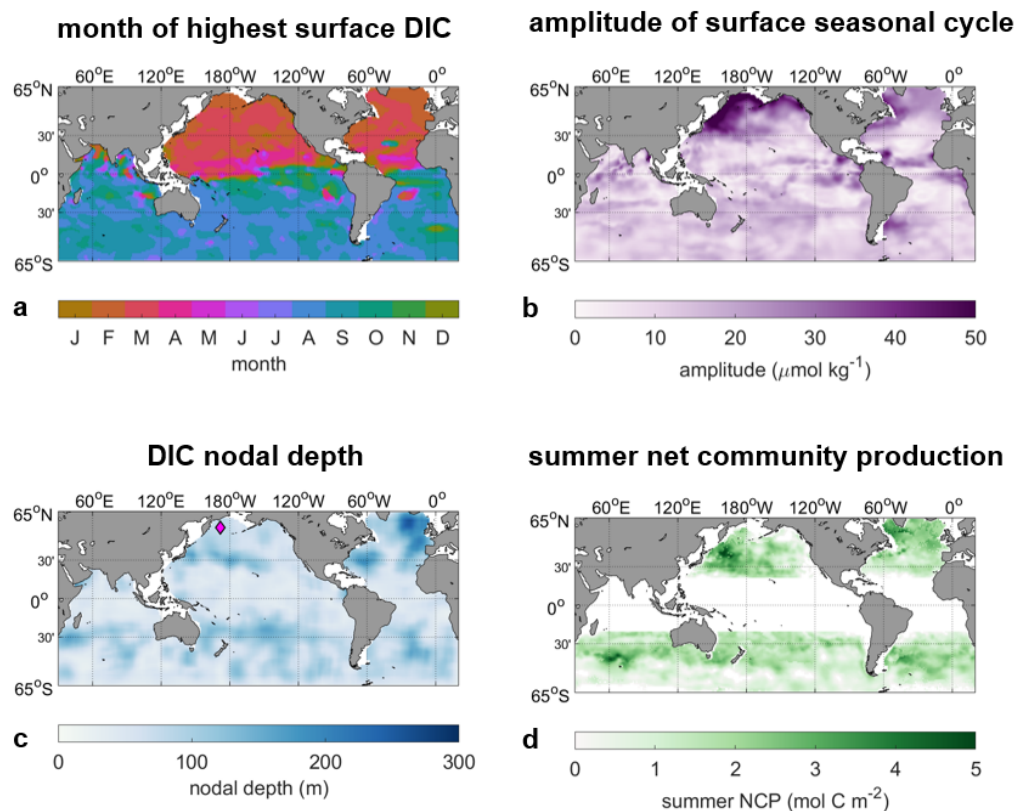


FIGURE 9: Spatial distribution of the seasonal characteristics of seasonal DIC, depicting the month with the highest DIC values at the surface (a), the amplitude of the surface seasonal cycle of DIC (b), the DIC nodal depth(c), and the summer net community production (d). Modified from Appendix B.

4.3 Interannual variability of interior Southern Ocean DIC

In Appendix C, I build on the method from Appendix B, extending the temporal resolution to monthly mapped fields of DIC at global scale from 2004 through 2017. Focusing on the Southern Ocean, I test this new data estimate with independent data and find that the method adequately maps the Southern Ocean DIC, capturing its mean, trend, and interannual variability, illustrated by the RMSE of $24 \mu\text{mol kg}^{-1}$ between my DIC estimate and the DIC calculated from SOCCOM floats. In addition, tests with synthetic data from the ocean biogeochemistry model HAMOCC (Ilyina et al., 2013; Mauritsen et al., 2019) demonstrate that our estimate can reconstruct the model field with an RMSE of $8 \mu\text{mol kg}^{-1}$. This answers Research Question C.1: 'Can we map time-varying fields of DIC in the Southern Ocean at interannual monthly resolution?'

Analyzing this new data estimate of monthly mapped DIC fields, I find that the surface DIC has a very weak interannual variability compared to the air-sea CO_2 flux, and the strongest signal here is the anthropogenically-driven positive trend. Below the surface, my analysis reveals a large temporary sub-surface reduction in DIC from 2004 until the year 2009, which is followed by a recovery until 2012 (Fig. 10). This reduction is the strongest south of the Polar Front, i.e., near the Antarctic coast, and extends to 500 m. This answers Research Question C.2: 'What is the extent of the variability of DIC in the water column?'

I present multiple lines of evidence that link this temporary reduction in sub-surface DIC to recent changes in the MOC. A weakening overturning circulation in the 2000s led to less upwelling of Southern Ocean DIC, creating the sub-surface reduction, allowing for additional carbon uptake at the surface. While we do not know the evolution of the MOC after 2009, it is likely that enhanced upwelling aided the recovery of the sub-surface reduction in DIC, and weakened the carbon uptake at the surface. This answers Research Question C.3: 'What are the drivers behind the variability of DIC at the surface and below?'

4.4 Drivers of variability at the surface and below

In Appendix A, I find that the SAM does not have an overall effect on the recent variability in the air-sea carbon uptake, integrated over the whole Southern Ocean. Conversely, in Appendix C, I attribute the variability in sub-surface DIC to changes in the MOC, which is tied to the SAM. These findings demonstrate that in positive SAM phases, the regional effects of enhanced outgassing in regions of upwelling is counter-balanced by enhanced uptake elsewhere at the surface, which creates the overall net-zero effect of the SAM on the Southern Ocean carbon flux. However, below the surface, the reduced upward transport is visible in the DIC pool, as demonstrated in Appendix C.

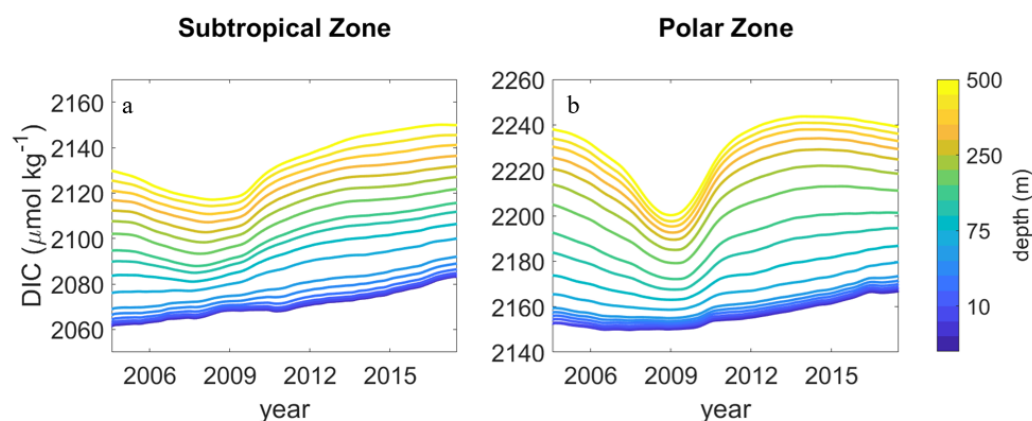


FIGURE 10: Changing DIC concentration with time (x-axis) and depth (color) for the Subtropical Zone (a) and the Polar Zone (b). See Fig. 4 for the location of the fronts. Note that the mean values of the y-axes differ among a and b, but they have the same scale (maximum value - minimum value = $120 \mu\text{mol kg}^{-1}$). Modified from Appendix C.

5 Outlook and Implications

How the Southern Ocean carbon fluxes and storage will continue into the future remains an open question, due to the Southern Ocean carbon dynamics being sensitive to processes of which we do not know the future evolution. This dissertation presented the large fluctuations in the amount of carbon that is taken up and stored in the Southern Ocean, and one can speculate that this carbon sink will continue to exhibit such fluctuations in the next decades, or even centuries.

New insights on regional and global carbon dynamics can be found by further delving into the two data products that I developed. I have demonstrated with the analysis of these products that a substantial amount of information can be gained from these data, which is worth exploring further. Specifically for the interannual fields, so far I only investigated the interannual variability of the DIC in the Southern Ocean, while the interannual variability in the remaining ocean is yet to be analyzed. Key regions of interest are the tropical Pacific, which experiences large interannual variability as part of the El Niño Southern Oscillation. The North Atlantic is another region of interest, as the Atlantic Deep Water is formed there, taking up large amounts of anthropogenic carbon. Changes in this uptake could affect the global climate and are worth further analysis.

Furthermore, the SOM-FFN approach, that I described in my analysis, can be used to produce time-varying global fields of other carbonate system parameters, such as alkalinity. In combination with temperature and salinity measurements, the remaining carbonate system parameters (pH, pCO_2) can then be computed and further analyzed, for example, to study the changes in ocean acidification or the buffering capacity of the ocean. As new measurements become available, the data products can also be updated to

extend further in time, allowing for continuous monitoring of the carbon uptake and storage, as well as its drivers.

It is worth noting that the potential drivers on the Southern Ocean carbon variability are difficult to disentangle based on observations. As correlation does not imply causation, it is challenging to determine which drivers are necessary and which are sufficient. A necessary cause would be an event, without which the consequence cannot occur, while a sufficient cause would be an event that is always followed by the consequence (Pearl, 2016). Earth System Models are potentially capable tools to disentangle these factors with sensitivity analyses (Pearl, 2016). However, as models currently tend to underestimate the observed variability (Frölicher et al., 2015), first they have to be able to capture this variability before being able to disentangle its drivers.

Another opportunity for further research is the analysis of the statistical drivers of the seasonal cycle of DIC in observations and models. Different CMIP5 models substantially disagree on the phase and amplitude of the seasonal cycle of inorganic carbon in the Southern Ocean (Mongwe et al., 2018). Using the method from Appendix B (Fig. B.7), the seasonal response function from the Neural Network in the Southern Ocean could be derived in models to determine the statistical drivers of DIC in these models. This method could, for example, be applied with different Coupled Model Intercomparison Project (CMIP) models to provide us insights into which models best represent the seasonal cycle of DIC in the Southern Ocean and demonstrate statistically why they do so (e.g., the biology or circulation could be too strong or too weak as a driver). This information could then be used to understand the carbon cycle better and improve climate projections.

Due to the global importance of the Southern Ocean carbon sink (Friedlingstein et al., 2019; Frölicher et al., 2015), the findings from this dissertation are crucial for the sustained monitoring and understanding of not only the Southern Ocean carbon sink, but also of the global carbon cycle, essential for governmental and economic decisions on carbon emission reduction pathways.

Appendices

Appendix A: Keppler, L. and P. Landschützer (2019). "Regional Wind Variability Modulates the Southern Ocean Carbon Sink". In: *Scientific Reports* 9, 7384. DOI: 10.1038/s41598-019-43826-y.

Appendix B: Keppler, L., P. Landschützer, N. Gruber, S.K. Lauvset, I. Stemmler (in review). "Seasonal Carbon Dynamics in the Global Ocean based on a Neural-Network Mapping of Observations". *In review at Global Biogeochemical Cycles*.

Appendix C: Keppler, L. and P. Landschützer (in prep.). "Temporary Reduction in Southern Ocean sub-surface Dissolved Inorganic Carbon". *To be submitted to Geophysical Research Letters*.

A Regional Wind Variability Modulates the Southern Ocean Carbon Sink

Keppler, Lydia^{1,2} & Peter Landschützer¹

¹ Max-Planck-Institute for Meteorology (MPI-M), Hamburg, Germany.

² International Max Planck Research School on Earth System Modelling (IMPRS-ESM), Hamburg, Germany.

Paper status: Published online on 14 May 2019 in Scientific Reports (2019) 9:7384 <https://www.nature.com/articles/s41598-019-43826-y>.

Data availability: The datasets generated during the current study are available from NOAA OCADS ([https://www.nodc.noaa.gov/ocads/oceans/SPC0\\$2\\$1982_present_ETH_SOM_FFN.html](https://www.nodc.noaa.gov/ocads/oceans/SPC0$2$1982_present_ETH_SOM_FFN.html)). All remaining data analysed during this study are included in this published article (and its Supplementary Information files).

Supplementary Information accompanies this paper (see online version).

Contributions: L.K. and P.L. designed the research; L.K. performed the research and analysed the data; P.L. developed the CO₂ data product. L.K. wrote the draft manuscript; P.L. contributed to the discussion of the results and the manuscript at all stages.

Abstract

The Southern Ocean south of 35°S accounts for approximately half of the annual anthropogenic carbon uptake by the ocean, thereby substantially mitigating the effects of anthropogenic carbon dioxide (CO₂) emissions. The intensity of this important carbon sink varies considerably on interannual to decadal timescales. However, the drivers of this variability are still debated, challenging our ability to accurately predict the future role of the Southern Ocean in absorbing atmospheric carbon. Analysing mapped sea-air CO₂ fluxes, estimated from upscaled surface ocean CO₂ measurements, we find that the overall Southern Ocean carbon sink has weakened since ~2011, reversing the trend of the reinvigoration period of the 2000s. Although we find significant regional positive and negative responses of the Southern Ocean carbon uptake to changes in the Southern Annular Mode (SAM) over the past 35 years, the net effect of the SAM on the Southern Ocean carbon sink variability is approximately zero, due to the opposing effects of enhanced outgassing in upwelling regions and enhanced carbon uptake elsewhere. Instead, regional shifts in sea level pressure, linked to zonal wavenumber 3 (ZW3) and related changes in surface winds substantially contribute to the interannual to decadal variability of the Southern Ocean carbon sink.

1 Introduction

The global oceans absorb ~25% of the annually emitted carbon dioxide (CO₂) from human activities (Le Quéré et al., 2018). A disproportionately large part of this uptake is linked to the Southern Ocean south of 35°S, which accounts for ~50% of the annual oceanic CO₂ uptake (Landschützer et al., 2016) and where ~40% of all emitted anthropogenic CO₂ since the beginning of industrialisation is stored (Frölicher et al., 2015; Khatiwala et al., 2009; Sabine et al., 2004). Therefore, the Southern Ocean plays a substantial role in mitigating the effects of human carbon emissions and understanding this carbon sink and its related processes is crucial for future climate projections.

A sobering study by Le Quéré et al. (2007) showed that despite the continued increase in atmospheric CO₂, the Southern Ocean carbon sink saturated in the 1990s, diverging from the expected uptake based on thermodynamic considerations. The authors explained this saturation with a positive trend in the Southern Annular Mode (SAM), i.e., the dominant mode of variability in the Southern Ocean, describing the zonal pressure difference between 40°S and 65°S (Marshall, 2003). This positive trend led to an intensification and poleward shift of the westerly winds, the driving force behind the Southern Ocean upwelling of carbon-rich deep water (Marshall, 2003; Thompson and Solomon, 2002; Thompson et al., 2000). The link between the saturation of the Southern Ocean carbon sink in the 1990s and the positive SAM phase was later confirmed by other model and atmospheric inverse studies (Hauck et al., 2013; Lenton and Matear, 2007;

Lovenduski et al., 2008, 2007; Zickfeld et al., 2007).

Further studies have demonstrated that the response of the mixed-layer depth and temperature to the SAM is not as “annular” (ring-shaped) as previously thought, and is in fact zonally asymmetric, possibly affecting the Southern Ocean carbon uptake (Fogt et al., 2012; Sallée et al., 2010; see also Supplementary Information A_SI.1). Due to the scarcity of observational data, many previous studies focused on zonal averages of the whole Southern Ocean. Although this view has helped to understand the mean dynamics in the last two decades, it is becoming more and more evident that the Southern Ocean is not zonally uniform and that many key processes occur in different regions that are averaged out in zonal averages (Rintoul, 2018; Sallée et al., 2012).

Recent technical advancements and efforts by the scientific community have led to basin-wide observation-based estimates of the sea-air CO₂ flux, sea surface temperature (SST), and sea surface salinity (SSS). To overcome the paucity of CO₂ measurements, novel approaches based on statistical relationships and machine-learning algorithms have advanced our ability to extrapolate and basin-wide map the information collected from single sampling routes (Landschützer et al., 2014).

Using the mapped partial pressure of CO₂ (pCO₂) data until December 2011, a study established that the saturation trend of the 1990s stopped and reversed between the early 2000s and 2011 and that the Southern Ocean had returned to its expected uptake strength (Landschützer et al., 2015). Despite the shipboard-based pCO₂ estimates being heavily extrapolated, longer-term signals, such as the decadal fluctuations that mark the saturation and reinvigoration periods were identified as robust features among different approaches (Ritter et al., 2017; Rödenbeck et al., 2015), and the reinvigoration of the Southern Ocean carbon sink was later confirmed by several other studies (DeVries et al., 2017; Gregor et al., 2018; Ritter et al., 2017).

Despite increasing evidence for the strengthening of the Southern Ocean carbon sink in the 2000s, the processes behind this strengthening are still debated, and the future evolution of this important sink region is highly uncertain. One proposed mechanism is a zonally asymmetric atmospheric circulation, which led to an oceanic dipole of warming and cooling that in turn increased the CO₂ uptake during the Southern Ocean reinvigoration period (2002 through 2011; Landschützer et al., 2015). Another explanation is based on changes in the upper meridional overturning circulation (MOC), which may be linked to trends in the SAM (DeVries et al., 2017). Another study argues that the interannual drivers of the Southern Ocean carbon sink are seasonally decoupled, with wind stress as the main driver in austral winter and biology in austral summer (Gregor et al., 2018).

Here, we build on previous assessments using neural-network derived mapped pCO₂ estimates based on shipboard measurements to demonstrate

the temporal evolution of the Southern Ocean carbon sink and its regional drivers. Finally, we focus on the period after the end of the reinvigoration in 2011 and put our findings from this most recent period in context with previous findings since the 1980s.

2 Results and Discussion

2.1 The Southern Ocean carbon sink variability

Using an updated observation-based mapped estimate of the sea-air CO₂ flux (extended from Landschützer et al. (2016)), we find that the substantial decadal variability of the Southern Ocean carbon sink persists and is present in all three sectors: the reinvigoration period of increased CO₂ uptake lasted until ~2011, and is followed by a reversal of this trend with decreasing carbon uptake until the end of our study period in December 2016 (Fig. A.1b,c), consistent with a previous finding (Gregor et al., 2018).

The integrated CO₂ uptake (Fig. A.1b) does not differ considerably between the three sectors despite the large differences in area (Atlantic sector: $\sim 2.2 \cdot 10^7$ km², Pacific sector: $\sim 3.7 \cdot 10^7$ km², and Indian sector: $\sim 3.0 \cdot 10^7$ km², Fig. A.1a). Specifically, the integrated sea-air CO₂ flux from 2012 through 2016 is approximately equal in each of the three sectors with a mean uptake of 0.3 to 0.4 PgC yr⁻¹ resulting in a total Southern Ocean carbon uptake of $\sim 1.1 \pm 0.2$ PgC yr⁻¹, or approx. 50% of the contemporary annual mean oceanic carbon uptake. The comparable uptake strength between sectors is in agreement with previous results, who found a fairly homogeneous carbon uptake between the three sectors from different model and inversion estimates (Lenton et al., 2013).

Despite the sectoral similarities in the integrated CO₂ uptake, strong sectoral differences exist in the magnitude of the sea-air CO₂ flux per unit area (Fig. A.1c). In particular, the Atlantic sector, i.e., the sector with the smallest spatial extent, reveals the largest variability range from ~ -0.7 mol m⁻² yr⁻¹ in the early 2000s to ~ -1.7 mol m⁻² yr⁻¹ in 2011. Throughout most of the time period, the Atlantic sector is the most intense carbon sink per unit area within the Southern Ocean and from 2012 onward, the CO₂ uptake per unit area in the Atlantic sector (~ 1.4 mol m⁻² yr⁻¹) is nearly twice the amount taken up by the Pacific sector (~ 0.8 mol m⁻² yr⁻¹) and still considerably more than in the Indian sector (~ 1.1 mol m⁻² yr⁻¹). This strong mean uptake has been recently challenged using calculated pCO₂ from biogeochemical Argo floats (Gray et al., 2018; Williams et al., 2017). While the differences are not yet fully resolved, a combination of float and ship data as a next step is required to fully constrain both the seasonal cycle and the mean uptake in the Southern Ocean. We therefore focus on the interannual variability and regional differences rather than the integrated carbon uptake in this study.

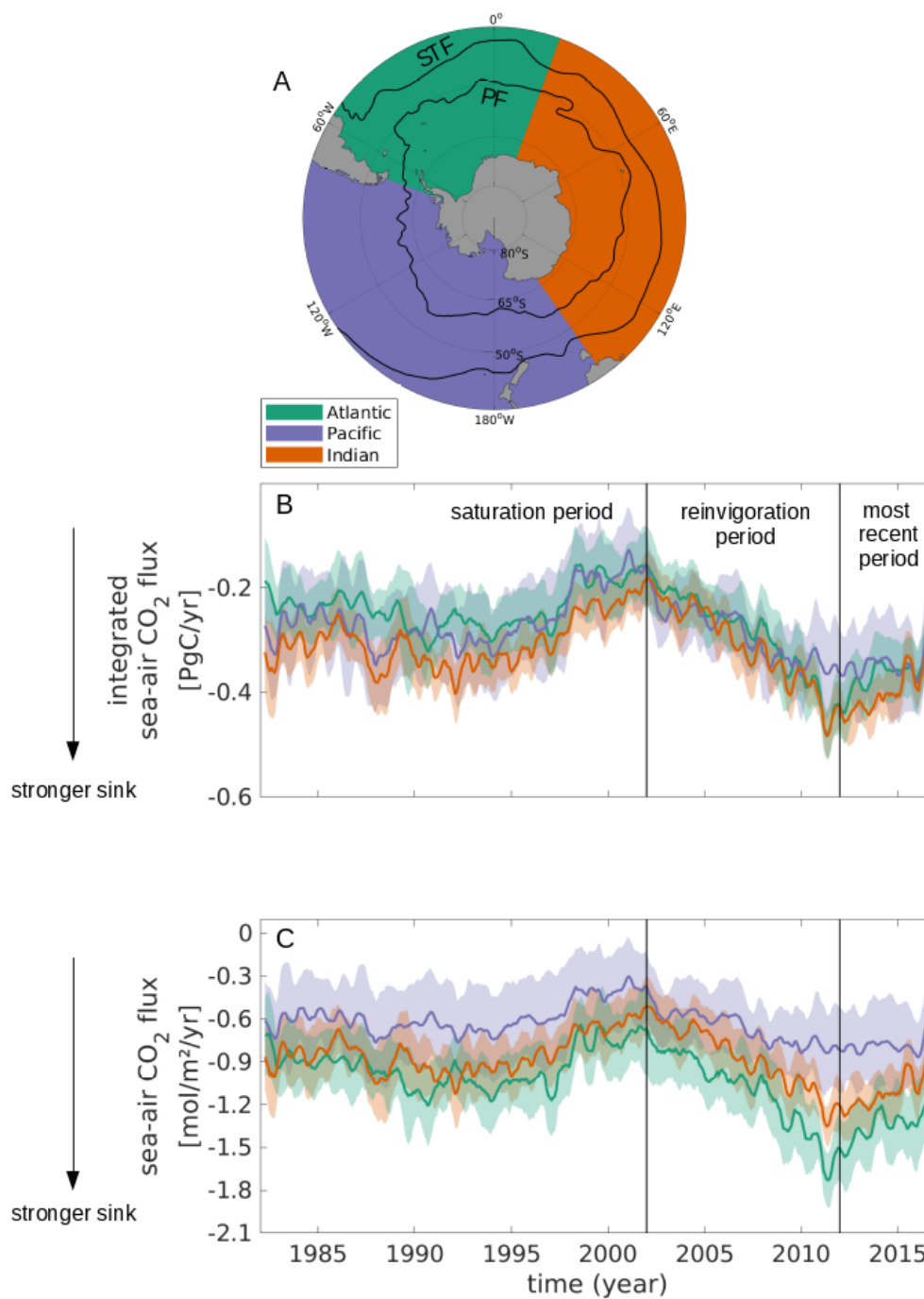


FIGURE A.1: The sectors of the Southern Ocean and the evolution of their carbon sink between 35°S and the Antarctic coast for the Atlantic (green), Pacific (purple), and Indian (orange) sectors from 1982 through 2016. (a) The sectors and fronts in the Southern Ocean, illustrating the Atlantic, Pacific, and Indian sectors in color, and the Subtropical Front (STF) and Polar Front (PF) from Orsi et al. (1995) solid black lines (from north to south). (b) The integrated sea-air CO₂ flux [PgC yr⁻¹]; and (c) the sea-air CO₂ flux per unit area [mol m⁻² yr⁻¹]. (b,c Mean (lines) and one standard deviation around the mean (shading); we removed the mean seasonal cycle from 1982 through 2016, then added the mean of the same time period, and then smoothed with a 3-month running mean; the first and last 3 months are removed during smoothing. The carbon uptake in Fig. A.1c is weighted by the area each grid cells covers. Note that we do not discuss the Southern Ocean carbon flux trends before 2012 extensively in-text, as this has been done in previous studies (Landschützer et al., 2015; Le Quééré et al., 2007).

Another striking observation is that since the late 2000s, stronger differences between the sectors emerge. In the saturation period of the 1990s and the following reinvigoration period in the early 2000s, differences between the sectors stay within one standard deviation around the mean, and they agree on the direction of the trend. However, since approx. 2008, the sink strength in the Pacific sector stalls, whereas the Atlantic and the Indian sectors continue to take up additional carbon until ~ 2011 , followed by a sink reduction thereafter, causing a significant divergence in the uptake intensity between the Atlantic and Pacific sectors.

It is a possibility that the sectoral differences towards the end of the time line are partially due to increased observational data in these years. This is however challenging to test with the available measurements, and model-based observing system simulations might be required to address the effect of data sparsity on the past sea-air CO₂ exchange.

2.2 The SAM's effect on the Southern Ocean carbon sink

The SAM, the dominant climate mode of variability in the Southern Ocean, influences the MOC, and hence the uptake and outgassing of carbon (Hall and Visbeck, 2002; Thompson and Wallace, 2000; Thompson et al., 2000). Specifically, in positive SAM phases, the westerly winds in the Southern Ocean intensify and shift poleward (Hall and Visbeck, 2002). This intensification leads to enhanced Ekman transport, resulting in an increase in both upwelling and subduction, and hence outgassing and uptake, respectively (Downes et al., 2011; Le Quéré et al., 2007; Lovenduski et al., 2007).

A positive trend in the SAM index polarity was suggested as the driver behind the Southern Ocean carbon sink stagnation in the 1990s (Le Quéré et al., 2007). Similarly, a more recent study found that in a region south of Tasmania, there are regions of both increased carbon uptake and outgassing in positive SAM phases in austral summer (Xue et al., 2018). When considering the period from 1982 through 2016, the SAM index illustrates substantial variations in time; however, it further shows a continuous positive long-term trend (Fig. A.2a). Therefore, we first investigate if the SAM affects the Southern Ocean carbon sink as a whole when considering the entire 35-year period (1982 through 2016). A 2D correlation and regression analysis confirms the link between the SAM and the carbon uptake but highlights the contrasting regional differences within the Southern Ocean (Fig. A.2). The resulting pattern closely reflects the results of a model-based study (Lovenduski et al., 2007).

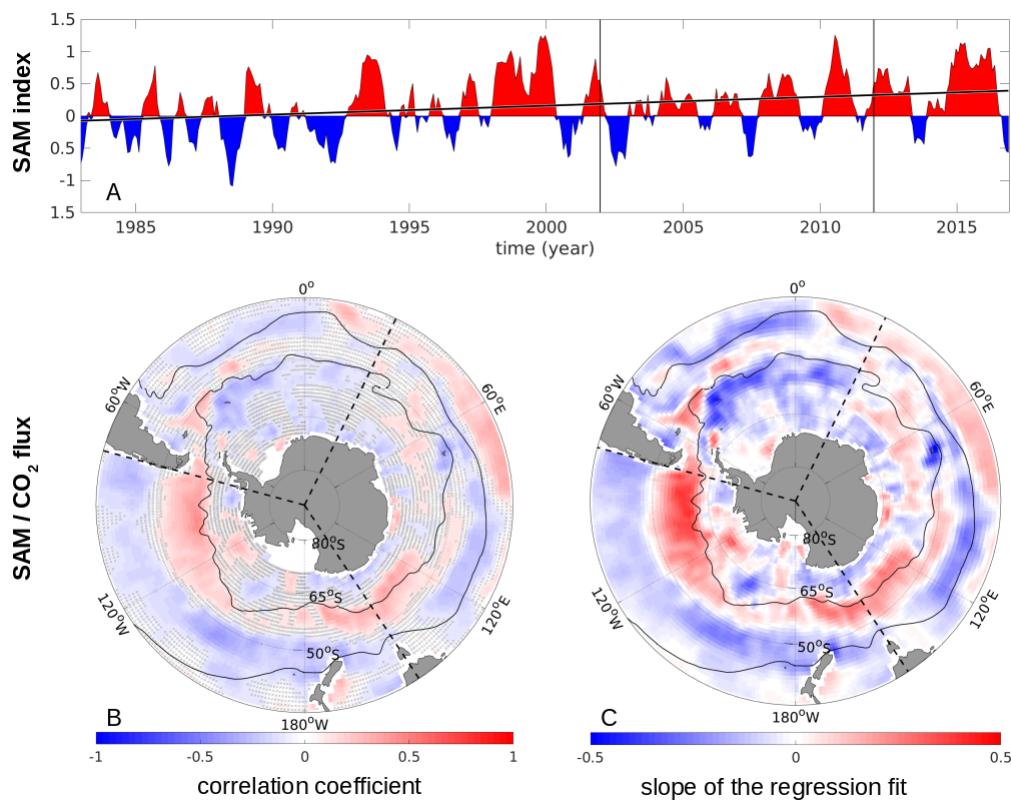


FIGURE A.2: The relationship between the SAM index and the CO₂ flux anomaly from January 1982 through 2016. (a) Standardized SAM index, smoothed with a 3-month running mean, and the trend line in black. Positive SAM indices are illustrated in red, negative ones in blue. The start of the reinvigoration (Jan 2002) and the most recent period (Jan 2012) are marked with thin vertical black lines. (b) The correlation coefficients between the sea-air CO₂ flux anomaly [$\text{mol m}^{-2} \text{yr}^{-1}$] and the smoothed, standardized SAM index. Coefficients with significance $< 95\%$ are hatched. (c) The slope of the regression fit between the sea-air CO₂ flux anomalies [$\text{mol m}^{-2} \text{yr}^{-1}$] and the standardized SAM index. As the SAM index is standardized to have a mean of 0 and a standard deviation of 1, (c) illustrates the change in the CO₂ flux [$\text{mol m}^{-2} \text{yr}^{-1}$] per standard deviation of the SAM. (b-c) The mean positions of the PF and the STF are illustrated as thin black lines, the three Southern Ocean sectors are delimited by dashed black lines, and coastal areas are masked white.

In agreement with that study (Lovenduski et al., 2007), positive SAM phases correlate with anomalous outgassing in the region between $\sim 50^\circ\text{S}$ and $\sim 65^\circ\text{S}$, with the exception of the Atlantic sector (Fig. A.2b), potentially illustrating the recently suggested zonal SAM asymmetry (Fogt et al., 2012; Sallée et al., 2010). However, we find that for most of the remaining Southern Ocean, the CO₂ flux correlates negatively with the SAM index; here, positive SAM phases are linked to increased uptake. The general picture is comprised of alternating zonal bands with positive and negative correlations. However, the pattern in the Atlantic sector is approximately opposite to the Pacific sector south of $\sim 45^\circ\text{S}$.

Regionally, the link between the SAM and the air-sea exchange of CO₂ derived from mapped shipboard observations is evident. Just north of the PF in the Pacific sector, anomalous outgassing of approx. $0.5 \text{ mol m}^{-2} \text{yr}^{-1}$ occurs per standard deviation of the SAM (Fig. A.2c). Conversely, south of the PF in the Atlantic sector, anomalous carbon uptake of $\sim 0.4 \text{ mol m}^{-2}$

yr^{-1} occurs per standard deviation of the SAM.

However, when integrating the total effect of the SAM on the Southern Ocean carbon uptake south of 35°S , we find that the regionally opposing effects cancel each other out: the net effect is 0.0 PgC yr^{-1} per standard deviation of the SAM, for the whole Southern Ocean, and the net effect in each of the three sectors is also 0.0 PgC yr^{-1} . Inversion and model-based studies have also found a compensation of positive and negative correlations between the sea-air CO_2 flux and the SAM throughout the Southern Ocean (Hauck et al., 2013; Lenton and Matear, 2007; Lovenduski et al., 2007). These studies found a slightly positive net integrated uptake of $\sim 0.1 \text{ PgC yr}^{-1}$ per standard deviation of the SAM in their study periods. However, our findings based on upscaled observations suggest that the positive trend in the SAM does not considerably alter the basin-wide net Southern Ocean CO_2 uptake over the past 35 years.

2.3 Physical sea surface properties and the carbon flux from 2012 through 2016

Despite its regional correspondence and its link to the saturation of the Southern Ocean carbon sink in the 1990s (Le Quéré et al., 2007), the SAM index polarity does not fully explain the overall Southern Ocean carbon sink variability over the 35-year period. We therefore continue to investigate other potential drivers.

As CO_2 is more soluble in colder water, one would expect positive correlations between SST and sea-air CO_2 flux anomalies in regions where the solubility of CO_2 is the dominant driver (negative SST anomalies negative corresponding to negative sea-air CO_2 flux anomalies). Instead, the general picture during this period are alternating zonal bands of positive and negative correlations. Specifically, warmer SST correspond to less uptake in the northern region of subduction, to less outgassing in the upwelling band, i.e., where circulation and/or biology dominate the CO_2 flux variability (Landschützer et al., 2014; Takahashi et al., 2002), and patches of less uptake in the southern regions of deep water formation (Fig. A.3a, see also Supplementary Information A_SI.4-A_SI.6).

Hence, in the northern zonal band (north of $\sim 40^{\circ}\text{S}$) solubility drives the CO_2 flux variability. In contrast, south of 40°S the band of negative correlations suggests other processes to be dominant, such as variations in dissolved inorganic carbon (DIC) and alkalinity (Takahashi et al., 2009). This zonal symmetry suggests different drivers than explored in the reinvigoration period, where the authors found that in the Pacific Sector of the Southern Ocean changes in the thermal component dominated over the non-thermal counterpart (Landschützer et al., 2015).

In contrast, the correlation between SSS and CO₂ flux anomalies reveals only some significant patches at the 95% confidence level (Fig. A.3b).

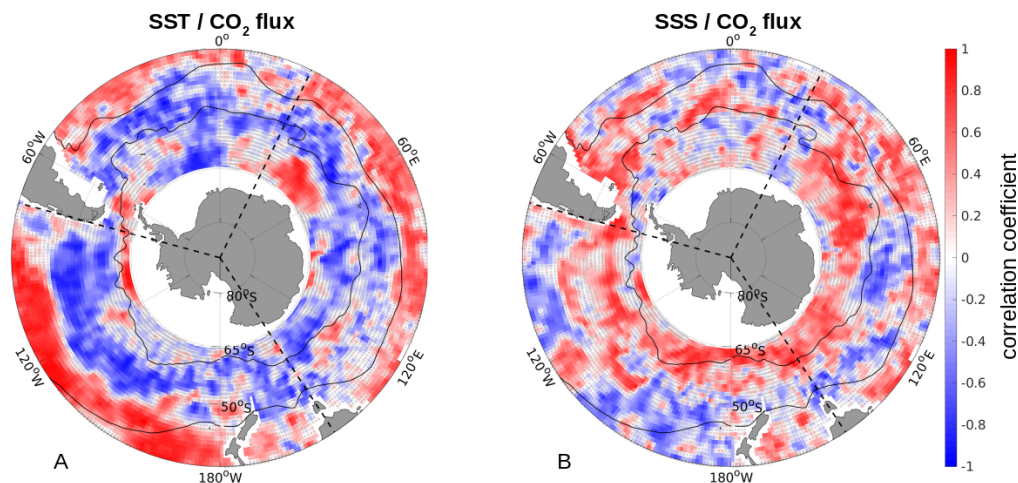


FIGURE A.3: The correlation coefficients between the sea-air CO₂ flux anomaly (negative is into the ocean) and SST (a) and SSS (b) anomalies from 2012 through 2016. The trend and seasonal cycle was removed from all three variables, and then smoothed with a 3-month running average. The mean positions of the PF and the STF are illustrated as thin black lines, the three Southern Ocean sectors are delimited by dashed black lines, and coastal areas are masked white. Coefficients with significance < 95% are hatched.

2.4 Regional shifts in sea level pressure (SLP) and surface winds as CO₂ flux drivers

As we have demonstrated in the previous section, changes in the non-thermal drivers (i.e. DIC, alkalinity or biology), and not solubility, are the dominant processes behind the recent Southern Ocean carbon sink. Although the atmospheric forcing on the ocean dynamics is generally non-linear (O’Kane et al., 2013), the relationship between atmospheric forcing and ocean dynamics has been suggested in the past to influence the Southern Ocean carbon uptake (DeVries et al., 2017; Le Quéré et al., 2007). Here, we demonstrate that regional shifts in SLP and the related winds affect the MOC, modulating the Southern Ocean carbon sink.

The southern extra-tropical atmospheric circulation is overall zonally symmetric, but significant asymmetries, such as zonal wavenumbers 1 and 3 (ZW1 and ZW3, respectively) are present within this zonal flow (Hobbs and Raphael, 2010; Raphael, 2004). ZW1 and ZW3 are quasi-stationary, where ZW1 is a zonal wave with one ridge in the Pacific sector and one trough in the Atlantic sector, while ZW3 has ridges south of each of the three continents and three troughs in between (Hobbs and Raphael, 2010; Loon and Jenne, 1972). The observed picture is generally a combination of both ZW1 and ZW3, while ZW1 tends to be considerably more dominant (Hobbs and Raphael, 2010; Quintanar and Mechoso, 1995).

From 2002 through 2011, a more zonally asymmetric atmospheric circulation was suggested to lead to an oceanic dipole of warming and cooling, which was identified to drive the reinvigoration of the Southern Ocean carbon sink (Landschützer et al., 2015, see also Supplementary Information A_SI.7). Due to geostrophic balance, the winds follow this pattern, resulting in stronger zonal winds in the Pacific sector, and weaker zonal winds in the Atlantic and Indian sectors. In turn, anomalous northward advection in the Pacific sector led to enhanced upwelling of cold water, enabling enhanced carbon uptake due to the solubility of CO₂. Concurrently, anomalous southward advection in the Atlantic sector led to enhanced downwelling and carbon uptake in that area (Gruber et al., 2019b; Landschützer et al., 2015). The SLP in this time period resembles the inverse structure of the typical ZW1 pattern (Landschützer et al., 2015, see also Supplementary Information A_SI.7) with an additional imprint of the ZW3 pattern (Gruber et al., 2019b).

Based on this finding, it appears plausible that a dominance shift of ZW1 or ZW3 might drive the most recent Southern Ocean carbon sink stagnation. Indeed, from 2012 through 2016, the trends in SLP and resulting surface wind velocity have shifted substantially again compared to both the saturation and reinvigoration periods (Fig. A.4a; see also Supplementary Information A_SI.7). In this period, we find a strong asymmetry in the local pressure system with a positive SLP trend over the Drake Passage (~30°W), south of Africa (~20°E), and west of Australia (~100°E), and negative SLP trends in between (Fig. A.4a). This pattern strongly resembles the positive ZW3 pattern (Hobbs and Raphael, 2010), with the exception that typical ZW3 patterns are more symmetric, with the third ridge being further east, just south of Australia (Hobbs and Raphael, 2010; Loon and Jenne, 1972). This is in line with a recent study by Schlosser et al. (2018), who found that 2016 has a strong positive phase in the ZW3, causing significant decay of Antarctic sea ice. Due to geostrophic balance, winds tend to follow the SLP, as seen in Fig. A.4a. We find that south of the PF in the Atlantic and Indian sectors, the local trends enhance the westerly wind circulation, while at the same latitudes in the eastern Pacific the local trends counteract the westerly circulation.

Previous studies have shown that enhanced westerlies enhance the MOC, while decreased westerlies decrease the MOC (DeVries et al., 2017; Le Quéré et al., 2007). To investigate the effects of the changes in the MOC, we consider the changes in pCO₂. The ΔpCO₂ (oceanic pCO₂ – atmospheric pCO₂) trends from 2012 through 2016 are predominantly positive south of the PF (Fig. A.4b), indicating reduced uptake close to the seasonally ice-covered regions. In addition, the total ΔpCO₂ has mainly a negative trend north of the STF in all three sectors, while between the PF and the STF, the trends are mainly positive (i.e., reduced uptake/increased outgassing), with the most dominant exception being the eastern Pacific sector around 50°S. The recent decrease in the carbon uptake per unit area in the Atlantic and Indian sectors shown in Fig. A.1c is hence mainly due to a decrease in carbon uptake in the higher latitudes, which is slightly offset by the

increased uptake north of the STF. Similarly, the recent stagnation in the carbon uptake per unit area in the Pacific sector is largely due to increased uptake towards the north-eastern Pacific sector being offset by decreased uptake towards the south-western Pacific sector.

To determine the processes behind the trends in the total $\Delta p\text{CO}_2$, we further separate the observed trends in the surface ocean $p\text{CO}_2$, using the CO_2 sensitivity of seawater to thermal changes of $4.23\%/^\circ\text{C}$ (Landschützer et al., 2015; Takahashi et al., 2002). As CO_2 dissolves faster in colder water, areas with negative trends in the thermal component of $p\text{CO}_2$ are regions that enhance the carbon uptake (Takahashi et al., 1993). The trend in the thermal component (Fig. A.4c) is mainly negative, i.e., surface waters cooled over the past few years, with a few exceptions, most notably in the eastern Pacific sector north of the PF, thereby enhancing the solubility of seawater.

The non-thermal component is comprised of the sum of circulation and biological effects. Regions of upwelling are usually associated with outgassing, while subduction areas tend to be regions of carbon uptake. Moreover, regions of high biological productivity tend to be regions of carbon sequestration. The pattern of the trend of the non-thermal component of the $\Delta p\text{CO}_2$ (Fig. A.4d) closely resembles the pattern of the trend of the total $\Delta p\text{CO}_2$ (Fig. A.4b), with the thermal component offsetting the non-thermal component.

Combining the findings from Fig. A.4, we find that in the Atlantic and Indian sectors, south of the STF, increased winds enhance the westerly circulation (Fig. A.4a), likely resulting in an increase in Ekman-induced upwelling of carbon-rich waters from deeper layers, which explain the observed anomalous outgassing and northward transport of cold and carbon-rich waters in these two sectors south of the STF (see Fig. A.4b and d). In contrast, at the same latitudes in the Pacific sector, decreased winds as a result of the high-pressure area at Drake Passage explain the observed decreased carbon uptake and decreased outgassing here, likely imposed by reduced upwelling and subduction. In contrast, the inflow of warmer surface waters from the north, induced by enhanced westerlies, only in part counteracts the non-thermal signature. Concurrently, Fig. A.4a reveals enhanced winds in the west of the Pacific sector leading to enhanced upwelling and subduction, and hence both increased carbon uptake and increased outgassing. These opposing effects lead to the overall CO_2 flux stagnation of the Pacific sector in this period.

Our finding that the carbon uptake in the Pacific sector is mainly driven by the non-thermal component, is somewhat contrary to previous findings that trends in this region are solubility driven (Landschützer et al., 2015), but might also indicate that the relative dominance between thermal and non-thermal drivers is shifting in time, highlighting the complexity of the Southern Ocean carbon sink.

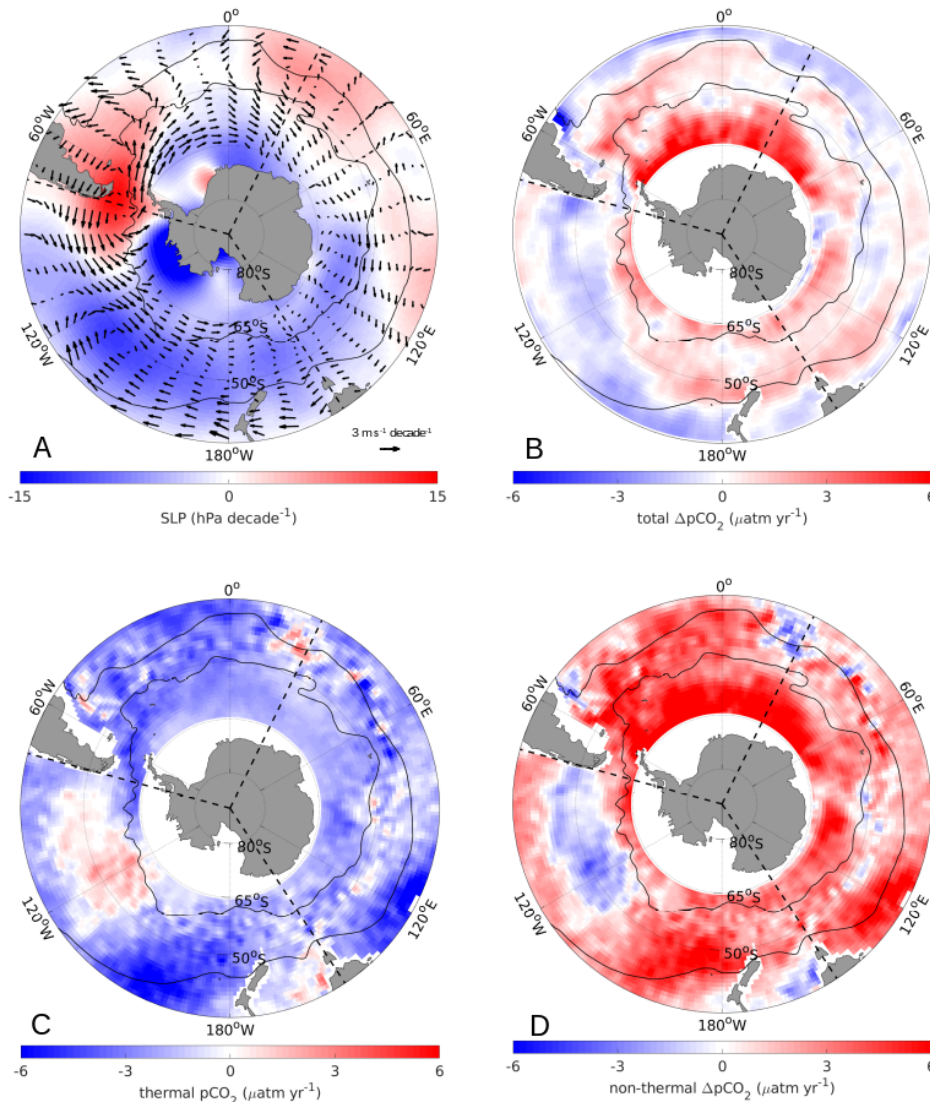


FIGURE A.4: Trends of SLP and 10 m wind velocity and the trends of the $\Delta p\text{CO}_2$, (oceanic $p\text{CO}_2$ - atmospheric $p\text{CO}_2$) its components during the most recent period (2012 through 2016). (a) Trend of the SLP (hPa decade^{-1}) (color) and trend of the 10 m wind velocity [$\text{m s}^{-1} \text{decade}^{-1}$] (vectors). (b) Trend of the $\Delta p\text{CO}_2$ ($\mu\text{atm yr}^{-1}$); (c) trend of the thermal component of the $p\text{CO}_2$ ($\mu\text{atm yr}^{-1}$); (d) trend of the non-thermal component of the $\Delta p\text{CO}_2$ ($\mu\text{atm yr}^{-1}$). The mean positions of the PF ($\sim 55^\circ\text{S}$) and the STF ($\sim 40^\circ\text{S}$) are illustrated as thin black lines, the three Southern Ocean sectors are delimited by dashed black lines. See S7 for the analogous figure for the reinvigoration period (2002 through 2011).

3 Summary and Conclusions

In summary, our study demonstrates that regionally, the Southern Ocean carbon uptake shows a significant regional correspondence to the SAM index polarity, although when considering the entire 35-year period, the SAM does not have a considerable effect on the overall Southern Ocean carbon uptake. Instead, regional shifts in SLP closely tied to the ZW3 pattern in the Southern Ocean and related surface wind velocity substantially affect the most recent evolution of the Southern Ocean carbon

sink. In the Atlantic and Indian sectors, enhanced outgassing in upwelling regions and decreased uptake in subduction regions dominate after 2011, causing the carbon sink in these sectors to weaken. In the Pacific sector, however, regionally opposing trends to the east and the west linked to the ZW3 pressure asymmetry cause the net carbon sink of this sector to stall. In particular, towards the eastern Pacific sector, local wind patterns counteracting the mean westerly flow lead to decreased upwelling of carbon from deeper ocean layers, while towards the west, local winds enhancing the westerly flow lead to enhanced stirring and outgassing of carbon. Our results also reveal a rather complex picture of the Southern Ocean carbon sink. While from 2002 through 2011 it was suggested that the increase in solubility led to more carbon uptake in the Pacific sector (Landschützer et al., 2015), in the subsequent years the wind-driven upward stirring caused a slow-down of the uptake in the eastern part of this basin. Our findings therefore suggest that the evolution of the Southern Ocean carbon sink is not only determined by local weather patterns but further determined by the relative dominance of thermal and non-thermal drivers that appear to locally interchange dominance in time.

Our study implies that adequate observations of SLP and winds in the Southern Ocean are key to better understand the regional processes in this dynamic region on interannual to decadal timescales. Similarly, future studies including better representation of regional weather patterns in earth system models may lead to a better modelled representation of the Southern Ocean carbon cycle and close the present discrepancies between model-based and observation-based sea-air fluxes.

It is an open question of how the Southern Ocean carbon sink will continue to evolve. However, we demonstrate that understanding the evolution of regional weather patterns is key in monitoring the Southern Ocean sink strength on interannual to decadal timescales.

4 Data and Methods

We combine data from different platforms in the Southern Ocean south of 35°S, which we introduce below.

4.1 Ship-based sea-air CO₂-flux estimate

We use a neural-network derived mapped estimate of the sea-air CO₂ flux, which is based on data from the Surface Ocean CO₂ Atlas database SOCATv5 (Bakker et al., 2016). To overcome the paucity of shipboard pCO₂ observations, this product applies a 2-step neural-network mapping approach, using a suite of independent predictors as proxy data to infer the final pCO₂ fields. In the first step of this SOM-FFN method, self-organizing maps (SOM) cluster the global ocean into biogeochemical provinces. In the second step, a feed-forward network (FFN) is applied to determine the

statistical relationships between the SOCATv5 data (Bakker et al., 2016) and proxy parameters within the provinces to then estimate the $p\text{CO}_2$. Lastly, the sea-air CO_2 flux is computed using a bulk flux formulation, where positive values indicate outgassing, and negative values indicate oceanic uptake of CO_2 . The gas transfer is computed using a quadratic wind dependence (Wanninkhof, 1992) based on ERA-interim wind speeds (Dee et al., 2011). The gas transfer coefficient is then scaled so that the mean transfer velocity of 16 cm hr^{-1} matches a recent estimate by Wanninkhof et al. (2013). For more information on this method see Landschützer et al. (2013) and for a discussion on the robustness of this data estimate, see S2. This mapped estimate is on a $1^\circ \times 1^\circ$ monthly grid, originally created from 1982 through 2011 (Landschützer et al., 2014; Landschützer et al., 2016). We extend it by five additional years until December 2016. We compute the CO_2 flux anomalies by removing the climatological seasonal cycle and smooth the remaining high-frequency variability using a 3-month running mean.

4.2 The SAM index

We use the SAM index by Marshall (2003), which is based on the observed pressure difference between six stations at 40°S and 65°S . We standardise the index by subtracting the mean and dividing it by the standard deviation over the time period (1958 to 2017), following Lovenduski et al. (2007). We then smooth the standardised index with a 3-month running mean in order to be able to analyse the interannual signal of the SAM, following Lenton and Matear (2007). Although some studies do not smooth the SAM index at all, others smooth with a running mean of 8 or 12 months (Hauck et al., 2013; Lenton and Matear, 2007; Lovenduski et al., 2007). We tested different high-pass and low-pass filters and found that the 3-month running mean can represent the interannual variability of the SAM index without removing too much of the signal.

4.3 Argo float-based SST and SSS

Argo floats are autonomous profiling floats that measure seawater properties in the water column (<http://www.argo.ucsd.edu/>). As such, they fill large observational gaps in the ocean, especially in historically under-sampled regions, such as the Southern Ocean. The Roemmich and Gilson (2009) Argo-based product provides optimally interpolated data of temperature and salinity of the top 2000 m on a monthly $1^\circ \times 1^\circ$ grid. Due to the relatively high spatiotemporal density of floats compared to ship data, this data set is of high confidence and provides reliable in-situ data. We use the shallowest value at 2.5 m of the temperature and salinity for the SST and SSS respectively from January 2004 until December 2016 (i.e., 13 years of data). Based on the data availability of this product, the analysis of the sea surface properties only extends until 65°S . It would be interesting to analyse the region south of 65°S as well, as this is a region of deep water formation and hence subduction. However, as this region is partially ice-covered, there are few Argo profiles with good quality control flags, which results in data

with lower confidence than the gridded Argo-based data we use in this study. It has to be left for future analyses to investigate the relationship between the physical sea surface properties and the carbon sink in this region. As for the sea-air CO₂ flux, we compute anomalies by removing the climatological seasonal cycle and we smooth remaining high-frequency variability using a 3-month running mean.

4.4 SLP and surface wind velocity

To analyse how the SLP and related wind velocity affects the Southern Ocean carbon uptake, we use reanalysis data between January 2004 and December 2016. For the SLP, we used the NCEP/NCAR Reanalysis monthly mean data (www.esrl.noaa.gov/psd/data/gridded/data.ncep.reanalysis.surface.html), and for the wind velocity, we use the monthly mean zonal and meridional 10 m wind velocity components from Era Interim (<http://apps.ecmwf.int/datasets/data/interim-full-daily/levtype=sfc/>).

4.5 Separation into thermal and non-thermal components and $\Delta p\text{CO}_2$

Following Takahashi et al. (2002), we separate the thermal and non-thermal components of the pCO₂ at each grid point using Eq. A.1 and A.2:

$$\text{non-thermal} = p\text{CO}_2 \cdot \text{EXP}(0.0423 \cdot (sst_{mean} - sst)) \quad (\text{A.1})$$

$$\text{thermal} = p\text{CO}_{2mean} \cdot \text{EXP}(0.0423 \cdot (sst - sst_{mean})) \quad (\text{A.2})$$

where at each grid point, pCO₂ is the oceanic pCO₂ at a given point in time, pCO_{2mean} is the mean pCO₂ over the whole time period, sst is the SST at the given point in time, and sst_{mean} is the mean SST of the whole time period. Following Landschützer et al. (2015), we compute $\Delta p\text{CO}_2$ by subtracting the atmospheric pCO₂ at each grid point from the oceanic pCO₂ at the same grid point. We obtain atmospheric xCO₂ from the NOAA marine boundary layer reference product (<https://www.esrl.noaa.gov/gmd/ccgg/mb1/>). From this, we calculate atmospheric pCO₂ as outlined in Landschützer et al. (2013) using the NCEP sea level pressure (Kalnay et al., 1996) and the water vapour correction by Dickson et al. (2007).

4.6 Ocean sectors and position of fronts

To analyse sectoral differences within the Southern Ocean, we define the Atlantic sector from 70°W to 20°E, the Indian sector from 20°E to 145°E, and the Pacific sector from 145°E to 70°W (see Fig. A.1a). We chose to divide the Southern Ocean into these sectors and not, e.g., into water masses, because the sectors are separated by fixed lines, while other ways of dividing the ocean are dynamic and not straight-forward. In addition, similar processes are at play within each of the sectors. Furthermore, several fronts separate the Southern Ocean and divide it into inter-frontal zones with unique biogeochemical and physical properties (e.g., Roemmich and Gilson (2009)). For our analysis and discussion, we use the Subtropical Front (STF) at

$\sim 40^{\circ}\text{S}$ and the Polar Front (PF) at $\sim 55^{\circ}\text{S}$ as defined by Orsi et al., 1995 (see Fig. A.1a). Although we use the mean position of the fronts, the positions of the fronts are not static as they change their position on time scales from intra- to interannual (Trull et al., 2001).

B Seasonal Carbon Dynamics in the Global Ocean based on a Neural-Network Mapping of Observations

Keppler, Lydia^{1,2}, Peter Landschützer¹, Nicolas Gruber³, Siv Kari Lauvset⁴, Irene Stemmler¹

¹ Max-Planck-Institute for Meteorology (MPI-M), Hamburg, Germany.

² International Max Planck Research School on Earth System Modelling (IMPRS-ESM), Hamburg, Germany.

³ Environmental Physics, Institute of Biogeochemistry and Pollutant Dynamics, ETH Zurich, Switzerland

⁴ NORCE Norwegian Research Centre, Bjerknes Centre for Climate Research, Bergen, Norway

Paper status at the time of the submission of this thesis:
In Review at the Journal of Global Biogeochemical Cycles

Data availability:

The data product created during this study is freely available to the public (will be submitted to NCEI OCADS after publication of this paper).

Supplementary Information accompanies this paper at the end of this Appendix.

Contributions: L.K. and P.L. designed the research; L.K. performed the research; L.K. wrote the draft manuscript; all authors contributed to the discussion of the results and the manuscript at all stages.

Abstract

The seasonal cycle represents one of the largest perturbations of the natural carbon cycle in the ocean, yet the global seasonal pattern of dissolved inorganic carbon (DIC) is not well established. Here, we present the first global monthly climatology of oceanic DIC extending from the surface to 2000 m, obtained by a 2-step neural network method and DIC measurements from the GLODAPv2.2019 data product. Tests with synthetic data from an ocean biogeochemistry model and with independent observations demonstrate that the method successfully captures the spatio-temporal variability of DIC with an average root mean squared error of $\sim 20 \mu\text{mol kg}^{-1}$. We find the largest amplitudes of the seasonal cycle of surface DIC in the northern high latitude Pacific (~ 30 to $>50 \mu\text{mol kg}^{-1}$). Surface maxima tend to occur in hemispheric spring and minima in late summer, driven by the input of DIC into the upper ocean by mixing during winter/early spring, and the subsequent biological draw-down of DIC in summer. This seasonal pattern extends to a nodal depth of <50 m in the tropics and several hundred meters in the subtropics, below which the seasonal cycle has the opposite phase, although with a smaller amplitude. From the carbon draw-down, we estimate the hemispheric summer net community production (NCP) from the surface to the base of the euphotic zone at global scale. We find a global mean summer NCP of $\sim 1.4 \pm 0.2 \text{ mol C m}^{-2}$ ($\sim 6.1 \pm 0.9 \text{ PgC}$) with the highest production rates in the North Atlantic (up to $\sim 5 \text{ mol C m}^{-2}$).

1 Introduction

The vast majority of the dissolved inorganic carbon (DIC) that exists in the ocean is part of the natural carbon cycle. This pool of roughly 36,000 PgC (1 PgC = 10^{15} g carbon) contains about 90% of the total amount of carbon in the ocean, atmosphere, and land biosphere system combined (Ciais et al., 2014). Since the beginning of the industrial revolution, human activities, mostly through the release of anthropogenic carbon dioxide (CO_2) from the burning of fossil fuels and land-use change, have perturbed these pools substantially. By the year 2007, the ocean DIC pool had grown by 152 ± 20 PgC relative to the year 1800 through the uptake of this anthropogenic CO_2 from the atmosphere (Gruber et al., 2019b). The current oceanic net uptake rate of $2.5 \pm 0.6 \text{ PgC yr}^{-1}$ constitutes approximately 23% of the anthropogenic CO_2 emissions on an annual basis, thereby highlighting the crucial role of the ocean in ameliorating one of the key drivers of climate change (Friedlingstein et al., 2019; Le Quéré et al., 2018). Thus, it is not surprising that nearly all studies in the last four decades investigating changes in the interior distribution of DIC have focused on this long-term anthropogenic perturbation of oceanic DIC (Brewer, 1978; Chen and Millero, 1979; Gruber et al., 1996; Sabine and Tanhua, 2010).

In contrast, changes in the natural carbon cycle, and especially those changes in oceanic DIC occurring on seasonal timescales have received

considerably less attention. This is a remarkable shortcoming, as the seasonal cycle represents one of the strongest perturbations of the natural carbon cycle in the ocean, creating seasonal variations that in most places far exceed those occurring on inter-annual to decadal timescales (Bates et al., 2014; Brix et al., 2004; Gruber et al., 2002). The seasonal cycle of DIC is driven by the interaction of ocean circulation, vertical mixing, air-sea gas exchange, and net community production (NCP), i.e., the net exchange of carbon between the inorganic and organic forms driven by the balance between photosynthesis and respiration/remineralization (Sarmiento and Gruber, 2006). Thus, provided that the contribution of the physical mechanisms can be estimated, the seasonal cycle of DIC can serve as an important quantitative constraint for biological productivity (Emerson et al., 2008; Gruber et al., 1996; Keeling et al., 2004; Ostle et al., 2015) and ultimately its response to a changing climate. These estimates of NCP, although originally primarily using oxygen (Jenkins and Goldman, 1985; Riser and Johnson, 2008) and later also isotopes of carbon and oxygen (Juranek et al., 2012; Quay and Stutsman, 2003) and nutrients (Emerson et al., 2008; Plant et al., 2016), have revealed a remarkably uniform oceanic distribution of NCP, which over the annual timescale is very roughly equal to export production (Emerson and Bushinsky, 2014). So far, the only attempt to extend such an effort on a global scale was made by Lee, 2001, who only used data from the sea-surface, using a climatology of surface $p\text{CO}_2$ and alkalinity, to derive the seasonal cycle of DIC. That analysis revealed a global NCP of 9.1 ± 2.7 or 10.8 ± 2.7 PgC yr^{-1} , depending on the method used. However, these estimates have a large uncertainty as they were limited to surface data. Using seasonal oxygen data extending throughout the upper ocean, Najjar and Keeling, 1997 demonstrated that the seasonal cycle can imprint deep into the upper ocean, with many places having a nodal depth at which the phase of the seasonal cycle shifts by $\sim 180^\circ$, owing to the shifting balance between production and respiration/remineralization.

Furthermore, changes in the seasonal cycle of DIC and other tightly linked carbonate system parameters such as the surface ocean partial pressure of CO_2 ($p\text{CO}_2$) or oceanic pH are predicted to occur in response to the oceanic uptake of anthropogenic CO_2 from the atmosphere (Hauck and Voelker, 2015; Kwiatkowski et al., 2018; Rodgers et al., 2008). These changes in the seasonal cycle can be crucial for the onset of critical effects of ocean acidification on marine organisms (McNeil and Sasse, 2016). While changes in the seasonal cycle of $p\text{CO}_2$ have already been detected (Landschützer et al., 2018), no such studies of DIC exist.

A further reason to focus on the seasonal cycle of DIC is that this cycle represents the largest natural perturbation of the natural carbon cycle, providing perhaps also insights into the sensitivity of this cycle to other perturbations, especially those associated with climate change. In this respect, it is a concern that the seasonal cycle of DIC and oceanic $p\text{CO}_2$ are not well captured in the current generation of Earth System Models used to make projections for the future behavior of the coupled carbon cycle climate

system. For example, Mongwe et al. (2018) compared the CO₂ uptake in 10 Earth System Models from the Coupled Model Intercomparison Project version 5 (CMIP5) in different sub-regions of the Southern Ocean. In these sub-regions, the models disagree on both the amplitude and the phase of the seasonal cycle, and they disagree on the relative importance of DIC and temperature in regulating the seasonal air-sea CO₂ exchange. Additionally, an Earth System Model's representation of the present-day seasonal cycle of DIC has been demonstrated to considerably affect the model's projected carbon uptake in the future (Nevison et al., 2016).

Taken together, this illustrates the need to better constrain the seasonal cycle of DIC from observations and to better understand its drivers, in particular, the role of biological productivity. This will not only provide a necessary step towards improving near-term predictions and longer-term projections of Earth System Models, but also improve our quantitative understanding of the ocean's biological productivity at a global scale.

No such global-scale analysis of the observation-based seasonal cycle of DIC exists, and this is largely due to data sparsity (Fig. B.1). Direct measurements largely collected during repeat hydrography expeditions provide a highly accurate basis to track the global-scale and long-term evolution of the oceanic carbon sink, yet they are sparse in space and time (Olsen et al., 2019; Talley et al., 2016). An important exception are the DIC measurements from various time-series sites around the world, which demonstrate the importance of the seasonal cycle (Bates et al., 1996; Dore et al., 2003; Gruber et al., 2002; Keeling, 1993; Michaels et al., 1994). However, there are only seven stations with sufficient coverage to establish the climatological seasonal cycle without any form of statistical modeling (Bates et al., 2014). These data also demonstrate that the phase and amplitude of the seasonal cycle of DIC vary considerably by location, but for the remainder of the ocean, the seasonal cycle of DIC remains very weakly constrained.

In recent years, Argo floats equipped with biogeochemical (BGC) sensors have complemented shipboard observations by measuring pH. These pH measurements can be used to calculate the DIC when combined with high-quality hydrography data and empirical algorithms (Bittig et al., 2018; Carter et al., 2018; Williams et al., 2017). Data assimilation efforts such as the BGC Southern Ocean State Estimate have begun to use these data to create a novel state estimate (Verdy and Mazloff, 2017); however, they are currently limited to the Southern Ocean.

An alternative means to establish the seasonal cycle of DIC is to use a mapping method based on the available observations. This is the approach taken by Sasse et al. (2013) who used a single-step neural network method to produce the first global surface map of DIC at seasonal resolution. These artificial neural networks can map time-varying data based on complex, non-linear relationships between the input and output data to overcome the existing challenges due to data sparsity (Dibike and Coulibaly, 2006; Hornik

et al., 1989). While representing a major step forward, the DIC climatology by Sasse et al. (2013) was limited to the surface. In contrast, Lauvset et al. (2016) provide a measurement-based mapped DIC product extending over the entire upper ocean. However, their climatology is limited to the annual mean for a single reference year and is likely seasonally biased owing to the summer bias of the underlying DIC measurements.

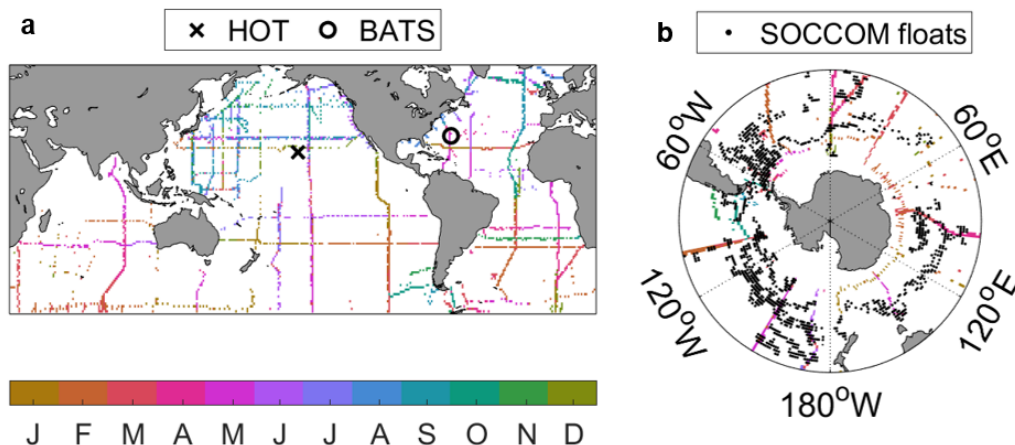


FIGURE B.1: DIC observations at 10 m from GLODAPv2.2019 from 2004 through 2017. Globally (a) and for the Southern Ocean (b). The month of the GLODAP measurement is illustrated in color. On repeat hydrographies, the later month is illustrated. The location of independent validation data from the HOT and BATS time-series stations (a) and BGC Argo floats (b) are marked in black.

Here, we deploy a method based on the 2-step SOM-FFN technique by Landschützer et al. (2013). We first cluster the global ocean into regions using self-organizing maps (SOMs), and then apply a feed-forward network (FFN) in each of these regions, to create the first observation-based monthly climatology of DIC in the interior ocean. Our resulting data product is mapped on a $1^\circ \times 1^\circ$ grid from 65°N to 65°S on 33 depth levels between 2.5 m and 1975 m.

We demonstrate that the resulting DIC field adequately reproduces independent measurements from time-series and biogeochemical float observations. Building on this novel data product we investigate the relative contribution of each available driver on the seasonal amplitude of DIC. Finally, we use the seasonal variations in the DIC field to calculate the depth where primary production dominates over respiration and further calculate the carbon draw-down linked to NCP, providing the first global estimation of summer NCP based on DIC measurements.

2 Data and Methods

2.1 Reconstructing global mapped fields of DIC using SOM-FFN

We use the 2-step SOM-FFN approach by Landschützer et al. (2013) with the DIC observations from GLODAPv2.2019 throughout the upper 2000 m. The SOM-FFN method first clusters the global ocean into regions of similar biogeochemical properties using SOMs. In a second step, it runs an FFN in each cluster to establish the statistical relationship between the measured DIC and a set of physical and biogeochemical predictors. Next, global fields of these predictors are used to project the statistically modeled DIC into the ocean for each month and depth. This section provides a summary of the SOM-FFN approach and some of the adjustments made from the approach described by Landschützer et al. (2013). A more detailed description of our method and data can be found in the Supplementary Information B_S1 - B_S4.

Here, we apply and extend the SOM-FFN method using DIC as the target variable for the mapping. We map DIC not only at the sea surface, but also throughout the upper water column from the surface until ~ 2000 m. We use the DIC measurements from GLODAPv2.2019 from 2004 through 2017 (Olsen et al., 2019) as the input for the FFN (Fig. B.1). This temporal restriction reduces the impact of the long-term trend in DIC, driven primarily by the oceanic uptake of anthropogenic CO_2 from the atmosphere. The method reconstructs the non-linear best-fit relationship between all of the available observations and a set of physical and biogeochemical predictor data. These predictor data exist on a global scale, hence the reconstructed relationship can be applied where no observations exist to fill the data gaps (see Landschützer et al. (2013) and Supplementary Information B_S1 - B_S4).

As predictor data, we chose representative proxies for the effect of ocean physics, chemistry, and biology on the DIC field. We use optimally interpolated temperature and salinity fields based on Argo floats (Argo, 2019; Roemmich and Gilson, 2009), and optimally interpolated fields of silicate, nitrate, and dissolved oxygen from the World Ocean Atlas 2018 (Garcia et al., 2019). The predictors have a known interaction with DIC and are available as monthly global mapped fields in the water column. Our output consists of monthly mean fields of DIC based on the period from 2004 through 2017, on 33 depth levels between 2.5 m and 1975 m on a $1^\circ \times 1^\circ$ grid from 65°N to 65°S .

2.2 Smoothing and uncertainty within the method

The internal validation of the SOM-FFN method is based on a randomly chosen subsample of the available observations by the network (see Supplementary Information B_S3). Therefore, the resulting DIC fields vary slightly each time we run the network. To account for potential biases in the separation between training and validation data, we use a bootstrapping

approach and run the SOM-FFN method ten times and take the mean of this ensemble, resulting in a smoother end product than a single ensemble member. We define the generalization uncertainty within the method as the standard deviation across this ensemble. The mapped ensemble mean fields are further smoothed at each depth level with a scalar function-based filtering using the mean of the neighboring three grid cells in each direction except depth (month, latitude, and longitude). We estimate the seasonal cycle by applying a non-linear least squares harmonic fit at each grid cell, at each depth level. Our final neural-network derived estimate of DIC is hereafter called DIC_{NN} (Table B.1).

2.3 Test with synthetic data

In addition to validating our method with independent measurements, we test our method with synthetic data. We take the model field from the ocean biogeochemistry model HAMOCC (Ilyina et al., 2013; Mauritsen et al., 2019), which was run on a $1.5^\circ \times 1.5^\circ$ grid in hindcast mode with historic atmospheric forcing for the Global Carbon Budget 2018 (Le Quéré et al., 2018). We first re-grid the HAMOCC output onto the same grid and format as the observational predictor and target data (monthly means between 2004 through 2017, 33 depth levels between 2.5 m and 1975 m, $1^\circ \times 1^\circ$ grid, from 65°N to 65°S). We call the full model field of DIC in HAMOCC hereafter DIC_{HAMOCC} (Table B.1).

To test how well our method reconstructs the full model field, we subsample DIC_{HAMOCC} at the month and location where we have DIC observations in GLODAPv2.2019. We then use the same SOM-FFN set-up (as described in full detail in Supplementary Information B_S1 - B_S3) and run the method using the same predictors, but from HAMOCC, to estimate the DIC in HAMOCC (hereafter $DIC_{NN.HAMOCC}$). Finally, we compare $DIC_{NN.HAMOCC}$ with DIC_{HAMOCC} .

2.4 Test with independent measurements

We further compare our estimate with data from independent time-series sites that were not fed into the network and have a long enough record to extract the mean seasonality. Although there are many time-series stations across the globe (Bates et al., 2014) (See also https://www.nodc.noaa.gov/ocads/oceans/time_series_moorings.html), only a few stations measured DIC in the upper ocean from 2004 through 2017 and at locations that are not excluded in our product (i.e., coastal regions and latitudes poleward of 65°). The time-series stations that fall within our temporal and spatial domains are the Hawaii Ocean Time-Series (HOT) (Dore et al., 2009) and the Bermuda Atlantic Time Series Study (BATS) (Bates et al., 2014).

The HOT (http://www.soest.hawaii.edu/HOT_WOCE/ftp.html) and BATS (http://batsftp.bios.edu/BATS/bottle/A_README_BOTTLE.txt) databases consist of physical and BGC ship data. The DIC measurements that form a part of these time-series datasets were taken from bottled sea-water samples. The HOT time-series extends from 1988 through 2017 for the upper ocean at 22°45'N, 158°00'W, north of Hawaii, while the BATS time series extends from 1988 through 2016 at 31°40'N, 64°10'W (Fig. B.1a).

For the validation, we compile all DIC measurements from the HOT and BATS databases and only keep the data that overlap with the period from our study (2004 through 2017). At BATS, while conducting our analysis, data from 2017 were not available, so here the dataset ends in December 2016. We then compute a monthly climatology by taking the mean monthly values. While the HOT data extends to 1000 m, at BATS, only a few observations exist below 600 m, so here we only use the top 600 m for our validation.

We test DIC_{NN} at the $1^\circ \times 1^\circ$ grid point closest to the HOT location (hereafter $DIC_{NN.HOT}$) and compare it to the measured DIC at the HOT station (hereafter DIC_{HOT}). We also test how DIC_{HAMOCC} at the grid point closest to HOT (hereafter $DIC_{HAMOCC.HOT}$) compares to our estimate thereof (hereafter $DIC_{NN.HAMOCC.HOT}$, Table B.1).

Similarly, we test DIC_{NN} at the $1^\circ \times 1^\circ$ grid point closest to the BATS location (hereafter $DIC_{NN.BATS}$) and compare it to the measured DIC at the BATS station (hereafter DIC_{BATS}). We then test how DIC_{HAMOCC} at the grid point closest to BATS (hereafter $DIC_{HAMOCC.BATS}$) compares to our estimate thereof (hereafter $DIC_{NN.HAMOCC.BATS}$, Table B.1).

To test our method in the southern hemisphere, we use data from BGC Argo floats that take measurements as part of the Southern Ocean Carbon and Climate Observation and Modelling project (SOCCOM). We compare the monthly mean DIC concentration calculated from the SOCCOM floats to our neural-network derived estimate of the DIC concentration at the month and location of the float measurements ($DIC_{NN.SOCCOM}$). The DIC from the SOCCOM floats is calculated using a combination of pH measurements, total alkalinity estimated using the commonly used LIAR algorithm (Carter et al., 2018), and the CO₂SYS analysis tool (Heuven et al., 2011). As the SOCCOM float data is only available after 2014, we compute the monthly climatology of DIC from 2014 through 2017 on a $1^\circ \times 1^\circ$ grid and linearly interpolate the result onto our 33 depth levels (hereafter DIC_{SOCCOM}). In the domain until 65°S, there are, on average, 160 grid cells with SOCCOM floats in each month of the year (Fig. B.1b). The data density of the SOCCOM floats is relatively high, although the period of these observations only extends over four years (2014 through 2017). Lastly, we test how DIC_{HAMOCC} at the grid points closest to the SOCCOM floats (hereafter $DIC_{HAMOCC.SOCCOM}$) compares to our estimate thereof (hereafter $DIC_{NN.HAMOCC.SOCCOM}$, Table B.1).

TABLE B.1: Different data sets used for external validation of our method. Unless otherwise stated, the data sets are on a $1^\circ \times 1^\circ$ grid from 65°N to 65°S , on 33 depth levels from the sea surface until 1975 m.

Data set	Description
DIC_{NN}	Our neural-network based estimate of DIC. A monthly mapped climatology based on the period from 2004 through 2017.
$\text{DIC}_{\text{LAUVSET}}$	The annual mean mapped climatology by Lauvset et al. (2016). Reference year: 2002.
$\text{DIC}_{\text{HAMOCC}}$	The full model field of DIC in the Ocean Biogeochemistry Model HAMOCC. A monthly mapped climatology based on the period from 2004 through 2017.
$\text{DIC}_{\text{NN.HAMOCC}}$	Our neural-network based reconstruction of $\text{DIC}_{\text{HAMOCC}}$.
$\text{DIC}_{\text{NN.HAMOCC.HOT}}$	$\text{DIC}_{\text{NN.HAMOCC}}$ at the $1^\circ \times 1^\circ$ grid point closest to HOT.
$\text{DIC}_{\text{HAMOCC.HOT}}$	$\text{DIC}_{\text{HAMOCC}}$ at the $1^\circ \times 1^\circ$ grid point closest to HOT.
$\text{DIC}_{\text{NN.HAMOCC.BATS}}$	$\text{DIC}_{\text{NN.HAMOCC}}$ at the $1^\circ \times 1^\circ$ grid point closest to BATS.
$\text{DIC}_{\text{HAMOCC.BATS}}$	$\text{DIC}_{\text{HAMOCC}}$ at the $1^\circ \times 1^\circ$ grid point closest to BATS.
$\text{DIC}_{\text{NN.HAMOCC.SOCCOM}}$	$\text{DIC}_{\text{NN.HAMOCC}}$ at the $1^\circ \times 1^\circ$ grid point closest to the SOCCOM floats.
$\text{DIC}_{\text{HAMOCC.SOCCOM}}$	$\text{DIC}_{\text{HAMOCC}}$ at the $1^\circ \times 1^\circ$ grid point closest to SOCCOM.
DIC_{HOT}	Monthly mean values of the DIC measurements at the HOT station from 2004 through 2017.
$\text{DIC}_{\text{NN.HOT}}$	DIC_{NN} at the $1^\circ \times 1^\circ$ grid point closest to HOT.
DIC_{BATS}	Monthly mean values of the DIC measurements at the BATS station from 2004 through 2016.
$\text{DIC}_{\text{NN.BATS}}$	DIC_{NN} at the $1^\circ \times 1^\circ$ grid point closest to BATS.
$\text{DIC}_{\text{SOCCOM}}$	Monthly mean values of the DIC measurements from SOCCOM floats from 2014 through 2017.
$\text{DIC}_{\text{NN.SOCCOM}}$	DIC_{NN} at the $1^\circ \times 1^\circ$ grid point closest to the SOCCOM floats.

2.5 Seasonal response function

To investigate how each of the predictors contributes to the seasonal changes in DIC, we compute the seasonal response function for each of the predictors. We use an approach similar to the “profile method” described in Gevrey et al. (2003), which is commonly used in sensitivity analyses to determine how changes in the predictors affect the target data in a neural network. In the profile method, the network is trained as usual (see Supplementary Information B_S3), and in the simulation step, one predictor is consecutively varied while holding the remaining predictors constant. As we are interested in the seasonal response in different regions, we use a similar approach to the profile method, but we only hold the time dimension constant, while varying in space.

Our method works as follows: We first calculate DIC_{base} by training the network as usual and then apply the network while keeping all predictors constant in time (i.e., using the time-mean at each grid cell). Next, we simulate the network again consecutively for each predictor, while keeping all of the predictors except the predictor under evaluation constant in time. For example, we calculate $DIC_{temperature}$ by simulating the network with all of the predictors kept constant in time, except temperature. Lastly, for each predictor, we calculate ΔDIC_{input} by subtracting the DIC_{input} of that predictor from the DIC_{base} ; for example, for temperature: $\Delta DIC_{temperature} = DIC_{base} - DIC_{temperature}$. We repeat our bootstrapping approach by simulating these ten times to calculate the mean response over the ensemble.

2.6 Nodal depth and summer NCP

To investigate the effect of primary production on the seasonal cycle of DIC, we first compute the nodal depth. Above and below the nodal depth, the phase of the seasonal cycle of DIC differs, due to the opposing effects of primary production near the surface and remineralization below. We determine the nodal depth as the depth where the amplitude of the seasonal cycle of DIC is minimal, while it increases both upward and downward of the nodal depth.

To determine the summer NCP, we solve the following diagnostic equation following Gruber et al. (1998) and Keeling et al. (2004) (Eq. B.1):

$$\int NCP dz = \int \frac{DIC_{norm}}{dt} dz + F_{air.sea} - F_{diff} - F_{entr} + F_{hor.div} \quad (B.1)$$

where $\int NCP dz$ is the NCP between the surface and the base of the euphotic zone, $\int \frac{DIC_{norm}}{dt} dz$ is the change in time of the integrated salinity normalized DIC from the surface until the base of the euphotic zone, $F_{air.sea}$ is the integrated air-sea CO_2 flux over hemispheric summer, F_{diff} is the mean vertical diffusive flux over hemispheric summer, F_{entr} is the mean entrainment flux over hemispheric summer, and $F_{hor.div}$ is the horizontal

divergence of the horizontal transport.

For the following calculations, unless otherwise stated, we use mean monthly climatologies from 2004 through 2017 on a $1^\circ \times 1^\circ$ grid. Hereafter, April to October and October to April are called hemispheric summer (for the northern and southern hemisphere, respectively).

We compute the euphotic zone, i.e., where biology acts as a main driver on the DIC, following Morel et al. (2007), and using SeaWiFS chlorophyll-a data (from the NASA ocean color website https://oceancolor.gsfc.nasa.gov/cgi/13?sen=S&per=M0&prod=CHL_chlor_a).

We then convert the DIC concentration (in $\mu\text{mol kg}^{-1}$) to DIC content (in mol m^{-3}) using the density based on the Argo climatology (Roemmich and Gilson, 2009). Next, we solve the first term using our DIC estimate, which we normalize following Friis et al., 2003, and the mean base of the euphotic zone over hemispheric summer. For the second term, we use the updated Landschützer et al. (2014) product based on its latest extension in time presented in Keppler and Landschützer (2019) to calculate the time integral of the air-sea CO_2 flux over the hemispheric summer. We solve the third term using Eq. B.2 and our DIC estimate:

$$F_{diff} = -k_z \frac{dDIC}{dz} \text{ (at base of euphotic zone)} \quad (\text{B.2})$$

where k_z is the diffusivity (we use a constant value of $-4 \times 10^{-4} \text{ m}^2 \text{ s}^{-1}$). We solve the fourth term using Eq. B.3 and our DIC estimate:

$$F_{entr} = -\frac{dh}{dz} \frac{dDIC}{dz} \text{ (at base of mixed layer)} \quad (\text{B.3})$$

where h is the mixed layer depth (MLD), and $\frac{dh}{dz}$ is the entrainment rate, i.e. how fast the MLD deepens over hemispheric summer. We use the monthly climatology of the MLD by Holte et al. (2017) and apply an optimal interpolation to fill observational gaps and compute the mean MLD over hemispheric summer. This term is only relevant when the MLD is deeper than the base of the euphotic zone (i.e., in the high latitudes). We cannot solve $F_{hor.div}$, so we neglect it. Unlike other studies (Ostle et al., 2015), we do not correct for the formation of calcium carbonate due to the lack of global available NO_3 and total alkalinity data.

Accounting for the air-sea CO_2 flux, the vertical diffusive flux, and the entrainment flux, we obtain an estimate of the summer NCP, i.e. the net amount of carbon taken up by biology between hemispheric spring and autumn.

Using standard error propagation, we estimate the error of the NCP calculation based on Eq. B.4:

$$error = \sqrt{e_1^2 + e_2^2 + e_3^2} \quad (\text{B.4})$$

where e_1 is the percent-error based on the air-sea CO_2 flux ($\sim 17\%$, Roobaert et al., 2019), e_2 is the error within the method, based on our bootstrapping approach of running the network 10 times. We estimate e_2 from the spread across the ensemble, which amounts to $11.5 \mu\text{mol}/\text{kg}$ or in percent-terms $\sim 0.5\%$ of the mean DIC field. Lastly, we estimate the error resulting from the mismatch towards DIC measurements. Our approach per definition reduces the mean bias towards 0; however we find regionally larger discrepancies as illustrated by the root mean squared error (RMSE) between our product and available measurements (see Supplementary Information Fig. B_SI.4). As we have little knowledge regarding the RMSE where no observations exist, we use a conservative approach and calculate e_3 based on the maximum RMSE observed from both dependent and independent data. As identified in Supplementary Information Fig. B_SI.4, the RMSEs remain below $50 \mu\text{mol}/\text{kg}$ or $\sim 2\%$ of the mean DIC concentration. We further remain conservative and assume the RMSE is uncorrelated and constant throughout the water column, resulting in a percent error of 2% for e_3 . We do not add error estimates from the remaining terms (F_{diff} and F_{entr}) as we lack a mechanistic understanding of the uncertainties and also because their contribution to the overall NCP is minor compared to the other terms we considered. In addition, as mentioned above, we had to neglect the horizontal transport divergence. This adds further uncertainty, which we cannot quantify. Solving with e_1 - e_3 , we get an overall error of the NCP of 17% , which is largely due to the error in the air-sea CO_2 flux.

3 Results

3.1 Mean DIC fields

Our new data product DIC_{NN} portrays the well-known mean DIC distribution (Fig. B.2 and B.3a,d,g), such as the latitudinal surface gradient primarily driven by temperature and upwelling (Wu et al., 2019). We find the lowest DIC concentrations near the ocean surface, and the global average concentrations increase with depth from $2044 \mu\text{mol kg}^{-1}$ at the surface to $2270 \mu\text{mol kg}^{-1}$ at 1975 m . This increase in DIC with depth is known to be due to the biological uptake near the surface and remineralization at depth, as well as the accumulation of “older” water (i.e., water that has been out of contact with the atmosphere for longer) along the trajectory flow (Heinze et al., 2015). The isopycnals depicted in Fig. B.3 a,d,g further demonstrate that the mean DIC profile largely follows the profile of the water masses.

The DIC_{NN} concentration in the top 500 m displays well known spatial features following the large-scale ocean circulation. For example, in the upwelling region of the eastern and equatorial Pacific, upwelled carbon-rich deep water increases the surface DIC concentration in this region. In the intermediate waters ($\sim 500 \text{ m}$ to $\sim 1500 \text{ m}$), the distribution of DIC becomes more uniform. Exceptions are in deep-water formation regions such as the North Atlantic and the Southern Ocean, which have lower DIC

concentrations than the northern Indo-Pacific. In the deep ocean, the DIC concentration is the highest and the most uniform, with the most DIC in the northern Indo-Pacific and the least in the North Atlantic. As the deep water in the North Pacific is the "oldest," i.e., it has been out of contact with the atmosphere for ~ 1500 years, the largest amounts of DIC are stored here (Heinze et al., 2015; Sarmiento and Gruber, 2006).

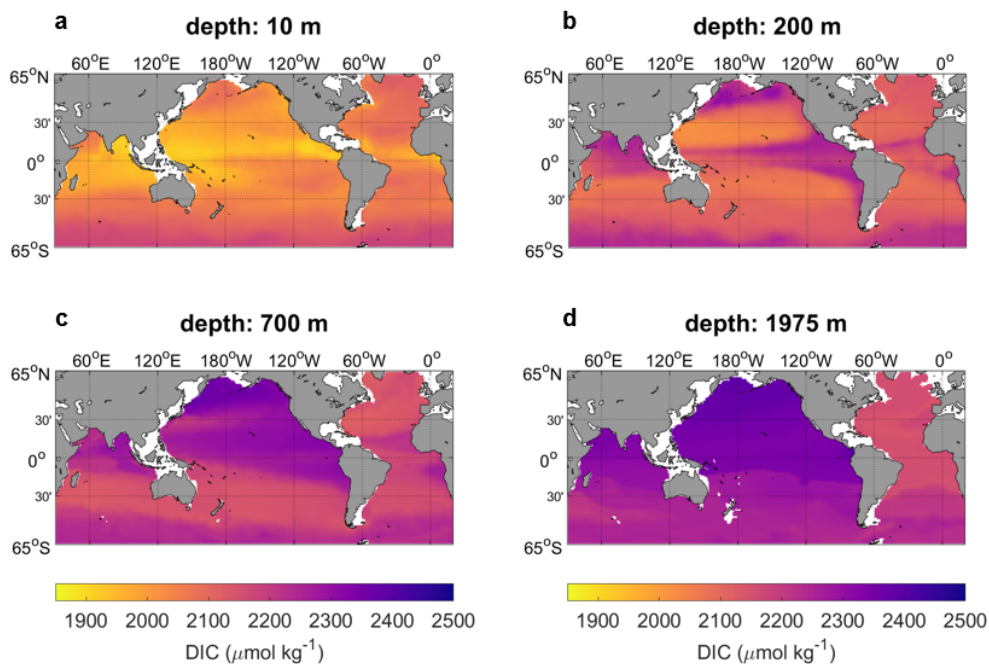


FIGURE B.2: Spatial distribution of the time-mean DIC. Illustrating DIC on 4 depth levels. a) 10 m, b), 200 m, c) 700 m, d) 1975 m.

Comparing Fig. B.2 with Fig. B.1 reveals the degree of extrapolation within our method. Per definition, our global approach minimizes the mean mismatch between measurements that the resulting mean bias equates to 0. Regionally, however, we find a larger mismatch illustrated by RMSE exceeding $40 \mu\text{mol}/\text{kg}$ or roughly 2% in the Atlantic Ocean (see Supplementary Information Fig. B_SI.4). Additionally, we expect larger local uncertainties in unsampled (i.e. unsampled after 2004) regions such as the Indian Ocean north of the equator and the Arabian Sea. The lack of independent observations, however, prohibits us from quantifying this mismatch. We, therefore, turn towards a comparison with results from an extrapolation using a different method.

We compare our annual mean DIC_{NN} field to the annual climatology by Lauvset et al. (2016). That product is on a $1^\circ \times 1^\circ$ grid and is normalized to the year 2002. To compare the two estimates, we linearly interpolate the Lauvset climatology onto the same 33 depth levels as our product (hereafter $\text{DIC}_{LAUVSET}$) and compute the annual mean of DIC_{NN} . Generally, the two estimates agree on the distribution, but our estimate tends to have higher concentrations near the surface and lower concentrations in the interior (Fig.

B.3). The former can be linked to the difference in reference year: $DIC_{LAUVSET}$ is scaled to the year 2002, and DIC_{NN} is based on data after 2004, centered around the years 2010/2011. Hence, we expect that DIC_{NN} has more DIC near the surface than $DIC_{LAUVSET}$ due to the accumulation of anthropogenic carbon. The expected increase in surface ocean DIC due to the atmospheric perturbation is $\sim 1.1 \mu\text{mol kg}^{-1} \text{ yr}^{-1}$ or $\sim 11 \mu\text{mol kg}^{-1}$ between 2002 and 2011 (following Sarmiento and Gruber, 2006). The positive differences near the surface approximately match the expected increase over one full decade: DIC_{NN} in the top 200 m is approximately $13 \mu\text{mol kg}^{-1}$ higher than $DIC_{LAUVSET}$, indicating that most of the differences between the two estimates at the surface can be explained by the anthropogenic perturbation.

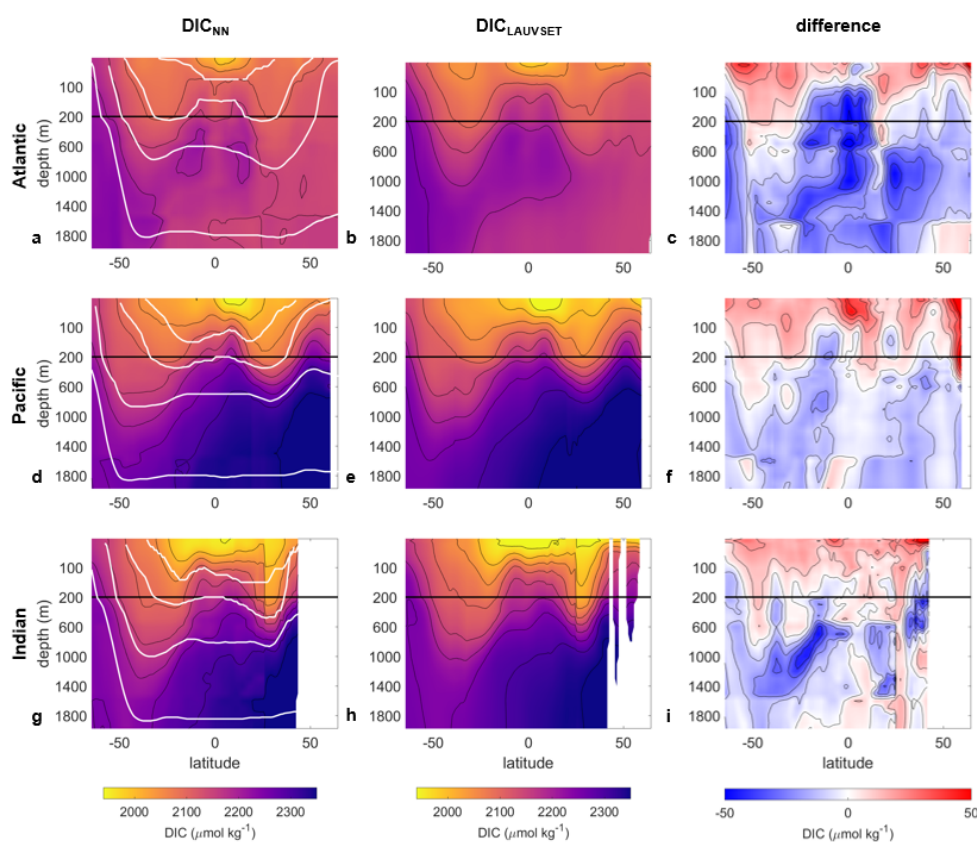


FIGURE B.3: Comparison between $DIC_{LAUVSET}$ and DIC_{NN} . Zonal mean of the annual mean DIC_{NN} (a,d,g), $DIC_{LAUVSET}$ (b,e,h), and the difference between the two ($DIC_{NN} - DIC_{LAUVSET}$) (c,f,i). For each of the three sectors: Atlantic (a-c), Pacific (d-f); Indian (g-i). Zoomed into the top 200 m (delimited in black). Some isopycnals are illustrated as white lines in a,d,g (from top to bottom: 24.5, 26.2, 27.6, and 28.4 kg m^{-3}).

In addition to this offset near the surface, our estimate in the interior (below ~ 200 m) is, on average, $\sim 10 \mu\text{mol kg}^{-1}$ lower than $DIC_{LAUVSET}$, which cannot simply be explained by the difference in reference years. Furthermore, there is a striking difference between the two estimates in the Atlantic sector between ~ 100 m and 1000 m, where the time-average of DIC_{NN} is lower by $\sim 50 \mu\text{mol kg}^{-1}$ than $DIC_{LAUVSET}$. This region of high DIC in the Lauvset product may be explained by data availability. All of the

available information here stems from a single cruise (33MW19930704) as well as a few calculated DIC values (based on observed total alkalinity and pH) from cruise 74DI19980423. The DIVA mapping used by Lauvset et al. (2016) draws no other information apart from the observations directly, the correlation length scale, and the signal-to-noise ratio. The latter two are subjectively chosen, and for $DIC_{LAUVSET}$, the signal-to-noise ratio is such that the observations are considered climatologically representative, and therefore, closely fit. Our method, however, takes the high DIC values in the Atlantic in combination with the additional information from the predictor data, and thus, DIC_{NN} might be more representative of the true climatological state. In addition, the differences in the ocean interior could be due to the difference in the timespan. While our approach only considers measurements between 2004 and 2017, the approach by Lauvset et al. (2016) also includes measurements from earlier campaigns.

The results of the tests, nevertheless, are mostly within the $40 \mu\text{mol}/\text{kg}$ RMSE spread identified from the direct measurement comparison. Exceptions include the already mentioned Atlantic Ocean at intermediate depths, but also the high latitude North Pacific and Indian Ocean, where we do not have any direct measurements after 2004.

Additionally, we can turn to the synthetic data to estimate the accuracy of our reconstruction. Run with synthetic data, the SOM-FFN method is capable of reconstructing the mean DIC_{HAMOCC} distribution, as illustrated in Fig. B.4. The differences between DIC_{HAMOCC} and $DIC_{NN.HAMOCC}$ remain within $10 \mu\text{mol kg}^{-1}$ for the majority of the ocean, strengthening our trust in the reconstructed DIC field. However, a few exceptions exist where differences reach $50 \mu\text{mol kg}^{-1}$ and more in the deep Indian and Pacific Ocean, where fewer observations exist, illustrating again that regional uncertainties can be significantly larger in this global approach. In summary, we have confidence that we can reconstruct the mean field locally within error bounds of $50 \mu\text{mol}/\text{kg}$ ($\sim 2\text{-}3\%$) of the observed concentration.

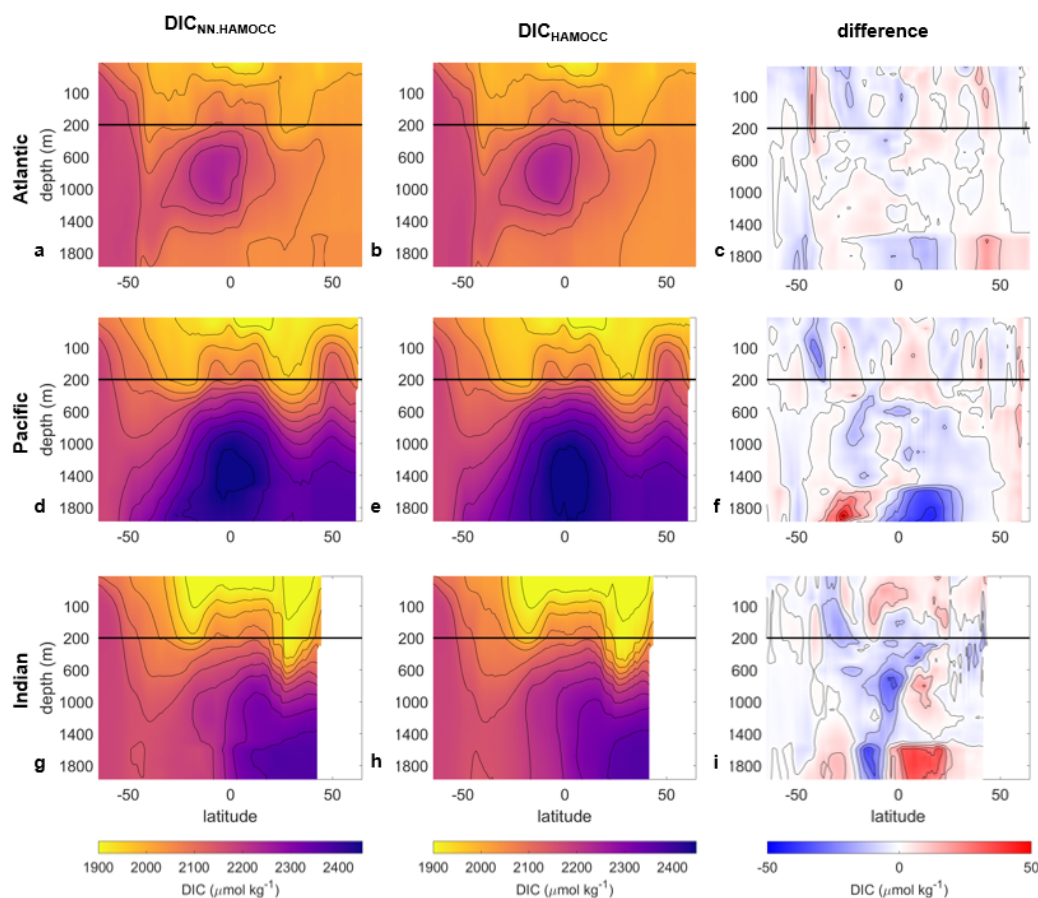


FIGURE B.4: Comparison between the DIC_{HAMOCC} and $DIC_{NN.HAMOCC}$. Zonal mean of the $DIC_{NN.HAMOCC}$ (a,d,g), DIC_{HAMOCC} (b,e,h), and the difference between the two ($DIC_{NN.HAMOCC} - DIC_{HAMOCC}$) (c,f,i). For each of the three sectors: Atlantic (a-c), Pacific (d-f); Indian (g-i). Zoomed into the top 200 m (delimited in black).

3.2 Regional seasonal cycles of surface DIC

Dividing the ocean into coarse latitudinal bands, we find that the mean surface seasonal cycle of DIC has the largest amplitude in the temperate regions, especially in the northern hemisphere with $\sim 32 \mu\text{mol kg}^{-1}$, intermediate in the subtropical regions with amplitudes of $\sim 15 \mu\text{mol kg}^{-1}$, and weakest in the tropical regions ($\sim 8 \mu\text{mol kg}^{-1}$), where the seasonal atmospheric forcing is weakest (Fig. B.5a,c). Unsurprisingly, the mean phase is approximately opposite in the two hemispheres, with the highest surface DIC concentrations in early spring when vertical mixed layers tend to be deepest (Holte et al., 2017). The deep mixing brings DIC-rich waters to the surface, increasing the respective concentration. Conversely, the surface DIC is lowest in early autumn when vertical mixing tends to be minimal. However, the phase and amplitude of the seasonal cycle vary regionally and with the onset of local phytoplankton blooms.

To ensure the seasonality illustrated is not only due to salinity patterns, we also demonstrate the mean seasonal cycle in the same climate regions as in Fig. B.5a,c, but for DIC that we normalized with salinity (Fig. B.5b,d),

following the method by Friis et al. (2003). The surface seasonal cycle of the normalized DIC agrees relatively well with the surface seasonal cycle of DIC in terms of its amplitude and phase.

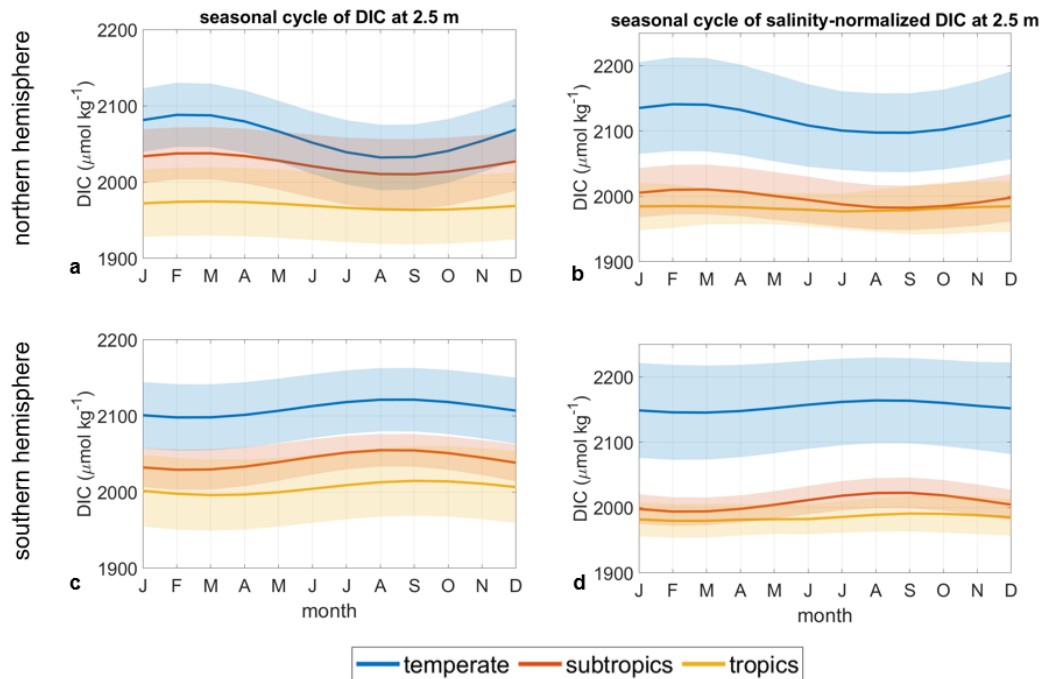


FIGURE B.5: Mean seasonal cycle of DIC_{NN} at 2.5 m in different climate regions. Temperate (35° to 65° , blue), subtropical (23° to 35° , orange), and tropical (0° to 23° , yellow) for the northern (a-b) and southern (b-c) hemispheres. The mean of each region (solid lines) is bound by the standard deviation within that region (shading); a,c are DIC concentration, and b,d are for DIC normalized with salinity. The boundaries for the climate regions are illustrated on the map grid in Fig. B.6a.

While throughout most of the ocean, the amplitude of the surface seasonal cycle of DIC is between 5 and $20 \mu\text{mol kg}^{-1}$ (median of $14 \mu\text{mol kg}^{-1}$), some areas with considerably larger signals exist, particularly in the northern high latitudes, but also in upwelling regions (Fig. B.6a). In the high latitude near-shore North Pacific, the amplitude extends beyond $50 \mu\text{mol kg}^{-1}$. Likewise, in the high latitude North Atlantic, the amplitude ranges between 30 and $50 \mu\text{mol kg}^{-1}$. In the northern hemisphere, the month of the largest DIC concentrations is mostly March, but it varies from January to April (boreal spring, Fig. B.6b).

Amplitudes in the subtropics in both the Pacific and Atlantic Ocean are considerably lower. Interestingly, this clear and distinct latitudinal pattern observed in the northern hemisphere does not exist in the southern hemisphere. Here, the high southern latitudes do not display significantly higher seasonal amplitudes than the lower latitudes. Plausible explanations are that upwelled water masses in combination with a weaker biological uptake dampen the seasonal cycle of DIC in austral spring/summer. In the southern hemisphere, August and September are mostly the months with the highest DIC concentrations throughout the year, with some variance

from July to December (austral spring). The phase of the seasonal cycle of DIC in the northern Indian Ocean is similar to the southern hemisphere. This may be a monsoon feature, i.e. the northern hemisphere seasonality matches the southern hemisphere due to the forcing from monsoon seasons.

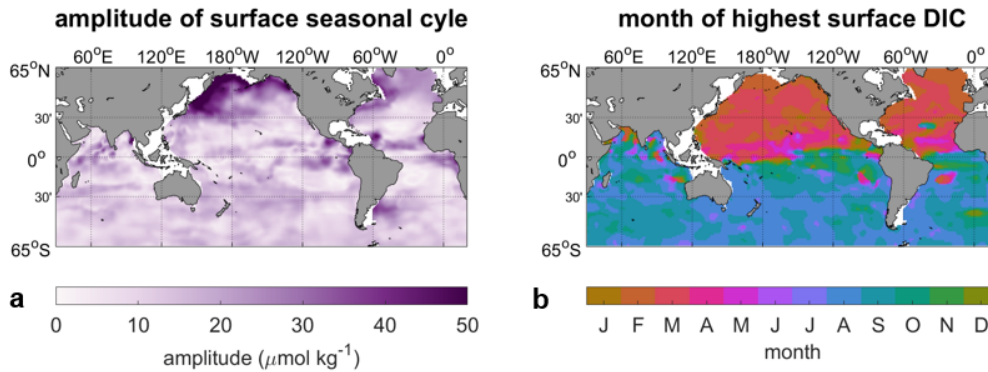


FIGURE B.6: The amplitude and phase of the seasonal cycle of DIC_{NN} near the surface. (a) Mean amplitude of the seasonal cycle of DIC_{NN} between 2.5 m and 20 m. (b) month with the highest DIC values at 2.5 m. The latitude grid in (a) delimits the boundaries for the climate regions in Fig. B.5.

Near the sea surface, i.e., where we observe the largest seasonal amplitude in the different climate regions (Fig. B.7), we find that most of the seasonal changes of surface DIC are linked to temperature as our main predictor. Temperature is inversely linked to DIC (Takahashi et al., 2002) and contributes to the seasonality two-fold. Colder waters are linked to higher solubility and increased vertical mixing, and both increase the surface DIC pool (Heinze et al., 2015; Sarmiento and Gruber, 2006). In the temperate regions, nitrate, representing nutrient input to the surface, also significantly affects the seasonal cycle of surface DIC, highlighting the importance of including upwelling and biology in reconstructing the seasonal cycle. Nutrient availability through vertical mixing or river input triggers biological production, lowering the DIC concentration at the surface (Sarmiento and Gruber, 2006; Takahashi et al., 2002). Hence, the effects of temperature and biology are competing in the temperate regions and both need to be considered to reconstruct the seasonal DIC cycle faithfully. The remaining proxies, i.e. salinity, oxygen, and silicate play overall a smaller statistical role in our reconstruction. The temperature dominance indicates the possibility to even reconstruct lower frequency signals using this method. In the tropical regions, where the seasonal forcing is comparatively weak, the different predictors do not differ significantly in their dominance.

While we can identify some clear large scale patterns, Fig. B.6 remains still patchy in places. In particular, high amplitudes in the tropical Pacific and tropical Atlantic suggest that inter-annual variability linked to tropical modes such as ENSO (Feely et al., 2006) obscure this refined analysis. Likewise, strong amplitudes in the northern Indian Ocean or Patagonian shelf might be linked to data paucity. Lacking the observational constraints to test the uncertainty in our reconstructed seasonal amplitude, we turn to

test our reconstruction with our synthetic data set.

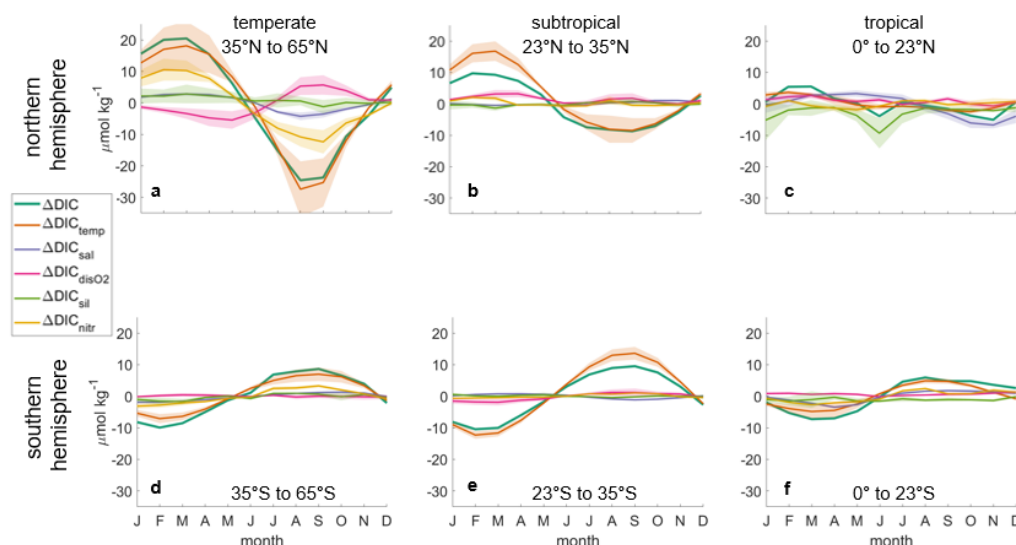


FIGURE B.7: The seasonal response function at 2.5 m in different climate regions. Temperate (a,d; 35° to 65°), subtropical (b,e; 23° to 35°), and tropical (c,f; 0° to 23°) for the northern (a-c) and southern (d-f) hemisphere, $\Delta\text{DIC}_{\text{temperature}}$ (orange), $\Delta\text{DIC}_{\text{salinity}}$ (purple), $\Delta\text{DIC}_{\text{dissolvedoxygen}}$ (magenta), $\Delta\text{DIC}_{\text{silicate}}$ (light green), $\Delta\text{DIC}_{\text{nitrate}}$ (yellow). The mean of the 10-member ensemble is illustrated as solid line, and one standard deviation around the mean in shading. ΔDIC (dark green) is the mean seasonal anomaly at 10 m from our data estimate.

The surface seasonal cycle of $\text{DIC}_{\text{NN.HAMOCC}}$ in large scale regions remains close to the seasonal cycle of $\text{DIC}_{\text{HAMOCC}}$ (Fig. B.8), with the maximum difference between $\text{DIC}_{\text{HAMOCC}}$ and $\text{DIC}_{\text{NN.HAMOCC}}$ of $11 \mu\text{mol kg}^{-1}$ in the northern temperate band, where the full model field is a bit jagged, and so $\text{DIC}_{\text{NN.HAMOCC}}$ is lower in boreal spring and higher in boreal summer. For most of the global ocean, $\text{DIC}_{\text{NN.HAMOCC}}$ is in phase with $\text{DIC}_{\text{HAMOCC}}$ but underestimates the amplitude by up to $10 \mu\text{mol kg}^{-1}$. This is consistent with findings for the sea surface pCO_2 from Landschützer et al. (2014) that the SOM-FFN method underestimates observed seasonal variability. In the northern subtropics, $\text{DIC}_{\text{NN.HAMOCC}}$ is lower than $\text{DIC}_{\text{HAMOCC}}$ by up to $9 \mu\text{mol kg}^{-1}$, especially in boreal autumn and winter, while in the southern subtropics, $\text{DIC}_{\text{NN.HAMOCC}}$ is lower by up to $10 \mu\text{mol kg}^{-1}$ in austral winter. In the tropics, $\text{DIC}_{\text{NN.HAMOCC}}$ agrees best with $\text{DIC}_{\text{HAMOCC}}$, and this is likely linked to the lack of strong variations. Overall, this test demonstrates that our method, as well as the number of available observations, are well suited to reconstruct the climatological DIC distribution, and in particular, the seasonal representation of $\text{DIC}_{\text{HAMOCC}}$, adding confidence to our method.

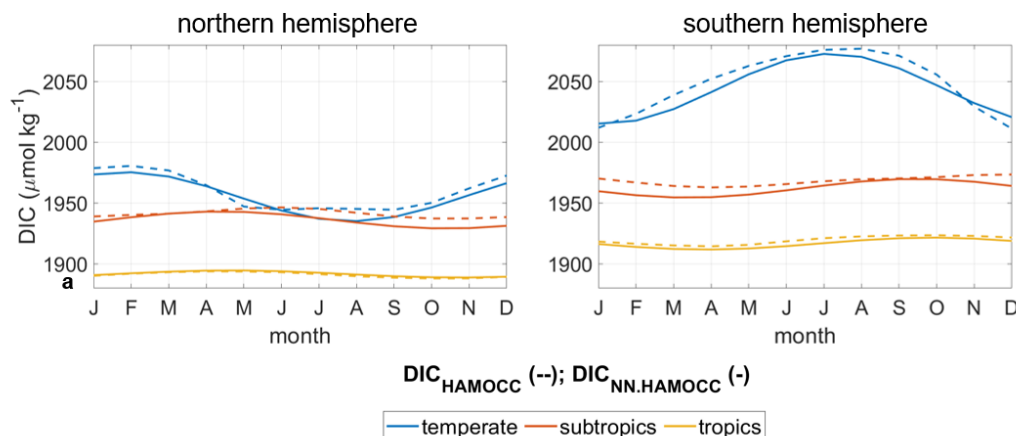


FIGURE B.8: Seasonal cycle of DIC_{HAMOCC} and $DIC_{NN.HAMOCC}$ at 10 m in different climate regions. DIC_{HAMOCC} (dashed line) and $DIC_{NN.HAMOCC}$ (solid line): Temperate (35° to 65° , blue), subtropical (23° to 35° , orange), and tropical (0° to 23° , yellow) for the northern (a) and southern (b) hemispheres.

Next, we investigate how DIC_{NN} compares to independent measurements (Fig. B.9-B.11). Although $DIC_{NN.HOT}$ represents the DIC phase and amplitude at station HOT well, it tends to underestimate DIC_{HOT} at most depths, except at 500 m depth. Most of the concentrations illustrated in Fig. B.9b are based on only a few observations. Therefore, these differences might be subject to internal variability at HOT that is not represented in $DIC_{NN.HOT}$. Both the $DIC_{NN.HOT}$ and DIC_{HOT} illustrate the weak seasonal cycle of surface DIC in the subtropics (Fig. B.9d). The DIC_{HOT} signal to noise ratio is high, and hence, no strong seasonal cycle can be observed here whereas $DIC_{NN.HOT}$ demonstrates a slightly stronger seasonal cycle. Nonetheless, given the locality of the measurements compared to the global reconstruction, the mean surface values between DIC_{HOT} and $DIC_{NN.HOT}$ compare remarkably well (1983 and 1974 $\mu\text{mol kg}^{-1}$, respectively at 10 m).

$DIC_{HAMOCC.HOT}$ is considerably lower than DIC_{HOT} (by $\sim 80 \mu\text{mol kg}^{-1}$). Nonetheless, our method reproduces the seasonal cycle of $DIC_{NN.HAMOCC.HOT}$ relatively well in terms of the mean and phase, with the highest DIC concentration in May. However, $DIC_{NN.HAMOCC.HOT}$, as observed before for the large scale regions, overestimates the amplitude of the seasonal cycle compared to $DIC_{HAMOCC.HOT}$ ($\sim 9 \mu\text{mol kg}^{-1}$ compared to $\sim 4 \mu\text{mol kg}^{-1}$).

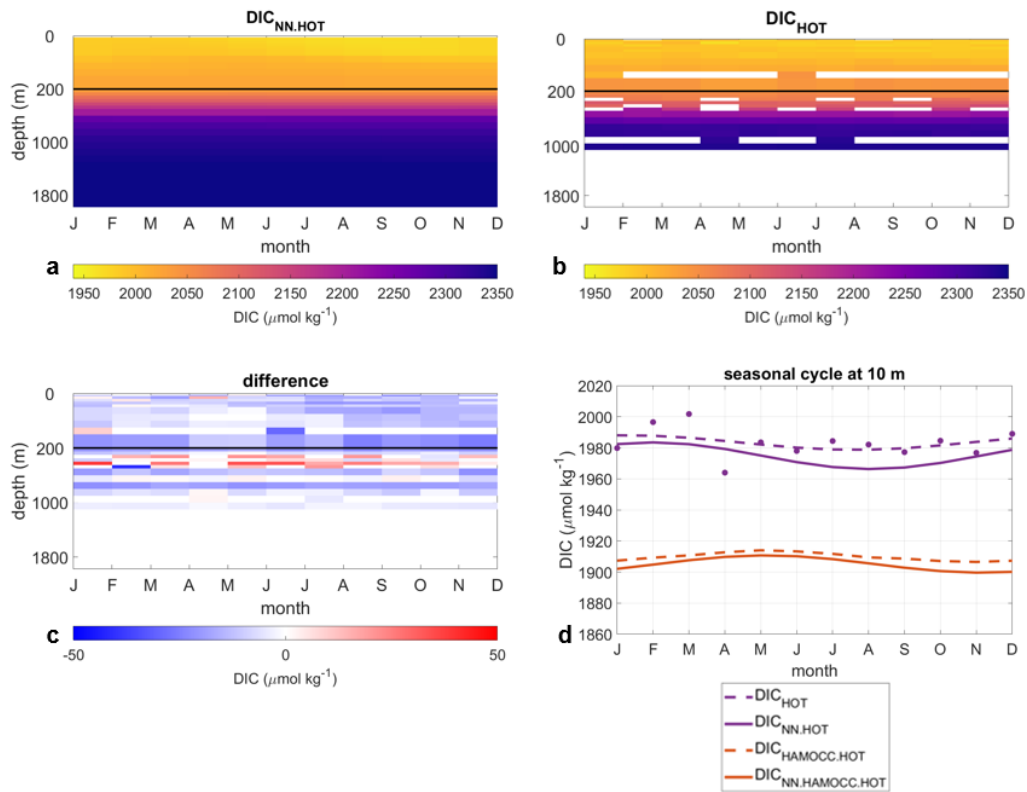


FIGURE B.9: Comparison between the DIC_{HOT} and $DIC_{NN.HOT}$. a) $DIC_{NN.HOT}$; b) DIC_{HOT} c) the difference between the two ($DIC_{NN.HOT} - DIC_{HOT}$). d) Seasonal cycle at 10 m from DIC_{HOT} (blue), $DIC_{NN.HOT}$ (green), $DIC_{HAMOCC.HOT}$ (orange), $DIC_{NN.HAMOCC.HOT}$ (purple), illustrating the calculated value (filled circles) and the least squares fit (solid lines); and a-c are zoomed into the top 200 m.

$DIC_{NN.BATS}$ demonstrates a much more pronounced seasonal DIC cycle compared to the one observed at HOT. Overall, the concentrations are higher by $\sim 5 \mu\text{mol kg}^{-1}$ than the monthly means of the measured values at DIC_{BATS} in the top 100 m, while between 100 m and 600 m it is lower by up to $18 \mu\text{mol kg}^{-1}$ (Fig. B.10). Again, given the locality of the time-series station, we find an encouraging agreement regarding the phase and amplitude of the surface seasonal cycle in $DIC_{NN.BATS}$. (Fig. B.10d). The surface seasonal cycle of DIC_{BATS} has approximately the same mean concentration as $DIC_{NN.BATS}$ (2061 and $2067 \mu\text{mol kg}^{-1}$, respectively), as well as a matching phase of the seasonal cycle (largest value in March). However, $DIC_{NN.BATS}$ underestimates the observed DIC concentrations in the winter months (up to $13 \mu\text{mol kg}^{-1}$). When comparing the mean seasonal cycle of $DIC_{HAMOCC.BATS}$, we find it again considerably lower than the DIC_{BATS} by $\sim 90 \mu\text{mol kg}^{-1}$. Our method reproduces the $DIC_{HAMOCC.BATS}$ amplitude quite accurately ($DIC_{NN.HAMOCC.BATS}$), but there is a 2-month phase shift.

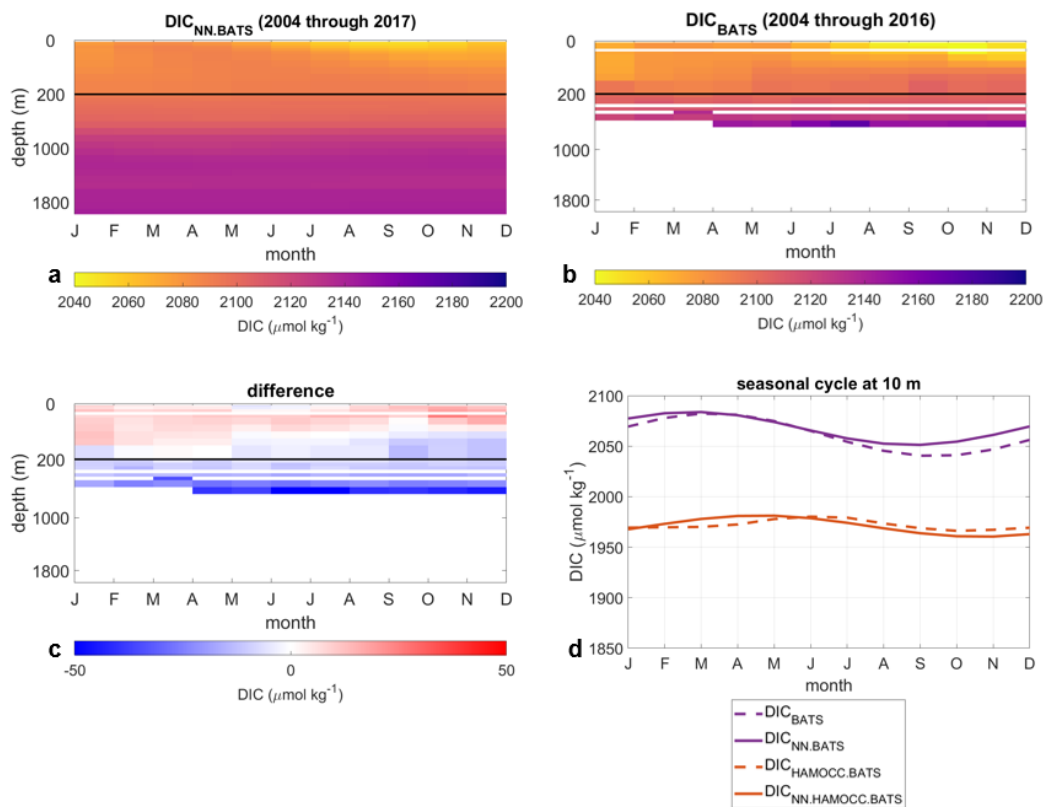


FIGURE B.10: Comparison between the DIC_{BATS} and $DIC_{NN.BATS}$. a) $DIC_{NN.BATS}$; b) DIC_{BATS} c) the difference between the two ($DIC_{NN.BATS} - DIC_{BATS}$). d) Seasonal cycle at 10 m from DIC_{BATS} (blue), $DIC_{NN.BATS}$ (green), $DIC_{HAMOCC.BATS}$ (orange), $DIC_{NN.HAMOCC.BATS}$ (purple), illustrating the calculated value (filled circles) and the least squares fit (solid lines); a-c are zoomed into the top 200 m.

Comparing the seasonal cycle in the southern hemisphere, we find that $DIC_{NN.SOCCOM}$ agrees well in phase with the DIC_{SOCCOM} , but DIC_{SOCCOM} is, on average, $16 \mu\text{mol kg}^{-1}$ higher than $DIC_{NN.SOCCOM}$ (Fig. B.11). Comparatively higher carbon values measured by the SOCCOM floats have been reported in recent studies by Williams et al. (2017), Gray et al. (2018), and Bushinsky et al. (2019), who found that SOCCOM floats demonstrated additional outgassing in austral winter months. The mean surface seasonal cycle of $DIC_{NN.SOCCOM}$ has a lower amplitude by $\sim 6 \mu\text{mol kg}^{-1}$ (Fig. B.11d), owing to the disagreement in austral winter. Comparing the mean seasonal cycle of DIC_{HAMOCC} with $DIC_{HAMOCC.SOCCOM}$, we find that the seasonal cycle in $DIC_{HAMOCC.SOCCOM}$ has a much larger amplitude (by $\sim 19 \mu\text{mol kg}^{-1}$) than DIC_{SOCCOM} , and the phase is shifted backward by ~ 2 months. However, $DIC_{NN.HAMOCC.SOCCOM}$ compares well with $DIC_{HAMOCC.SOCCOM}$, in phase, amplitude, and mean concentration.

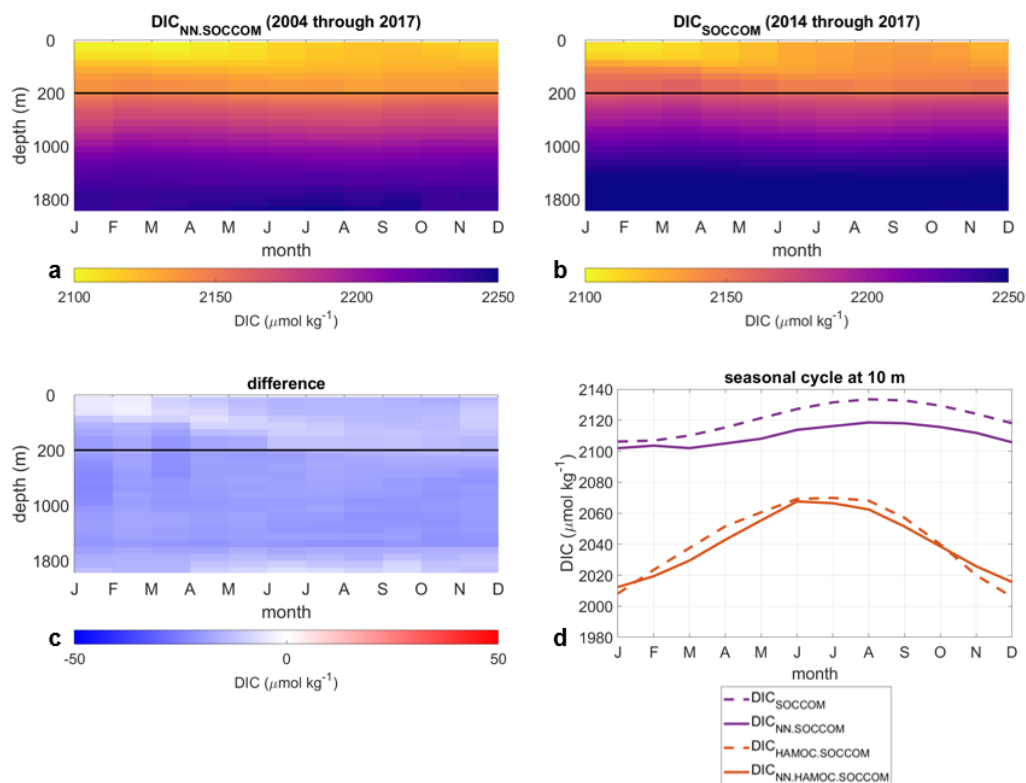


FIGURE B.11: Comparison between the DIC_{SOCCOM} and $DIC_{NN.SOCCOM}$. (a) $DIC_{NN.SOCCOM}$; (b) DIC_{SOCCOM} (c) the difference between the two ($DIC_{NN.SOCCOM} - DIC_{SOCCOM}$). (d) Seasonal cycle at 10 m from DIC_{SOCCOM} (blue), $DIC_{NN.SOCCOM}$ (green), $DIC_{HAMOCC.SOCCOM}$ (orange), $DIC_{NN.HAMOCC.SOCCOM}$ (purple), illustrating the calculated value (filled circles) and the least squares fit (solid lines); a-c are zoomed into the top 200 m.

Despite differences between DIC_{NN} and the various validation datasets, we demonstrate that DIC_{NN} is considerably closer to the independent test data (HOT, BATS, and SOCCOM) than the DIC_{HAMOCC} at those locations (Fig. B.9d, B.10d, and B.11d). Likewise, when trained with the HAMOCC data, $DIC_{NN.HAMOCC}$ lies close to what the synthetic data set prescribes, providing confidence in the global ocean DIC field.

In summary, given the assessments above, we demonstrate that our method can reconstruct the phase of the seasonal cycle at the sea surface well, with a regional mismatch in the amplitude strength of up to $10 \mu\text{mol kg}^{-1}$ (see Supplementary Information Fig. B_SI.4 for a summary of the validation tests).

3.3 Nodal depth and summer NCP

Previous studies have found that the phase of biogeochemical cycles does not simply vary at the surface, but can vary with location and depth due to primary production near the surface and respiration and remineralization below. For example, Najjar and Keeling, 1997 found that the phase of the seasonal cycle of oxygen shifts with depth and named this depth the

“oxygen nodal depth.” Similarly, we also find a change in the phase and amplitude of the seasonal cycle of DIC with increasing depth, as illustrated in Fig. B.12.

To demonstrate this change in DIC with depth, we display the change of the seasonal cycle of DIC as a function of depth at a chosen location in the northern high latitudes (55.5°N , 170.5°E , marked in Fig. B.12b) with strong seasonality illustrated in Fig. B.12a. The surface DIC increases from boreal summer to boreal winter and decreases again from boreal winter to boreal summer. The seasonal draw-down of DIC in this high latitude location is largely linked to transport, mixing, and biology (Sarmiento and Gruber, 2006). As the effects of photosynthesis near the surface and remineralization in deeper water have opposing effects on the DIC, the seasonal cycle of DIC changes in amplitude and phase with increasing depth. At about 100 m, the seasonal cycle flattens, and below that depth, the phase of the seasonal cycle shifts, with the highest values around spring, and the lowest values around autumn. We define this depth, where the phase of the seasonal cycle shifts, as the DIC nodal depth. With further increasing depth, the month of the lowest DIC concentration gradually shifts from autumn towards spring.

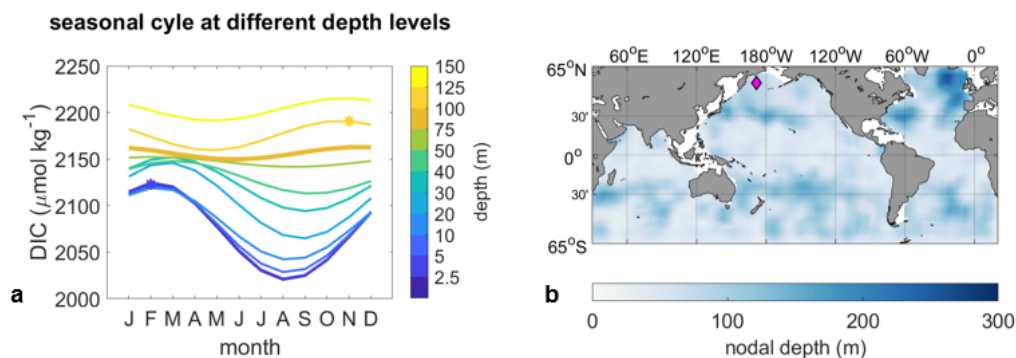


FIGURE B.12: Change in the seasonal cycle with depth. (a) The seasonal cycle of DIC_{NN} as a function of depth (color) at 55.5°N , 170.5°E (marked as a magenta diamond in b). The highest value at 2.5 m (February) and at 100 m (November) are marked with an asterisk, and the DIC at the nodal depth (100 m) is highlighted with a thick line. (b) 2D map of the nodal depth (m) around the globe, smoothed with a scalar function-based filtering using the mean of the neighboring ten grid cells. The nodal depth is here defined as the shallowest depth level; above it, the amplitude decreases, and below it, the amplitude increases again.

Fig. B.12b illustrates strong local variations at depth. The shift in the seasonal cycles usually occurs at depths above ~ 50 m in the tropics, where the seasonal forcing is weak. We find the deepest nodal depths at latitudes poleward of 30° , where the nodal depth is in the range of 150 m with few hot spots where it reaches several hundred meters (Fig. B.12b). The patchiness is a result of the data extrapolation and the sensitivity of the analysis towards uncertainties in the amplitude that can be significant, as illustrated above. Nevertheless, a familiar pattern arises, with deep nodal depths in the temperate southern hemisphere and the deepest nodal depths in the subpolar North Atlantic, corresponding to deep mixed layers (Holte

et al., 2017).

Knowing how deep primary production dominates the uptake of DIC, we can now isolate the biological draw-down of DIC in the upper ocean from the seasonal DIC difference. For this analysis, we removed the equatorial domain from 23°S to 23°N due to the weak seasonality there, resulting in a low signal-to-noise ratio that obscures our analysis. We find that primary production is responsible for a global mean carbon draw-down in summer of $\sim 1.4 \pm 0.2 \text{ mol m}^{-2}$ for our reference period (2004 through 2017) (Fig. B.13). There is a striking correspondence between our product and the global NCP climatology by Lee (2001). When we upscale our mean NCP of $1.4 \pm 0.2 \text{ mol m}^{-2}$, considering the molar weight of carbon of 12.01 g mol^{-1} and an ocean area of 361.1 million km^2 , we find a global NCP of $6.1 \pm 0.9 \text{ PgC}$, which is within the range of the findings by Lee (2001), who estimate the global NCP to be 9.1 ± 2.7 or $10.8 \pm 2.7 \text{ PgC yr}^{-1}$.

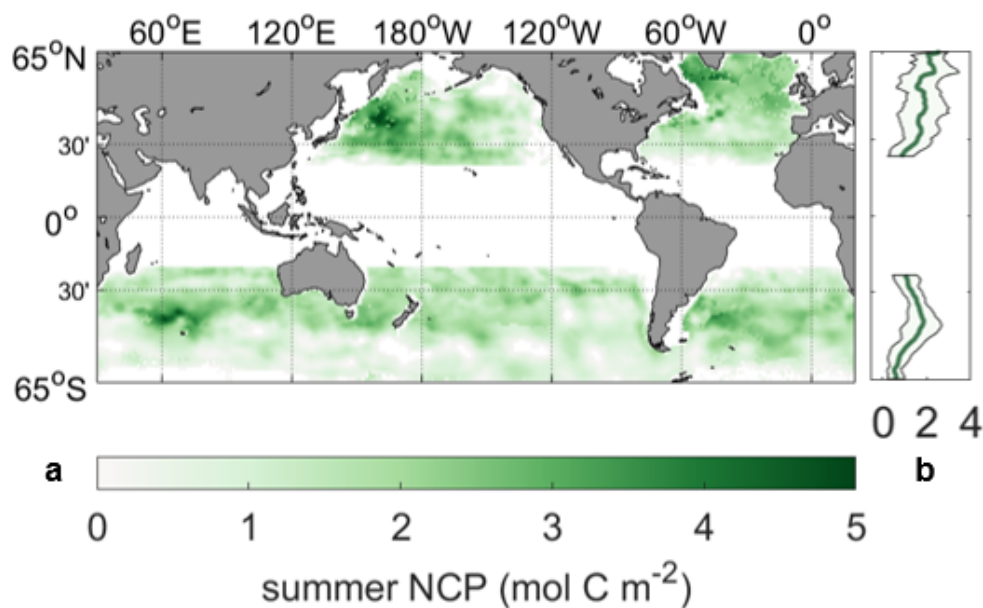


FIGURE B.13: DIC taken up by biology in summer. (a) Spatial distribution of summer net community production between April and October (northern hemisphere) and between October and April (southern hemisphere). (b) Zonal mean summer net community production. The region from 23°N to 23°S is masked due to the weak seasonal cycle here and the related high signal-to-noise ratio.

We find the strongest summer NCP around 45°S in the Southern Hemisphere and in the high latitude North Atlantic (the Labrador Sea) and Northwest Pacific (up to $\sim 5 \pm 1 \text{ mol m}^{-2}$). These three regions are areas of subduction with deeper nodal depths. Studies by Körtzinger et al. (2008) and Quay et al. (2012) have also identified that the NCP in the Labrador Sea and high latitude North Atlantic Ocean as larger than the global mean, and lie close to our estimate with 4 mol m^{-2} and 2.8 mol m^{-2} respectively.

Comparing our estimate of the summer NCP to long-running time-series stations, we find comparable smaller biological uptake. At BATS, Gruber et al. (1998) found a mean annual NCP of $3.8 \text{ mol m}^{-2} \text{ yr}^{-1}$, where we estimate the summer NCP to be $1.2 \pm 0.2 \text{ mol m}^{-2} \text{ yr}^{-1}$. Similarly, the NCP at Ocean Station Papa (OSP; 50°N , 145°W) was estimated using nitrate and oxygen to be $1.5 \pm 0.7 \text{ mol m}^{-2} \text{ yr}^{-1}$ (Plant et al., 2016), which is slightly higher than our estimate of $0.5 \pm 0.1 \text{ mol m}^{-2} \text{ yr}^{-1}$. This difference might reflect the global nature of our approach, which is not always able to fully reconstruct small regional structures.

4 Summary

We created the first global monthly oceanic DIC climatology and subsequent summer NCP estimate based on data from the repeat hydrography synthesis project GLODAPv2.2019 (Olsen et al., 2019). Using a two-step neural network mapping technique, we first clustered the global ocean into regions of similar BGC properties and statistical relationships using SOMs and then ran an FFN in each cluster using various physical and BGC parameters as predictor data. The resulting monthly climatology is on a $1^\circ \times 1^\circ$ grid from 65°N to 65°S on 33 depth levels from 2.5 m to 1975 m and is based on data from 2004 through 2017.

We test our results in various ways, including with synthetic data from the BGC component of the Ocean General Circulation Model HAMOCC, an existing mean annual climatology (Lauvset et al., 2016), and independent time-series station data (HOT and BATS) as well as SOCCOM floats, all of which were not used to create our monthly climatology of DIC. We find that our method performs well in estimating the mean monthly DIC fields. A large part of the discrepancies near the surface stems from differences in the period of the compared products and the anthropogenic perturbation. At the location of the independent observational data, DIC_{NN} is always considerably closer to the measurements than $\text{DIC}_{\text{HAMOCC}}$.

We find the mean DIC concentration globally at the surface to be $\sim 2044 \mu\text{mol kg}^{-1}$, which increases with depth to a global mean of $\sim 2270 \mu\text{mol kg}^{-1}$ at 1975 m. While the top ~ 500 m demonstrate distinct spatial features due to upwelling regions, the deeper waters have a more uniform DIC concentration. The seasonal cycle of DIC has the largest amplitudes at the northern high latitudes (~ 30 to more than $50 \mu\text{mol kg}^{-1}$). The remaining global ocean, including the high southern latitudes, has a median amplitude of $\sim 14 \mu\text{mol kg}^{-1}$. In both hemispheres, the months of the highest DIC tend to be in hemispheric spring, when vertical mixing is usually deepest. In the temperate and subtropical regions, the temperature tends to be the main driver of the seasonal cycle of surface DIC, and nitrate, representing biological production, is an important additional driver in the temperate regions in our method. The nodal depth of DIC, i.e., the depth where the phase of the seasonal cycle of DIC shifts, is less than 50 m in the tropics, and

between 150 and several hundred meters at latitudes poleward of 30°. We estimate the carbon draw-down in the upper ocean induced by primary production in hemispheric summer (i.e., the summer NCP) and find the largest summer NCP in areas of subduction (e.g., around 45°S, and in the northern high latitude Atlantic and West Pacific), in line with previous estimates based on in-situ data. Our estimate suggests a weak but significant increase in summer NCP with increasing latitude in the northern hemisphere. Conversely, the maximum summer NCP can be found around 45°S in the southern hemisphere with the least amount of carbon being taken up by biology in the high latitude Southern Ocean.

Our monthly climatology provides an advancement to previous climatologies that have been either limited by their temporal (Lauvset et al., 2016) or spatial domains (Sasse et al., 2013). It provides the baseline to initialize model set-ups, to study the seasonal cycle of DIC and its future changes linked to ocean acidification and to determine the physical and biogeochemical drivers of the marine carbon cycle. Our DIC-derived summer NCP estimate of $1.4 \pm 0.2 \text{ mol m}^{-2}$ ($\sim 6.1 \pm 0.9 \text{ PgC}$) is in line with previous observation-based assessments and serves as a complementary approach to estimates based on oxygen, which are historically limited in their temporal and spatial domains (Emerson and Bushinsky, 2014; Emerson et al., 2008; Ostle et al., 2015).

Supplementary Information to Appendix B

B_S1 Predictor data

As a neural network reconstructs the available DIC observations based on its relationship to the predictor data, the choice of predictors is essential. Temperature and salinity are known to control the partitioning of DIC into the chemical species forming the DIC pool: carbonic acid, bicarbonate ions, and carbonate ions (Heinze et al., 2015). In addition to the link between temperature and the solubility of CO₂ in seawater, both temperature and salinity also characterize water masses and provide useful additional information about the transport and mixing of DIC (Sarmiento and Gruber, 2006). As part of the biological carbon pump, nutrients and oxygen are also important nominees as predictor data (Heinze et al., 2015), and are available as monthly climatologies from the World Ocean Atlas 2018 (WOA18; (Garcia et al., 2019)). Therefore, we include temperature, salinity, nitrate, silicate, and dissolved oxygen as predictor data. We do not include phosphate or apparent oxygen utilization (AOU), due to the high correlation between nitrate and phosphate, and dissolved oxygen and AOU in most regions. Our results indicate that the network does not gain essential information, while the degrees of freedom substantially increase by including them. Similarly, we do not include information on the time or location as predictor data (for example, latitude, longitude, depth, or month of the year). See B_S4 for a discussion on this.

We use mapped global data on 1°×1° grids from two different platforms as predictor data. First, we use the optimally interpolated temperature and salinity fields from the Argo float-based dataset (Argo, 2019; Roemmich et al., 2015). We compute a monthly climatology from 2004 through 2017 of these temperature and salinity fields by computing the monthly means. As the Argo float-based dataset extends from 2.5 m to 1975 m depth, we use these depth levels as our minimum and maximum depths, respectively. We chose 2004 as the starting year as it marks the year where the Argo program provided global and uniform temperature and salinity data resulting in high confidence in the optimally interpolated dataset by Roemmich and Gilson (2009).

Second, we use the climatological monthly fields, based on data from 1955 through 2017, of dissolved oxygen, silicate, and nitrate from WOA18, which were also mapped using optimal interpolation (Garcia et al., 2019). Here, the dissolved oxygen fields extend until 1500 m, and silicate and nitrate until 500 m. We split the data into three horizontal slabs (2.5–500 m, 600–1500 m, 1600–1975 m) and only use the predictors for the respective depth slabs where they are available. We then interpolate the predictor data onto uniform depth levels and normalize the predictor variables to range between 0 and 1. See Table B_SI.1 for a summary of the predictor data and the respective available depth levels.

TABLE B_SI.1: Input variables for the SOM and FFN for the three different depth slabs (2.5 to 500 m, 600 to 1500 m, 1600 to 1975 m). The depth levels are expressed where 75:25:150 means from 75 m to 150 m in steps of 25 m. For the SOM input variables, clim. DIC refers to the mean annual climatology by Lauvset et al. (2016).

Depth	Depth levels (m)	Number of SOM clusters	SOM input	FFN predictor data
2.5-500 m	2.5:2.5:10 20:10:50 75:25:150 200:50:500 (18 levels)	6	temperature salinity clim. DIC	temperature salinity dissolved oxygen silicate nitrate
600-1500 m	600:100:1500 (10 levels)	4	temperature salinity clim. DIC	temperature salinity dissolved oxygen
1600-2000 m	1600:100:1900 1975 (5 levels)	4	temperature salinity clim. DIC	temperature salinity

B_S2 Target data

As the target data, we use the DIC ship measurements from the GLODAPv2. 2019 data product by Olsen et al. (2019). We only keep data with a WOCE quality control flag of 2 and a secondary GLODAP quality control flag of 1. We linearly interpolate the data onto a regular $1^\circ \times 1^\circ$ grid and onto the same 33 depth levels as the predictor data (Table B_SI.1), retaining only the data from the period and grid points in which the Argo data product overlaps with the GLODAPv2.2019 data (2004 through 2017, 65°N to 65°S). The latter is to avoid inconsistencies between predictor and target data. The final target data set is comprised of DIC measurements from 417 cruises (see Fig. B.1 in the main text).

B_S3 SOM-FFN

Our neural network method consists of two steps. In a first step, we cluster the global ocean into regions of similar properties and statistical relationships using a SOM technique. In the second step, we apply an FFN in each SOM-cluster to establish and apply statistical relationships between global fields of physical and biogeochemical properties and available DIC measurements. We use the monthly climatological fields of temperature and salinity as predictor data for the SOM, in addition to a mapped annual mean climatology of DIC (Lauvset et al., 2016). We weigh the mean climatology of the DIC with a factor of three so that the clusters, to a greater extent, represent regions of similar BGC properties, and to a lesser extent, water masses defined by temperature and salinity. We tested different predictor variables and weights and found that this set-up results in the best representation of the available observations.

SOMs are a type of unsupervised machine learning that is commonly used to cluster data (Kohonen, 1989; Kohonen, 2001, Fig. B_SI.1a-d). In this clustering method, we first arrange each normalized multi-dimensional

input variable (SST, SSS, climatological DIC; Table B_SI.1) as a 1D vector. The arrangement of the 1D vector is less important as long as all multidimensional arrays are arranged in the same way. Next, our network randomly initializes neurons with the same size as the input vectors (so-called neuron weights) and identifies the Euclidean distance of the input vectors to these neurons. Iteratively, during the network training, the neurons are then moved using the batch algorithm (Vesanto et al., 2000) towards clusters of input data with the shortest Euclidean distances. After the training process, all input vectors are assigned the number of the neuron with the shortest Euclidean distance. This results in a 1D vector with the same length as our input variables. We then transfer this vector back to a multidimensional array (latitude, longitude, depth, and month) so that the clusters can be displayed on our multidimensional grid.

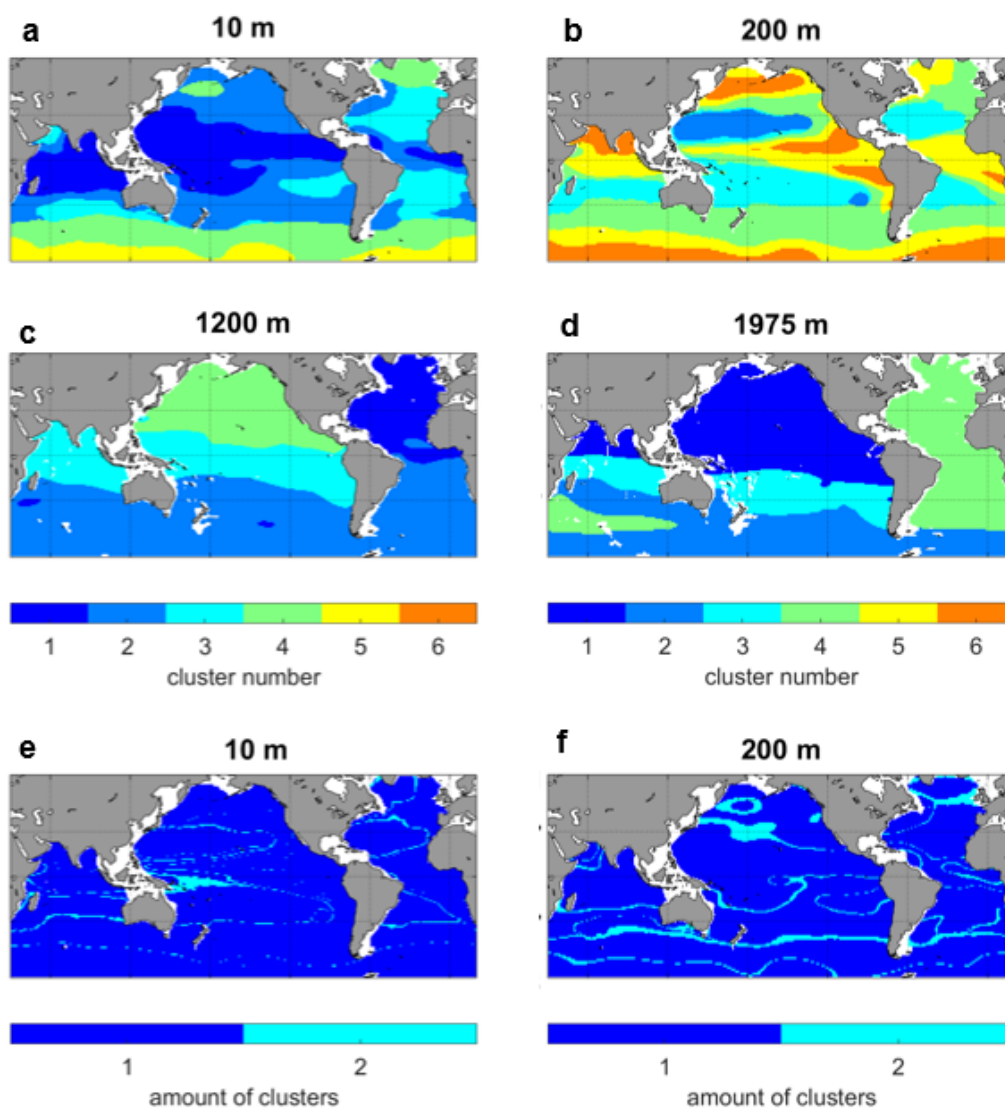


FIGURE B_SI.1: Spatial distribution of the SOM clusters in January for 4 depth levels (a: 10 m, b: 200 m; c: 700 m; d: 1975 m) and the amount of different clusters throughout the monthly climatology at two depth levels (e: 10 m, f: 200 m).

The choice of the number of neurons (and therefore the numbers of clusters) of a SOM is somewhat subjective. Too many clusters will result in only a few observations in each cluster, while too few will create regions that are too large and with a wide range of varying properties. As the surface ocean is less uniform than the intermediate and deep ocean, we chose six clusters for the surface slab (2.5 m–500 m), and four each for the intermediate (600 m–1500 m) and deep slabs (1600 m–1975 m; Table B_SI.1; Fig. B_SI.1a-d). Although the SOMs are computed for each climatological month, the clusters do not considerably change shape from one month to the next. Most clusters remain the same throughout the year, but near the cluster boundary, there is a small amount of variation in the top 200 m (Fig. B_SI.1e-f). The clusters are seasonally relatively static by design due to our weighting of the climatological DIC as a predictor variable.

FFNs are a type of back-propagation network that can approximate nearly any continuous function and are commonly used in Earth System Science (Hornik et al., 1989). In this step, we run an FFN in each cluster separately. During the FFN training, the predictor data that are co-located with the existing DIC measurements are multiplied by randomly initialized weights of each neuron to produce a DIC output (Fig. B_SI.2). This output is then compared to the available observations, and the mean squared error (MSE) is calculated. This step is iteratively repeated using the Levenberg-Marquardt Algorithm that adjusts the neuron weights until the MSE reaches a minimum (Levenberg, 1944; Marquardt, 1963).

The input array consists of the predictor data described above (Table B_SI.1, Fig. B_SI.2). In our set-up, we use two layers, where the first layer (in the literature referred to as the hidden layer) uses 16 neurons, which are connected to a second layer via a sigmoid transfer function. The second layer, consisting of a single neuron, uses a linear transfer function to linearly extract the hidden layer output to produce the final DIC estimate (Fig. B_SI.2). This two-layer setup enables the network to represent both linear and non-linear relationships between predictor and target data (Broullón et al., 2019; Hagan et al., 2014). The number of neurons chosen in the set-up of the FFN is related to the complexity of the data sets (Gardner and Dorling, 1998). While too few neurons result in the network not learning complex relations, too many neurons may overfit the problem (Broullón et al., 2019; Velo et al., 2013). We tested several set-ups and found that 16 neurons lead to the best representation of the observations.

For each iteration in the training process, we use only a randomly chosen subset of the input data to train the network (the training set; here, 80% of the data), and we use the remaining data for internal validation (the validation set; here, 20% of the data). The validation set is used to stop the iterative training once the adjustment of the network weights does not improve the MSE towards the independent validation set. This process is often referred to as an “early stopping approach” and ensures that the network can generalize and prevent the network from overfitting. Note that our mapped estimate is not scaled to a specific year, because it is based on

only 14 years of data (2004 through 2017). As our estimate represents the monthly means of these 14 years, we consider it centered around the years 2010 and 2011.

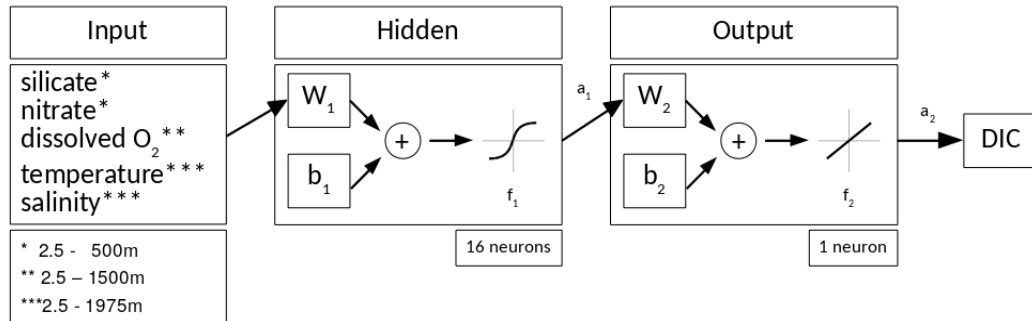


FIGURE B_SI.2: Schematic of our FFN configuration. Input vectors: silicate and nitrate until 500 m, dissolved oxygen until 1500 m, temperature and salinity until 1975 m; W : weight matrices; b : bias matrices; $+$: sum; f : transfer function; a : output matrices; subscripts indicate the number of the layer; boxes below the hidden layers indicate the number of neurons used. Modified from Hagan et al. (2014).

B_S4 Discussion on including information on the time or location as predictor in FFNs

Some studies include a time-variable, such as the month of the year as a predictor in FFNs (Bittig et al., 2018; Sauzède et al., 2017; Zeng et al., 2014). To represent the periodicity of the year, the cosine and/or sine of the time-variable is usually used (see Eq. B_S.1 and B_S.2 for the computation of the cosine and sine of the month of the year respectively). The same procedure is commonly used to represent the periodicity of longitude (Broullón et al., 2019; Zeng et al., 2014).

$$\cos_{month} = \cos \frac{\pi}{n/2} month \quad (\text{B_SI.1})$$

$$\sin_{month} = \sin \frac{\pi}{n/2} month \quad (\text{B_SI.2})$$

where n is the number of months there are in a year (12).

However, a problem arises: both the cosine and sine curve cross the x -axis twice in one cycle (Fig. B_SI.3). Hence, months that are climatologically different, are assigned the same value. For example, in the cosine curve, the 3rd and 9th month have the same value (0). Hence, in this case, March would learn from October and vice versa, although they have different values in the real world. Similarly, in the sine curve, the 6th and the 12th month have the same value (0) and so June and December would learn from each other, which is not in line with our knowledge of the seasonal cycle of carbon.

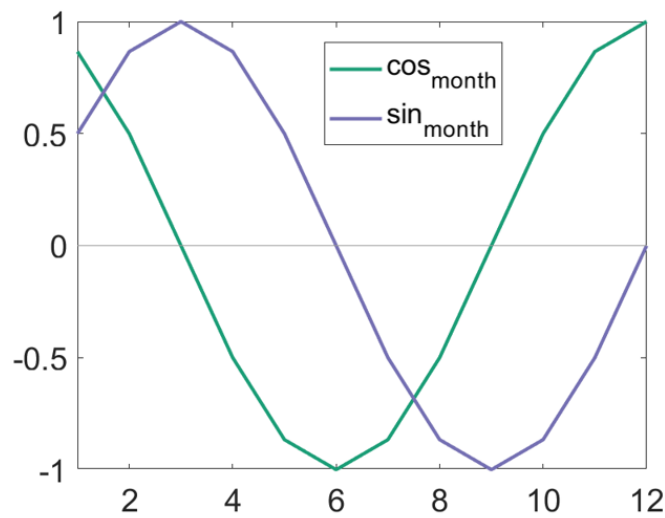


FIGURE B_SI.3: The curves of the cosine and sine of the month of the year.

During the set-up of our FFN, we analyzed what would happen if we did include the cosine and/or sine of the month of the year as a predictor. Our results were considerably noisier in those set-ups and we could not reproduce the seasonal cycles. Presumably, the same problem would arise when using the cosine and/or sine of the day of the year as a predictor. Instead, the network obtains the seasonal information from the predictor (especially temperature and salinity) and can produce a seasonal cycle of DIC without being provided information about the time. Similarly, we expect the same problem to occur when using the cosine and/or sine of longitude. Our method overcomes this problem through the clustering with the SOMs before the FFN is run and so does not need explicit information on the location.

B_S5 Summary of validation tests

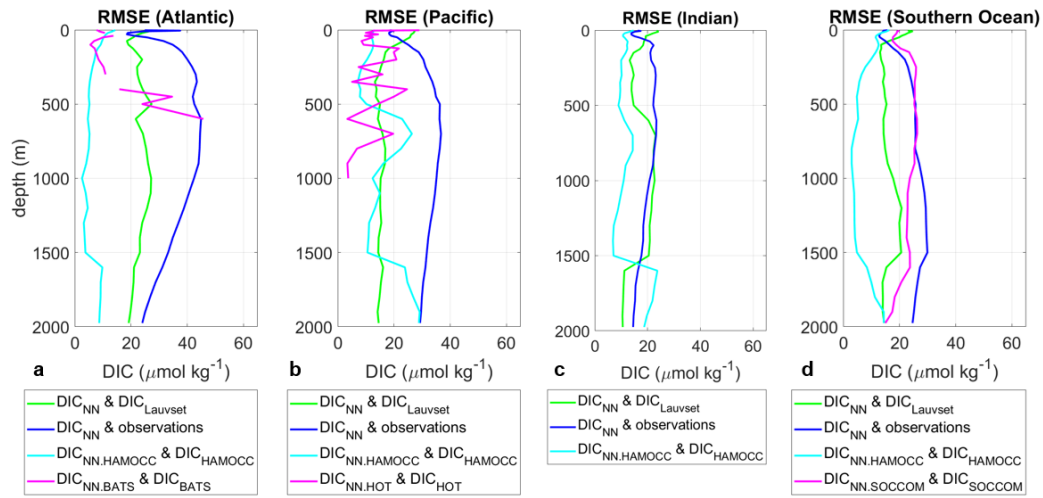


FIGURE B_SI.4: RMSE as a function of depth for the Atlantic (a), Pacific (b), Indian (c), and Southern (d) Ocean. Illustrating the difference between DIC_{NN} and $\text{DIC}_{\text{LAUVSET}}$ (green). The residuals of DIC_{NN} from the observations (dark blue), and the difference between the $\text{DIC}_{\text{NN.HAMOCC}}$ and $\text{DIC}_{\text{HAMOCC}}$ (light blue). The basins with independent observational data also demonstrate the difference between that (i.e. DIC_{BATS} (a), DIC_{HOT} (b), and $\text{DIC}_{\text{SOCCOM}}$ (c)) and DIC_{NN} (magenta).

C Temporary Reduction in Southern Ocean sub-surface Dissolved Inorganic Carbon

Keppler, Lydia^{1,2} & Peter Landschützer¹

¹ Max-Planck-Institute for Meteorology (MPI-M), Hamburg, Germany.

² International Max Planck Research School on Earth System Modelling (IMPRS-ESM), Hamburg, Germany.

Paper status at the time of the submission of this thesis:

In preparation, to be submitted to Geophysical Research Letters

Data availability:

The data product created during this study is freely available to the public (will be submitted to NCEI OCADS after publication of this paper).

Supplementary Information accompanies this paper at the end of this Appendix.

Contributions: L.K. and P.L. designed the research; L.K. performed the research; L.K. wrote the draft manuscript; P.L. contributed to the discussion of the results and the manuscript at all stages.

Abstract

The Southern Ocean carbon sink is highly variable. However, it is unclear how this variability is reflected in the dissolved inorganic carbon (DIC) pool, and the drivers behind this variability are still debated. Here, we repeat hydrography measurements of DIC from the GLODAPv2.2019 database in combination with a 2-step mapping approach to obtain monthly global fields of interior DIC from 2004 through 2017 to investigate the interannual signal until 500 m depth in the Southern Ocean south of 35°S. At the sea surface, the strongest signal is the anthropogenically-forced DIC trend with little variations resulting from reduced sub-surface DIC transport. Below the surface, we discover a more pronounced DIC reduction up to $\sim 20 \mu\text{mol kg}^{-1}$ from 2004 through 2009, followed by a strong recovery until 2012. This reduction is most prominent south of the Polar Front and extends to 500 m. These sub-surface variations are largely in line with proposed variations in the meridional overturning circulation during this period.

1 Introduction

Approximately half of the oceanic uptake of anthropogenic carbon dioxide from the atmosphere occurs in the Southern Ocean south of 35°S, although this region covers approximately 1/3 of the global oceans (Landschützer et al., 2015). Different, often opposing processes are at play here, affecting the carbon flux, and the transport and storage of carbon at depth. Close to the Antarctic coast, sea-water is cooled, which allows for oceanic carbon uptake due to enhanced solubility, and the down-welling of these carbon-enriched surface waters stores it at depth. Near the Antarctic Circumpolar Current (ACC), northward Ekman transport induces upwelling of carbon-rich waters and thereby outgassing of carbon. North of the ACC, Subantarctic Mode Waters that are transported northwards cool the warmer subtropical waters, leading to oceanic uptake of carbon, which is then subducted and transported northward. However, these processes display a large degree of variability on time scales from interannual to decadal (DeVries et al., 2017; Downes et al., 2009; Freeman et al., 2016; Hall and Visbeck, 2002; Schlosser et al., 2018).

The Southern Ocean carbon uptake at the air-sea interface was found to have weakened in the 1990s, despite the continued increase in atmospheric CO₂ (Le Quéré et al., 2007). This finding led to concern that the Southern Ocean carbon sink could have saturated. However, nearly a decade later, Landschützer et al. (2015) found that this globally important carbon sink had regained its strength between 2002 and 2011 and was back at the strength as would be expected due to the increase in atmospheric CO₂. Recently, the trend has reversed again, and from 2012 through 2016 the Southern Ocean carbon sink weakened again (Keppler and Landschützer, 2019).

The mechanisms explaining these decadal changes in the Southern Ocean carbon sink are not yet fully resolved and relate to circulation and biology. (Gruber et al., 2019a; Keppler and Landschützer, 2019; Landschützer et al., 2015) proposed that these changes are linked to regional variability in the local weather pattern, causing different hot spots of air-sea CO₂ exchange. DeVries et al. (2017) linked a weakening of the Meridional Overturning Circulation (MOC) in the 2000s to a strengthening of the Southern Ocean carbon uptake due to less upward transport and outgassing of natural carbon stored at depth. Similarly, Panassa et al. (2018) proposed links between the Southern Ocean carbon uptake variability and changes in the summer mixed layer depth in that region, as a deeper mixed layer enhances vertical mixing and thus, biological uptake of carbon. In line with that finding, Gregor et al. (2018) found that the biological draw-down of carbon is the main driver of the seasonal variability in the Southern Ocean carbon flux. As changes in the MOC and the biological uptake of carbon are reflected in the dissolved inorganic carbon (DIC) pool, we choose to investigate the recent development of the interior DIC in the Southern Ocean.

Most of the oceanic carbon that is taken up from the atmosphere is stored at depth as DIC, while a smaller amount is drawn down through photosynthesizing organisms consuming carbon (Heinze et al., 2015; Keppler et al., in review). Previous studies on the changes in the stored DIC only focused on the anthropogenic part and did so at decadal time-scales (Gruber et al., 2019b; Khatiwala et al., 2009; Sabine et al., 2004) as their focus was the anthropogenic increase rather than interannual to decadal variations of the DIC pool. Specifically, Gruber et al. (2019b) found that half of the global anthropogenic DIC occupies the upper 400 m, and the Southern Ocean has the second-deepest vertical extent of anthropogenic carbon in the world, only exceeded in the Deep Water Formation region of the North Atlantic. As the interannual to decadal variability of the carbon uptake at the surface is quite substantial (Keppler and Landschützer, 2019; Landschützer et al., 2015; Le Quéré et al., 2007), one would expect to see some of this variability in the interior DIC. The temporal-mean distribution of DIC in the water column, as well as the seasonal cycle of DIC, has been estimated by previous global-scale studies (Keppler et al., in review; Lauvset et al., 2016). However, the interannual to decadal variations in the interior Southern Ocean contemporary DIC (natural + anthropogenic) is yet to be investigated.

The processes of upwelling and subduction, and the associated carbon fluxes and storage, are not zonally uniform and many processes in the Southern Ocean occur in 'hot spots' (Rintoul, 2018; Sallée et al., 2012). To investigate the variability in the DIC pool at a regional scale, a mapped data estimate of DIC in the Southern Ocean, based on available but sparse shipboard measurements, is necessary. Recent progress in the collection and synthesis of available observations through the Global Ocean Data Analysis Project for Carbon (GLODAP, Key et al. (2015) and Olsen et al. (2019)) has led to the compilation of ship-measurements of oceanic carbon in the

interior ocean from the surface until over 7000 m depth. The data consists of over 1.1 million direct measurements from bottled sea-water samples across the world since the 1970s. However, despite an increase in ship measurements through the repeat hydrography surveys (Talley et al., 2016), DIC measurements in the Southern Ocean remain sparse.

Here, we combine data from GLODAPv2.2019 with a two-step neural-network-based mapping technique to reconstruct mapped monthly interior DIC fields from 2004 through 2017 for the global ocean. Using our new data estimate, we present the variability of DIC in the top 500 m of the Southern Ocean and link the observed variability both to processes that drive this variability and to processes that are driven by it.

2 Data and Methods

This section briefly discusses the novel set-up of our method and the data used. A more detailed discussion on the method can be found in Keppler et al. (in review). In the first step, we cluster the global ocean into regions that have similar biogeochemical properties using self-organizing maps (SOMs), and in a second step, we run a Feed-Forward-Network (FFN) in each of the clusters. The FFN first approximates the statistical relationship between predictor data and target data within each SOM-cluster and then applies this relationship to infer the oceanic DIC concentration. We use monthly gridded DIC fields from 2004 through 2017 from GLODAPv2.2019 (Key et al., 2015; Olsen et al., 2019) as target data. Following Keppler et al. (in review), temperature, salinity, dissolved oxygen, silicate, and nitrate are all useful predictors of the seasonal cycle of DIC as these predictors not only drive the partitioning of DIC through the physical and biological carbon pump but also are statistically tied to DIC by defining different water masses; hence, we use the same predictors for our updated set-up.

Compared to the monthly climatology by Keppler et al. (in review), we extend our data product to a monthly temporal resolution from 2004 through 2017 and chose a vertical extent of 500 m. Below this depth, fewer observations exist, and we expect little variability in the DIC pool on interannual to decadal timescales (Gruber et al., 2019b). In the SOM-step, we use six clusters, following Keppler et al. (in review). In the FFN-step, we use the objectively interpolated interannual fields of temperature and salinity based on Argo float measurements (Argo, 2019; Roemmich and Gilson, 2009) as predictors. This data product is on a $1^\circ \times 1^\circ$ grid and reaches from 65°N to 65°S , and from 2.5 m to 1975 m. In addition, we use the objectively interpolated monthly climatologies of dissolved oxygen, silicate, and nitrate from the World Ocean Atlas 2018 (Garcia et al., 2019). Although these variables are only available at seasonal resolution, these predictors aid in the reconstruction of the distribution of interior DIC. To reconstruct the expected trend from the increase in atmospheric CO_2 , we further use the monthly fields of the oceanic surface pCO_2 (Landschützer et al., 2014) and the globally averaged annual mean concentration of atmospheric CO_2 at the

marine surface from the Earth System Research Laboratory (https://www.esrl.noaa.gov/gmd/ccgg/trends/gl_data.html).

To avoid over-fitting the sparse observations, we apply a bootstrapping approach following Keppler et al. (in review): We run the SOM-FFN method ten times, holding back different sets of 20% of the observations each time to test the reconstruction independently, and then take the mean over this ensemble as our best guess reconstruction. The standard deviation across the ensemble represents the generalization uncertainty. We then further smooth the DIC fields with a scalar function-based filter, which averages over the neighboring three grid cells in each direction except depth (latitude, longitude, and month). For our calculations of the interannual signal, we remove the seasonal cycle of our DIC estimate by applying a 12-month moving average filter and subsequently remove the first and last six months in the time-series. Hereafter, we refer to our mapped DIC estimate as DIC_{NN} .

For our analysis, we distinguish sub-regions within the Southern Ocean based on two of the fronts defined by Orsi et al. (1995). We use the Subtropical Front ($\sim 40^\circ\text{S}$) and the Polar Front ($\sim 55^\circ\text{S}$) as our regional boundaries (see Supplementary Information (Fig. C_SI.1) for the location of the fronts). Here, we refer to the region between 35°S and the Subtropical Front as the Subtropical Zone; the region between the Subtropical Front and the Polar Front as the Inter-Frontal Zone; and the region between the Polar Front and the southern boundary of our data product at 65°S as the Polar Zone.

We test our method with independent observations collected in the Southern Ocean, i.e., data was not used to train the FFN. We use the calculated DIC from Argo floats with biogeochemical sensors that are collecting data as part of the Southern Ocean Carbon and Climate Observations and Modeling project (SOCCOM, <https://socom.princeton.edu/>). The SOCCOM floats are well scattered in time and space but only extend from 2014 through 2017 (hereafter DIC_{SOCCOM}). We sub-sample our DIC_{NN} when and where SOCCOM floats collected data (hereafter $DIC_{NN.SOCCOM}$) and compare it to DIC_{SOCCOM} .

Due to the lack of independent data before 2014, we further test our method with synthetic data, following the approach of Keppler et al. (in review). Here, we take the full DIC model field from the ocean biogeochemistry model HAMOCC (Ilyina et al., 2013; Mauritsen et al., 2019) as illustrated in (Le Quéré et al., 2018). For consistency, we interpolate the output onto the same grid ($1^\circ \times 1^\circ$, on 18 depth levels between the surface and 500 m, from 2004 through 2017) and sub-sample the model field of DIC when and where we have DIC measurements in GLODAPv2.2019. This data set is hereafter called DIC_{HAMOCC} . We then run our SOM-FFN method using predictor data from HAMOCC to reconstruct the full model field (hereafter $DIC_{NN.HAMOCC}$). We then compare DIC_{HAMOCC} with $DIC_{NN.HAMOCC}$ as an initial test of our method.

3 Results

We find that the strongest signal in the Southern Ocean surface DIC is a positive trend (Fig. C.1). From 2004 through 2017, the surface DIC nearly steadily increases, on average, at a rate of $\sim 1.3 \mu\text{mol kg}^{-1} \text{ yr}^{-1}$. This approximately agrees with the anthropogenically-forced increase in DIC in the upper 100 m, which Gruber et al. (2019b) estimated to be $1.1 \mu\text{mol kg}^{-1} \text{ yr}^{-1}$ between 1994 and 2007. However, the significant variability seen in the Southern Ocean surface pCO_2 and hence in the air-sea CO_2 flux appears only weakly reflected in the Southern Ocean surface DIC pool (Fig. C.1) as it is almost entirely masked by the longer-term trend. Below the surface, however, we find substantially larger variability superimposed onto the anthropogenically-forced trend. Here, the DIC concentration has a negative trend from 2004 onward, peaking around the year 2009, after which the DIC concentration bounces back to levels higher than before the reduction. This signal is visible from approximately 50 m onward and increases in intensity with depth, extending until 500 m. This temporary reduction in DIC is weakest in the Subtropical Zone, where the reduction from 2004 to 2009 equates to $\sim 10 \mu\text{mol kg}^{-1}$ (Fig. C.1b) and it is strongest in the Polar Zone, where the reduction is by $\sim 30 \mu\text{mol kg}^{-1}$ (Fig. C.1d).

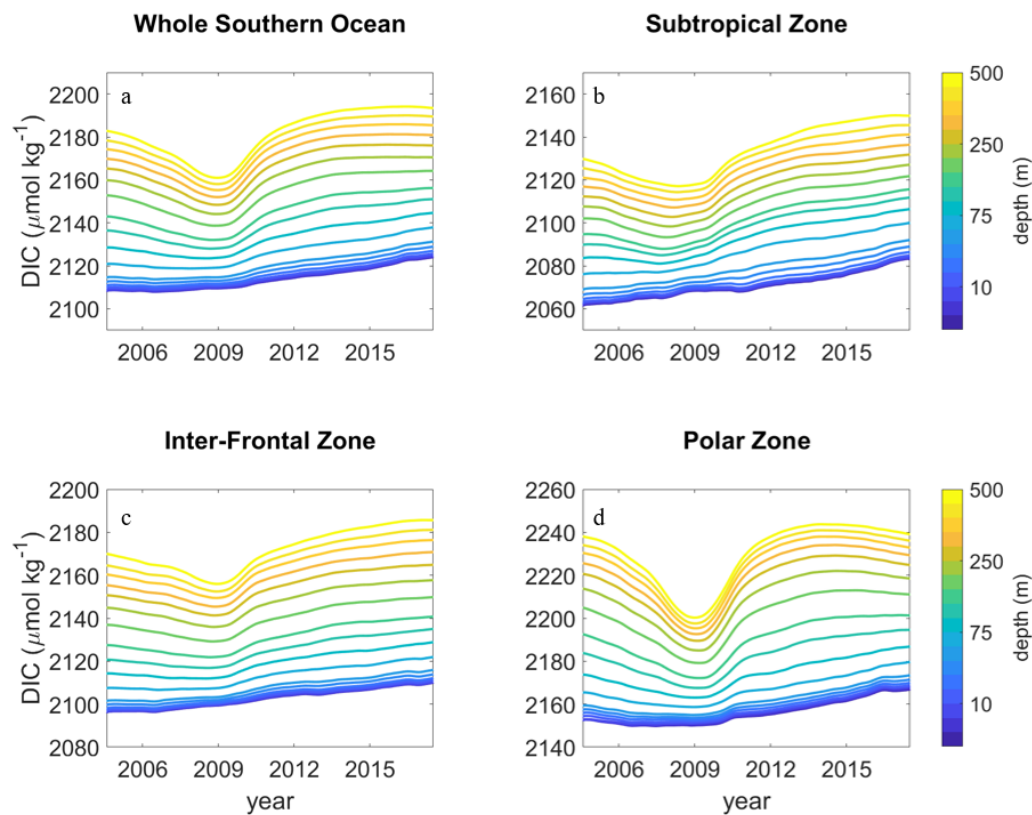


FIGURE C.1: The changing DIC concentration with time (x-axis) and depth (color) for the whole Southern Ocean (a), the Subtropical Zone (b), the Inter-Frontal Zone (c), and the Polar Zone (d). See (Fig. C_SI.1) for the location of the fronts. Note that the mean values of the y-axes differ among a-d, but they have the same scale (maximum value - minimum value = $120 \mu\text{mol kg}^{-1}$).

This temporary sub-surface reduction in DIC around the year 2009 cannot simply be explained with the surface flux variability. Keppler and Landschützer (2019) found that the reinvigoration period of the early 2000s, during which the Southern Ocean took up increased amounts of carbon, ended around 2011 with a weakening of the sink after that. As the DIC pool weakens before the surface uptake does, the temporary sub-surface reduction in DIC cannot directly be driven by the changes in the surface fluxes but may precede the surface flux. Therefore, we turn to the GLODAPv2.2019 data that was used to train the network, testing whether such a decrease can directly be observed in the DIC measurements. We do indeed find comparably low sub-surface DIC concentrations measured around the year 2009 (Fig. C.2), nevertheless, we cannot exclude the possibility that our method amplifies these DIC measurements by extrapolating them into their vicinity, resulting in an over-estimated DIC reduction. Therefore, we turn to available independent measurements and synthetic data to test whether our method is sensitive to the sampling.

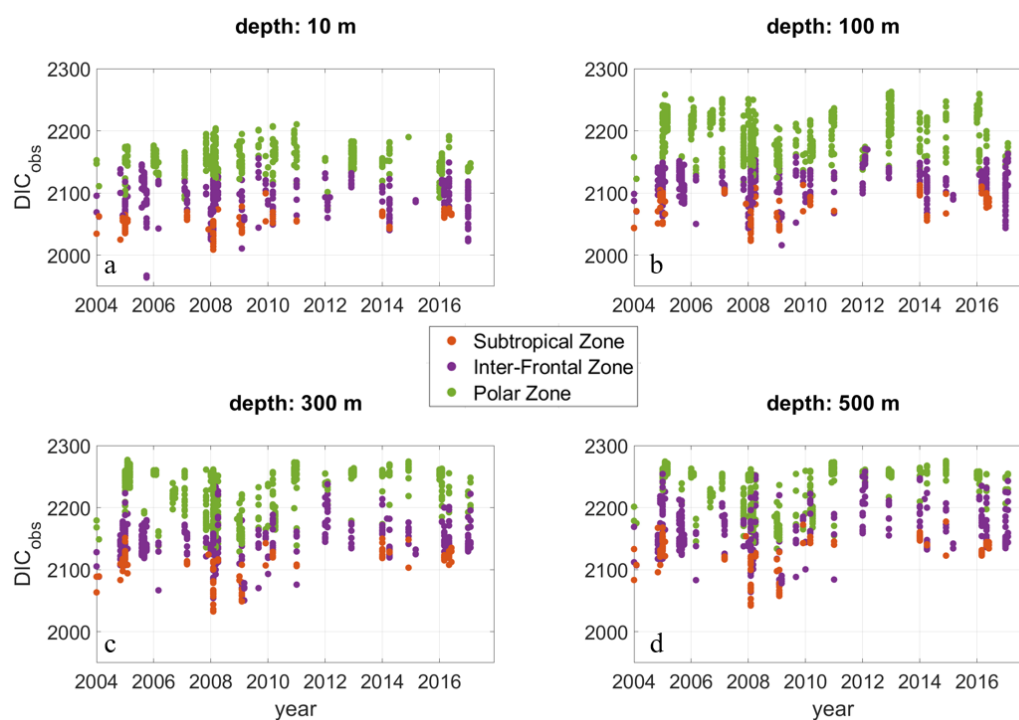


FIGURE C.2: The binned GLODAPv2.2019 DIC concentration on 4 depth levels: 10 m (a), 100 m (b), 300 m (c), and 500 m (d), indication the sub-region within the Southern Ocean in color: the Subtropical Zone (orange), Inter-Frontal Zone (purple), and the Polar Zone (green). See (Fig. C_SI.1) for the location of the fronts.

We test whether our method can reconstruct the calculated DIC from SOCCOM floats, which was not used to train the network, and therefore provide an independent dataset. While the SOCCOM floats started profiling in 2014, they cannot resolve the 2009 reduction, however, they provide a benchmark test, whether our method is capable of reconstructing the observed DIC concentration and variability in the later years of our study. From 2014 onward, the trend and interannual variability in $DIC_{NN.SOCCOM}$ compares remarkably well to DIC_{SOCCOM} (Fig. C.3a-d), given the independent nature of these measurements. There is, however, an offset in the mean concentration of approximately $10 \mu\text{mol kg}^{-1}$, with $DIC_{NN.SOCCOM}$ being generally lower than DIC_{SOCCOM} . This offset may, in part, also be explained by the fact that DIC is not directly measured by the floats and is calculated from directly observed quantities. The root mean squared error (RMSE) between $DIC_{NN.SOCCOM}$ and DIC_{SOCCOM} equates to $24 \mu\text{mol kg}^{-1}$ largely owing to the mean offset. Nevertheless, given the independent nature of the float data and the fact that we compare calculated DIC from floats to an extrapolation of sparse ship data, we find an encouraging agreement between them.

To test whether the signal results from data sparsity and a large signal-to-noise ratio in the measurements, we use synthetic data from a hindcast simulation of the ocean biogeochemistry model HAMOCC, forced with real climate (DIC_{HAMOCC}). We subsample DIC_{HAMOCC} at the time and location of the GLODAPv2.2019 ship tracks and then reconstruct the model field using our 2-step neural network method and predictor data from the HAMOCC model ($DIC_{NN.HAMOCC}$). Both the mean DIC concentration and the interannual variability of $DIC_{NN.HAMOCC}$ in the Southern Ocean compares well with DIC_{HAMOCC} (Fig. C.3e). Unlike the real-world reconstruction, the model field does not display significantly stronger variability at depth compared to the surface. Overall, besides a few small discrepancies, the RMSE between $DIC_{NN.HAMOCC}$ and DIC_{HAMOCC} is only $8 \mu\text{mol kg}^{-1}$, increasing the confidence in our reconstruction. This RMSE is considerably smaller compared to the SOCCOM comparison, which can be explained by the larger amount of noise in measurements compared to the smoother model field.

We can further use the HAMOCC model output to test whether the mean offset from the SOCCOM float comparison (Fig. C.3a-d) is an artifact of the shipboard sampling. Therefore, as an additional test, we sub-sample DIC_{HAMOCC} at the time and location of SOCCOM float measurements (hereafter $DIC_{HAMOCC.SOCCOM}$). The SOM-FFN reconstruction $DIC_{NN.SOCCOM}$ lies considerably closer to DIC_{SOCCOM} than $DIC_{HAMOCC.SOCCOM}$. However, $DIC_{NN.HAMOCC.SOCCOM}$ reconstructs $DIC_{HAMOCC.SOCCOM}$ very well with a small RMSE of $9 \mu\text{mol kg}^{-1}$ (Fig. C.3a-d) that is in the range of the overall RMSE from the full model reconstruction above.

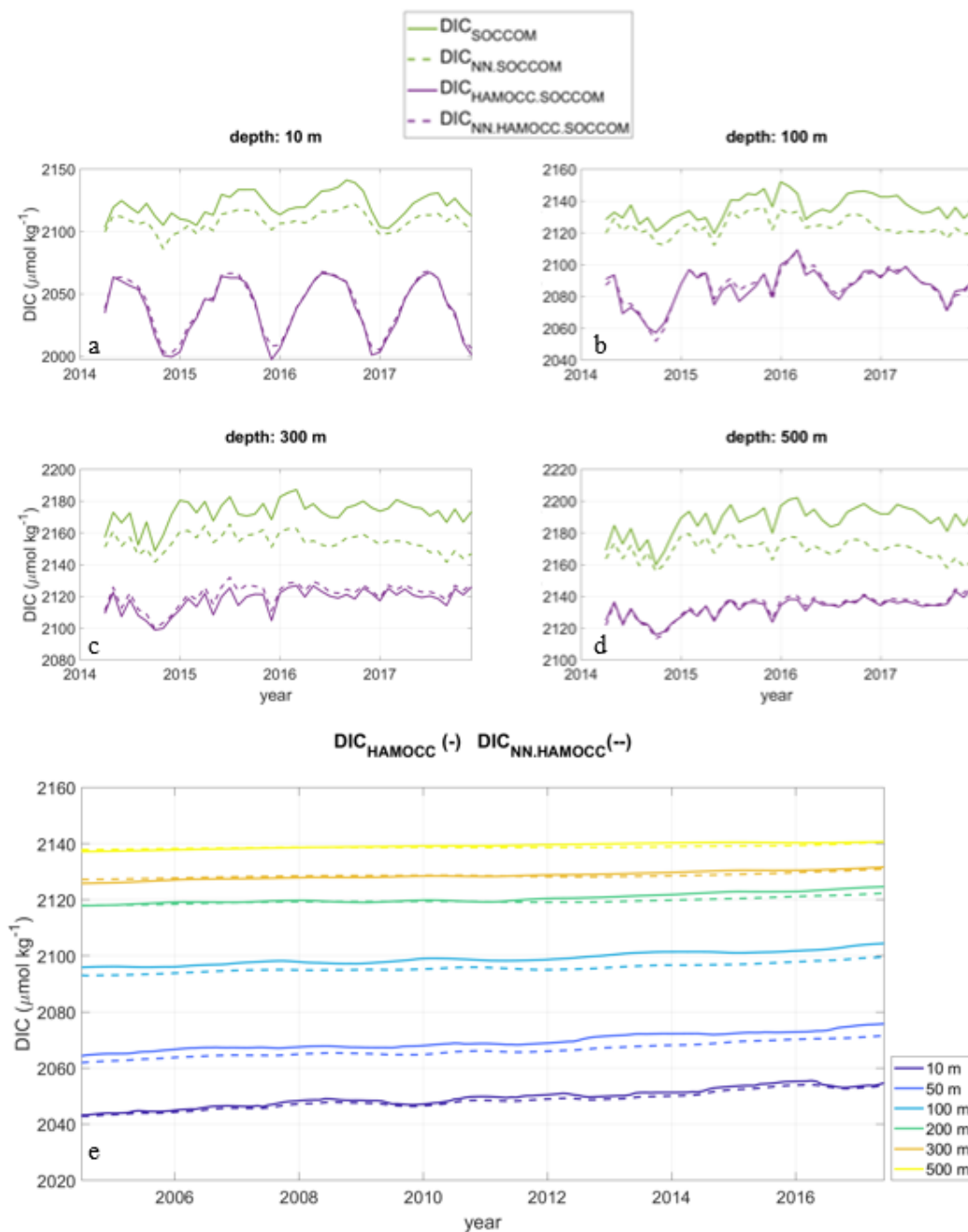


FIGURE C.3: (a-d) Timeline of the DIC that was calculated from SOCCOM float measurements (solid green line), and our SOM-FFN estimate of DIC at the same time and location (dashed green line) and the timeline of the DIC in HAMOCC at the time and location of SOCCOM float observations (solid purple line), and our SOM-FFN estimate thereof (dashed purple line), at different depth levels: 10 m (a), 100 m (b), 300 m (c), and 500 m (d). (e) Timeline of the DIC in HAMOCC (solid lines), and our reconstruction thereof (dashed lines) in the Southern Ocean at different depth levels (color).

Overall, we find that when and where we can test our method with independent data, it performs well. We further find evidence that the current shipboard sampling is sufficient to reconstruct available independent constraints faithfully; hence, we have confidence that the temporary sub-surface reduction in our estimate of the Southern Ocean DIC concentration is a robust feature.

To determine what forced the temporal sub-surface reduction in DIC, we investigate its potential drivers. As biological measurements, such as nutrients and oxygen, do not yet exist at full basin-scale multi-year resolution from the surface to the interior Southern Ocean, we are left investigating the link between DIC and its chemical and physical drivers of which we have sufficient data, i.e., the ocean surface $p\text{CO}_2$, and surface as well as interior temperature and salinity. Here, we assume that atmospheric CO_2 contributes to the long term DIC trend but has little influence on the year-to-year variability. As we are primarily interested in the drivers behind the interannual signal, and not the long-term trend, we remove the linear trends in our DIC and driver fields for comparison of the remaining anomalies.

Despite the difference in timing between the variability of the air-sea CO_2 flux compared to the interior DIC in the Southern Ocean, we do see a strong regional correlation between DIC and the oceanic surface $p\text{CO}_2$ linked to the solubility pump (Fig. C.4a,d). As we would expect, this strong correlation vanishes with depth (Fig. C.4a-c). Near the surface, the correlation coefficient between DIC and the surface $p\text{CO}_2$ is strongly positive throughout the Southern Ocean. This may be expected as more oceanic uptake of carbon and its dissolution enhances the formation of DIC. Similarly, additional DIC brought up from deep waters through upwelling that warms at the surface enhances the surface $p\text{CO}_2$. The strongest correlations at depth remain near the Antarctic Circumpolar Current, where the mixed layer is deepest, enhancing vertical mixing (Holte et al., 2017; Panassa et al., 2018) and so the link between the sub-surface DIC and the surface $p\text{CO}_2$ is evident deeper than in other regions.

Conversely, the temperature near the surface is strongly negatively correlated with DIC (Fig. C.4d). We expect this negative correlation due to the solubility CO_2 , as carbon dissolves faster in colder water than in warmer water. At latitudes lower than 40°S , where the correlation between the surface $p\text{CO}_2$ and DIC is negative, temperature dominates the $p\text{CO}_2$ anomalies over DIC, in agreement with the findings from Takahashi et al. (2002). At the same time, the correlation between temperature and DIC becomes less negative with depth and more regions of positive correlations emerge around 100 m (Fig. C.4e). South of 40°S , the areas of negative correlations are mostly areas of upwelling, where cold, carbon-rich water is brought up to the surface. Conversely, the zonal band of positive correlations between DIC and temperature around the Subtropical Front is an area of mean carbon uptake (Landschützer et al., 2015; Talley et al., 2011). Here, Subantarctic Mode Water, characterized as being saltier and, due to the contact with the atmosphere, also warmer and richer in anthropogenic carbon than the water below, are subducted, in line with the pattern in (Fig. C.4h) (Talley et al., 2011). At 500 m, the pattern looks similar compared to the pattern at 100 m, but weaker and slightly shifted northward. Overall, near the surface, the DIC variability is tightly linked to the variability in the air-sea CO_2 flux and solubility, while below the surface, the DIC correlations pattern correspond to the larger-scale circulation pattern.

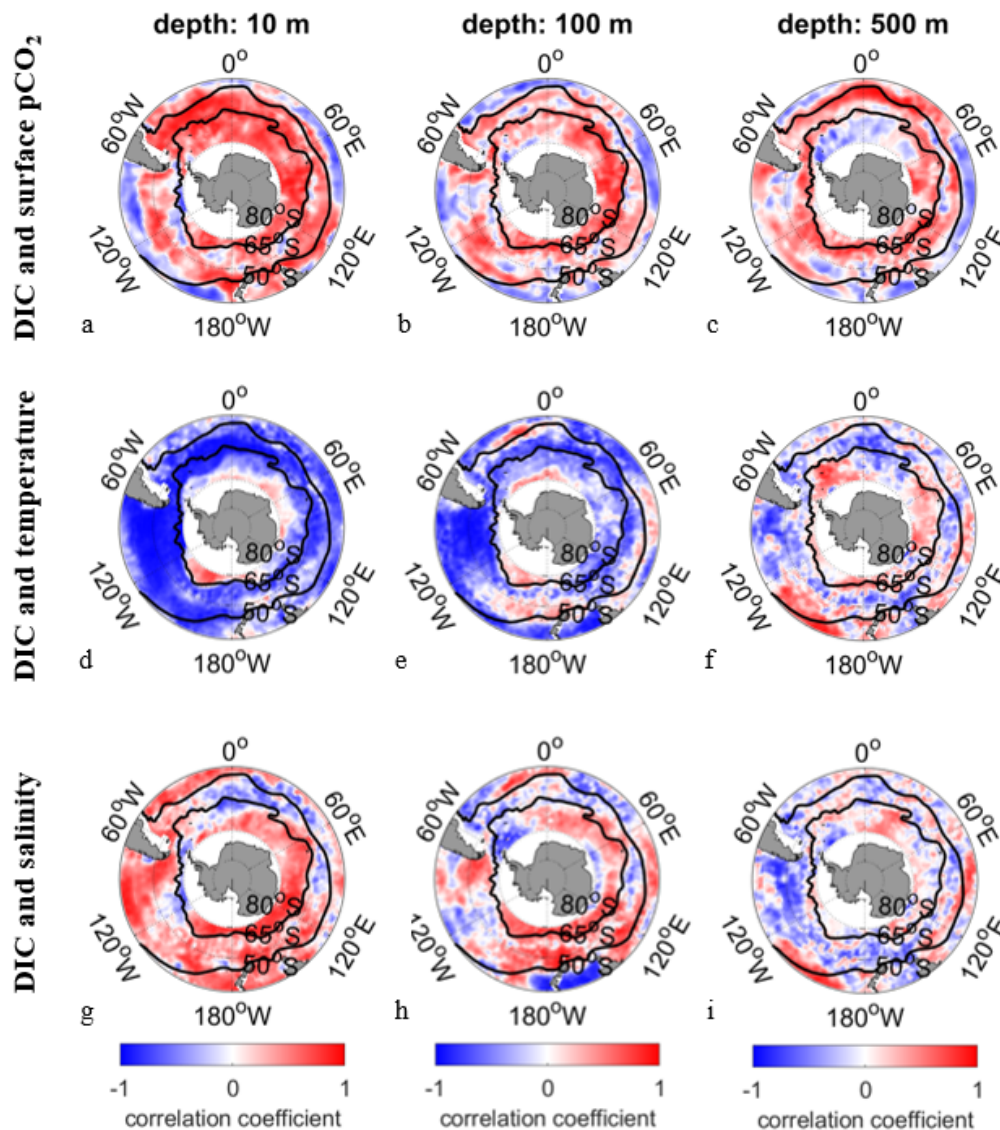


FIGURE C.4: Spatial distribution of the correlation coefficient between DIC and sea surface pCO₂ (a-c), between DIC and temperature (d-f), and between DIC and salinity (g-i) at each 1°x1° grid point on different depth levels: 10 m (a,d,g), 100 m (b,e,h), and 500 m (c,f,i).

4 Discussion

We have created the first interannual mapped monthly fields of interior DIC in the Southern Ocean from the surface until 500 m, for the years 2004 through 2017, based on a 2-step neural network technique and measurements from the GLODAPv2.2019 database (Key et al., 2015; Olsen et al., 2019). We demonstrate, based on the reconstruction of synthetic data from a biogeochemistry model and tests with independent measurements, that the method is capable of reproducing the observed variability despite the sparsity of ship measurements.

Our results reveal that variations, as seen in the surface uptake of carbon (Keppler et al., in review; Landschützer et al., 2015; Le Quéré et al., 2007), are visible in the water column, albeit near the surface, these variations are small in comparison to the trend driven by the increase in anthropogenic CO₂. We further find a substantial decadal signal in the DIC below the surface, with a minimum in 2009, followed by a quick recovery after that. This signal extends to at least 500 m and is also seen in the direct GLODAPv2.2019 observations. This signal is strongest in the Polar Zone, i.e., near the Antarctic coast, which is an area of upwelling and outgassing.

The observed sub-surface variability and the driver correlations line up with recent findings by DeVries et al. (2017), i.e. that the observed variations in the global carbon flux are related to changes in the MOC. The authors used a global inverse model to quantify the MOC and found that a strengthened MOC in the 1990s enhanced the outgassing of carbon, while in the 2000s, a weaker MOC led to less outgassing of natural carbon and thus, larger net oceanic uptake of carbon. Although that study does not extend to the 2010s, it supports our finding until 2009. The weaker MOC leads to less sub-surface DIC as suppressed overturning results in a weaker upward transport of natural carbon from the deep Subantarctic and Antarctic water masses. Likewise, the sub-surface correlations between DIC, temperature and salinity, their negative link in upwelling as well as their positive link in subduction regions further supports the connection to the MOC variability. Furthermore, Panassa et al. (2018) found that the summer mixed layer depth deepened by 2 m yr⁻¹ between 2002 and 2011 near the Subtropical Front, i.e. a region of outgassing in which we find sub-surface DIC positively correlates with surface pCO₂ and negatively with temperature. Thus, the observed changes in sub-surface DIC can again be linked to physical sub-surface processes.

Both the variability in the Southern Ocean MOC and the changes in mixed-layer depth have been linked to variability in the Southern Annular Mode (SAM), the dominant mode of climate variability in this region (DeVries et al., 2017; Marshall, 2003; Panassa et al., 2018). During positive phases in the SAM, the westerly winds strengthen and shift poleward (Hall and Visbeck, 2002), thus enhancing and shifting the MOC. Between 2004 and 2009, the SAM index polarity was low in comparison to the late 1990s and 2010s (Supplementary Information (Fig. C_SI.2. This may indicate further that a slower MOC caused the sub-surface reduction in DIC. Thus, our study provides further observation-based evidence to the study of DeVries et al. (2017) that the link between the strong variability in the Southern Ocean air-sea CO₂ flux (Keppler and Landschützer, 2019; Landschützer et al., 2015; Le Quéré et al., 2007) is linked to the MOC-driven changes in sub-surface DIC.

The link to the MOC and SAM, might, at first sight, appear contradictory to the findings by Keppler and Landschützer (2019), as these authors propose that trends in the SAM have a zero net effect on the overall contemporary air-sea CO₂ flux trends, whereas regional wind variability

drives the decadal sink trends (Gruber et al., 2019a; Keppler and Landschützer, 2019; Landschützer et al., 2015). While Keppler and Landschützer (2019) suggest the air-sea exchange remains unchanged with increasing index polarity of the SAM as enhanced outgassing in upwelling areas is counter-balanced by increasing uptake further north, it might nevertheless alter the DIC pool. As illustrated by DeVries et al. (2017), increasing strength in the MOC largely enhances the vertical transport of old DIC to the surface and likewise the subduction of new human-emitted carbon in the form of DIC further north at intermediate depths. Therefore, as a result of a slower MOC, the reduced outgassing of natural carbon and the reduced subduction of anthropogenic CO₂ balance at the surface and vice versa for a faster MOC. In the interior, however, and specifically at depth, the reduced upward transport is visible in the DIC pool.

One contributing factor we are unable to test is the role of biology as a potential driver of the sub-surface variability in DIC. A study by Gregor et al. (2018) suggests that a summer carbon draw-down in the Southern Ocean is the dominant driver for the seasonal pCO₂ variability at the surface. Biological uptake of carbon would indeed decrease both the pCO₂ as well as the DIC pool. Combined with circulation-driven changes in export production and remineralization, this might explain, at least in part, the DIC variability at depth. Other mechanisms that may play a role are freshening Antarctic Intermediate Waters and Subantarctic Mode Waters from 1982 through 2008 (Haumann et al., 2016). In general, the potential drivers of the Southern Ocean carbon variability are difficult to disentangle based on observations alone. Here our interpretation is therefore limited by the correlation-nature of our analysis.

We have now demonstrated for the first time based on observations, that substantial variations in the Southern Ocean Carbon cycle are visible in the interior oceanic DIC pool, providing additional evidence that the marine carbon sink is subject to considerable decadal variability. Our study illustrates that coinciding with the increasing air-sea CO₂ flux of the Southern Ocean in the 2000s, we find a decline in the interior DIC concentration. Likewise, the following sink stagnation coincides with an increasing DIC pool. Such a simultaneous decline in DIC and surface pCO₂, i.e. the dominant driver for the air-sea CO₂ exchange in the Southern Ocean (Landschützer et al., 2015), suggest that the proposed mechanisms are indeed related to circulation and/or biology as suggested by DeVries et al., 2017 and Gregor et al., 2018. Lacking essential biological proxy data at basin scale, a seasonally resolved analysis of the interior might shed light on the relative dominance of the processes driving the variability of the carbon cycle in the Southern Ocean. Additionally, Earth System Models provide a way forward as a capable tool to disentangle the driving factors.

Supplementary Information to Appendix C

C_SI. Time-mean of DIC in the Southern Ocean

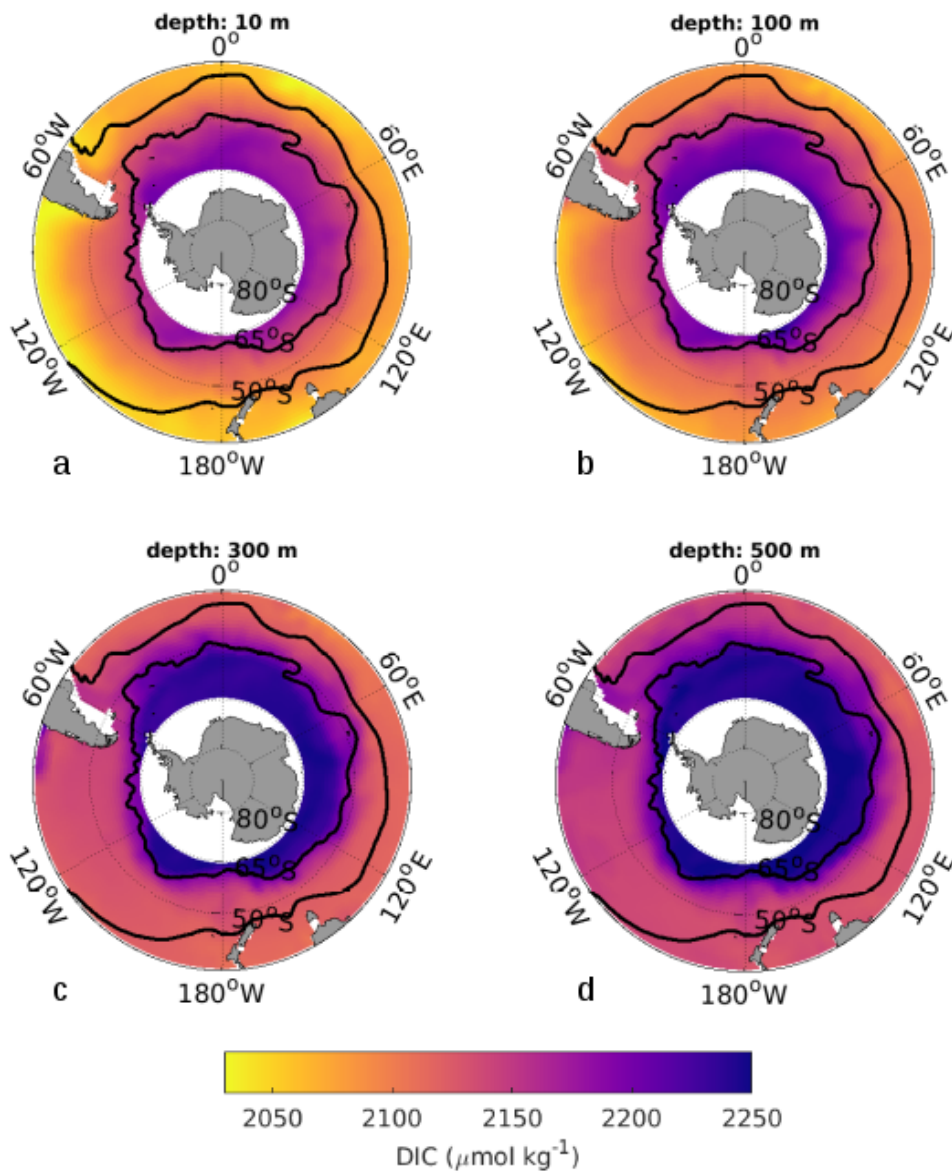


FIGURE C_SI.1: Time-mean spatial distribution DIC in the Southern Ocean on four different depth levels: 10 m (a), 100 m (b), 300 m (c), and 500 m (d). The Polar Front ($\sim 55^\circ$) and the Subtropical Front ($\sim 40^\circ$ S) from Orsi et al. (1995) are drawn as black lines.

C_S2. Timeline of the recent SAM

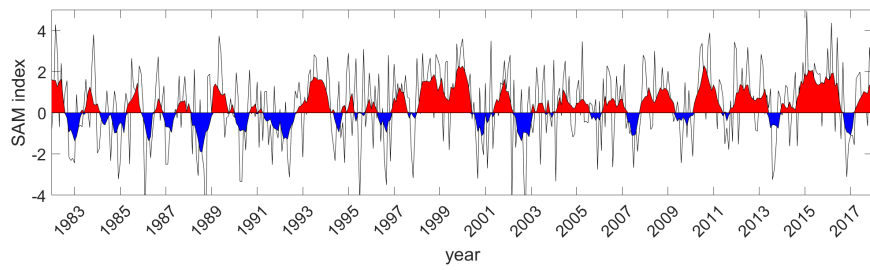


FIGURE C_SI.2: Timeline of the recent SAM index from Marshall (2003) (black line), smoothed with a 12-month running-mean (red/blue).

Bibliography

- Argo (2019). *Argo float data and metadata from Global Data Assembly Centre (Argo GDAC)*. type: dataset. DOI: 10.17882/42182.
- Bakker, D. C. E. et al. (2016). "A multi-decade record of high-quality fCO₂ data in version 3 of the Surface Ocean CO₂ Atlas (SOCAT)". In: *Earth System Science Data* 8.2, pp. 383–413. DOI: 10.5194/essd-8-383-2016.
- Bates, N. R., A. F. Michaels, and A. H. Knap (1996). "Seasonal and interannual variability of oceanic carbon dioxide species at the U.S. JGOFS Bermuda Atlantic Time-series Study (BATS) site". In: *Deep Sea Research Part II: Topical Studies in Oceanography* 43.2, pp. 347–383. DOI: 10.1016/0967-0645(95)00093-3.
- Bates, N. R. et al. (2014). "A Time-Series View of Changing Surface Ocean Chemistry Due to Ocean Uptake of Anthropogenic CO₂ and Ocean Acidification". In: *Oceanography* 27.1, pp. 126–141. DOI: 10.5670/oceanog.2014.16.
- Bittig, H. C. et al. (2018). "An Alternative to Static Climatologies: Robust Estimation of Open Ocean CO₂ Variables and Nutrient Concentrations From T, S, and O₂ Data Using Bayesian Neural Networks". In: *Frontiers in Marine Science* 5. DOI: 10.3389/fmars.2018.00328.
- Brewer, P. G. (1978). "Direct observation of the oceanic CO₂ increase". In: *Geophysical Research Letters* 5.12, pp. 997–1000. DOI: 10.1029/GL005i012p00997.
- Brix, H., N. Gruber, and C. D. Keeling (2004). "Interannual variability of the upper ocean carbon cycle at station ALOHA near Hawaii". In: *Global Biogeochemical Cycles* 18.4. DOI: 10.1029/2004GB002245.
- Bronselaer, B. et al. (2020). "Importance of wind and meltwater for observed chemical and physical changes in the Southern Ocean". In: *Nature Geoscience* 13.1, pp. 35–42. DOI: 10.1038/s41561-019-0502-8.
- Broullón, D. et al. (2019). "A global monthly climatology of total alkalinity: a neural network approach". In: *Earth System Science Data Discussions*, pp. 1–31. DOI: 10.5194/essd-2018-111.
- Bushinsky, S. M. et al. (2019). "Reassessing Southern Ocean Air-Sea CO₂ Flux Estimates With the Addition of Biogeochemical Float Observations". In: *Global Biogeochemical Cycles* 33.11, pp. 1370–1388. DOI: 10.1029/2019GB006176.
- Carter, B. R., R. A. Feely, N. L. Williams, A. G. Dickson, M. B. Fong, and Y. Takeshita (2018). "Updated methods for global locally interpolated estimation of alkalinity, pH, and nitrate". In: *Limnology and Oceanography: Methods* 16.2, pp. 119–131. DOI: 10.1002/lom3.10232.
- Chen, G.-T. and F. J. Millero (1979). "Gradual increase of oceanic CO₂". In: *Nature* 277.5693, pp. 205–206. DOI: 10.1038/277205a0.
- Ciais, P. et al. (2014). "Carbon and other biogeochemical cycles". In: *Climate Change 2013: The Physical Science Basis. Contribution of Working Group I to the Fifth Assessment Report of the Intergovernmental Panel on Climate Change*, pp. 465–570.
- Clement, D. and N. Gruber (2018). "The eMLR(C*) Method to Determine Decadal Changes in the Global Ocean Storage of Anthropogenic CO₂". In: *Global Biogeochemical Cycles* 32.4, pp. 654–679. DOI: 10.1002/2017GB005819.
- Deacon, E. L. (1977). "Gas transfer to and across an air-water interface". In: *Tellus* 29.4, pp. 363–374. URL: <https://onlinelibrary.wiley.com/doi/pdf/10.1111/j.2153-3490.1977.tb00746.x>.
- Dee, D. P. et al. (2011). "The ERA-Interim reanalysis: configuration and performance of the data assimilation system". In: *Quarterly Journal of the Royal Meteorological Society* 137.656, pp. 553–597. DOI: 10.1002/qj.828.

- DeVries, T. (2014). "The oceanic anthropogenic CO₂ sink: Storage, air-sea fluxes, and transports over the industrial era". In: *Global Biogeochemical Cycles* 28.7, pp. 631–647. DOI: 10.1002/2013GB004739.
- DeVries, T., M. Holzer, and F. Primeau (2017). "Recent increase in oceanic carbon uptake driven by weaker upper-ocean overturning". In: *Nature* 542.7640, pp. 215–218. DOI: 10.1038/nature21068.
- Dibike, Y. B. and P. Coulibaly (2006). "Temporal neural networks for downscaling climate variability and extremes". In: *Neural Networks. Earth Sciences and Environmental Applications of Computational Intelligence* 19.2, pp. 135–144. DOI: 10.1016/j.neunet.2006.01.003.
- Dickson, A. G., C. L. Sabine, J. R. Christian, C. P. Barger, and N. P. M. S. Organization, eds. (2007). *Guide to best practices for ocean CO₂ measurements*. PICES special publication no. 3. OCLC: ocn420872251. Sidney, BC: North Pacific Marine Science Organization. 1 p. ISBN: 978-1-897176-07-8.
- Doney, S. C., V. J. Fabry, R. A. Feely, and J. A. Kleypas (2009). "Ocean Acidification: The Other CO₂ Problem". In: *Annual Review of Marine Science* 1.1. Publisher: Annual Reviews, pp. 169–192. DOI: 10.1146/annurev.marine.010908.163834.
- Dore, J. E., R. Lukas, D. W. Sadler, M. J. Church, and D. M. Karl (2009). "Physical and biogeochemical modulation of ocean acidification in the central North Pacific". In: *Proceedings of the National Academy of Sciences of the United States of America* 106.30, pp. 12235–12240. DOI: 10.1073/pnas.0906044106.
- Dore, J. E., R. Lukas, D. W. Sadler, and D. M. Karl (2003). "Climate-driven changes to the atmospheric CO₂ sink in the subtropical North Pacific Ocean". In: *Nature* 424.6950, pp. 754–757. DOI: 10.1038/nature01885.
- Downes, S. M., A. S. Budnick, J. L. Sarmiento, and R. Farneti (2011). "Impacts of wind stress on the Antarctic Circumpolar Current fronts and associated subduction". In: *Geophysical Research Letters* 38.11. DOI: 10.1029/2011GL047668.
- Downes, S. M., N. L. Bindoff, and S. R. Rintoul (2009). "Impacts of Climate Change on the Subduction of Mode and Intermediate Water Masses in the Southern Ocean". In: *Journal of Climate* 22.12, pp. 3289–3302. DOI: 10.1175/2008JCLI2653.1.
- Emerson, S. and S. Bushinsky (2014). "Oxygen Concentrations and Biological Fluxes in the Open Ocean". In: *Oceanography* 27.1, pp. 168–171. DOI: 10.5670/oceanog.2014.20.
- Emerson, S., C. Stump, and D. Nicholson (2008). "Net biological oxygen production in the ocean: Remote in situ measurements of O₂ and N₂ in surface waters". In: *Global Biogeochemical Cycles* 22.3. DOI: 10.1029/2007GB003095.
- Feely, R. A. et al. (2006). "Decadal variability of the air-sea CO₂ fluxes in the equatorial Pacific Ocean". In: *Journal of Geophysical Research: Oceans* 111 (C8). DOI: 10.1029/2005JC003129.
- Fogt, R. L., J. M. Jones, and J. Renwick (2012). "Seasonal Zonal Asymmetries in the Southern Annular Mode and Their Impact on Regional Temperature Anomalies". In: *Journal of Climate* 25.18, pp. 6253–6270. DOI: 10.1175/JCLI-D-11-00474.1.
- Freeman, N. M., N. S. Lovenduski, and P. R. Gent (2016). "Temporal variability in the Antarctic Polar Front (2002-2014)". In: *Journal of Geophysical Research-Oceans* 121.10, pp. 7263–7276. DOI: 10.1002/2016JC012145.
- Friedlingstein, P. et al. (2019). "Global Carbon Budget 2019". In: *Earth System Science Data* 11.4, pp. 1783–1838. DOI: 10.5194/essd-11-1783-2019.
- Friis, K., A. Körtzinger, and D. W. R. Wallace (2003). "The salinity normalization of marine inorganic carbon chemistry data". In: *Geophysical Research Letters* 30.2. DOI: 10.1029/2002GL015898.
- Frölicher, T. L., J. L. Sarmiento, D. J. Paynter, J. P. Dunne, J. P. Krasting, and M. Winton (2015). "Dominance of the Southern Ocean in Anthropogenic Carbon and Heat Uptake in CMIP5 Models". In: *Journal of Climate* 28.2, pp. 862–886. DOI: 10.1175/JCLI-D-14-00117.1.
- Garcia, H. et al. (2019). *World Ocean Atlas 2018: Product Documentation*. Ed. by A. Mishonov.
- Gardner, M. W. and S. R. Dorling (1998). "Artificial neural networks (the multilayer perceptron)—a review of applications in the atmospheric sciences". In: *Atmospheric Environment* 32, pp. 2627–2636. DOI: 10.1016/S1352-2310(97)00447-0.

- Gevrey, M., I. Dimopoulos, and S. Lek (2003). "Review and comparison of methods to study the contribution of variables in artificial neural network models". In: *Ecological Modelling. Modelling the structure of aquatic communities: concepts, methods, and problems*. 160.3, pp. 249–264. DOI: 10.1016/S0304-3800(02)00257-0.
- Gray, A. R. et al. (2018). "Autonomous biogeochemical floats detect significant carbon dioxide outgassing in the high-latitude Southern Ocean". In: *Geophysical Research Letters* 0 (ja). DOI: 10.1029/2018GL078013.
- Gregor, L., S. Kok, and P. M. S. Monteiro (2018). "Interannual drivers of the seasonal cycle of CO₂ in the Southern Ocean". In: *Biogeosciences* 15.7, pp. 2361–2378. DOI: 10.5194/bg-15-2361-2018.
- Gruber, N., C. D. Keeling, and N. R. Bates (2002). "Interannual Variability in the North Atlantic Ocean Carbon Sink". In: *Science* 298.5602, p. 2374. DOI: 10.1126/science.1077077.
- Gruber, N., C. D. Keeling, and T. F. Stocker (1998). "Carbon-13 constraints on the seasonal inorganic carbon budget at the BATS site in the northwestern Sargasso Sea". In: *Deep Sea Research Part I: Oceanographic Research Papers* 45.4, pp. 673–717. DOI: 10.1016/S0967-0637(97)00098-8.
- Gruber, N., P. Landschützer, and N. S. Lovenduski (2019a). "The Variable Southern Ocean Carbon Sink". In: *Annual Review of Marine Science* 11.1, pp. 159–186. DOI: 10.1146/annurev-marine-121916-063407.
- Gruber, N., J. L. Sarmiento, and T. F. Stocker (1996). "An improved method for detecting anthropogenic CO₂ in the oceans". In: *Global Biogeochemical Cycles* 10.4, pp. 809–837. DOI: 10.1029/96GB01608.
- Gruber, N. et al. (2009). "Oceanic sources, sinks, and transport of atmospheric CO₂". In: *Global Biogeochemical Cycles* 23.1. DOI: 10.1029/2008GB003349.
- Gruber, N. et al. (2019b). "The oceanic sink for anthropogenic CO₂ from 1994 to 2007". In: *Science* 363.6432, pp. 1193–1199. DOI: 10.1126/science.aau5153.
- Hagan, M., H. Demuth, M. Beale, and O. De Jesús (2014). *Neural Network Design*. 2nd ed. ISBN: 978-0-9717321-1-7.
- Hall, A. and M. Visbeck (2002). "Synchronous variability in the southern hemisphere atmosphere, sea ice, and ocean resulting from the annular mode". In: *Journal of Climate* 15.21, pp. 3043–3057. DOI: 10.1175/1520-0442(2002)015<3043:SVITSH>2.0.CO;2.
- Hauk, J. and C. Voelker (2015). "Rising atmospheric CO₂ leads to large impact of biology on Southern Ocean CO₂ uptake via changes of the Revelle factor". In: *Geophysical Research Letters* 42.5, pp. 1459–1464. DOI: 10.1002/2015GL063070.
- Hauk, J., C. Völker, T. Wang, M. Hoppema, M. Losch, and D. A. Wolf-Gladrow (2013). "Seasonally different carbon flux changes in the Southern Ocean in response to the southern annular mode". In: *Global Biogeochemical Cycles* 27.4, pp. 1236–1245. DOI: 10.1002/2013GB004600.
- Haumann, F. A., N. Gruber, M. Munnich, I. Frenger, and S. Kern (2016). "Sea-ice transport driving Southern Ocean salinity and its recent trends". In: *Nature* 537.7618, pp. 89–92. DOI: 10.1038/nature19101.
- Heinze, C. et al. (2015). "The ocean carbon sink – impacts, vulnerabilities and challenges". In: *Earth System Dynamics* 6.1, pp. 327–358. DOI: 10.5194/esd-6-327-2015.
- Henry, W. and J. Banks (1803). "III. Experiments on the quantity of gases absorbed by water, at different temperatures, and under different pressures". In: *Philosophical Transactions of the Royal Society of London* 93, pp. 29–274. DOI: 10.1098/rstl.1803.0004.
- Heuven, S. van, D. Pierrot, J. Rae, E. Lewis, and D. Wallace (2011). *MATLAB Program Developed for CO₂ System Calculations*. Oak Ridge, Tennessee.
- Hobbs, W. R. and M. N. Raphael (2010). "Characterizing the zonally asymmetric component of the SH circulation". In: *Climate Dynamics* 35.5, pp. 859–873. DOI: 10.1007/s00382-009-0663-z.
- Holte, J., L. D. Talley, J. Gilson, and D. Roemmich (2017). "An Argo mixed layer climatology and database". In: *Geophysical Research Letters* 44.11, 2017GL073426. DOI: 10.1002/2017GL073426.

- Hornik, K., M. Stinchcombe, and H. White (1989). "Multilayer feedforward networks are universal approximators". In: *Neural Networks* 2.5, pp. 359–366. DOI: 10.1016/0893-6080(89)90020-8.
- Hsieh, W. W. (2009). *Machine learning methods in the environmental sciences : neural networks and kernels* /. Cambridge ; Cambridge University Press, ISBN: 978-0-521-79192-2.
- Ilyina, T., K. D. Six, J. Segschneider, E. Maier-Reimer, H. Li, and I. Núñez-Riboni (2013). "Global ocean biogeochemistry model HAMOCC: Model architecture and performance as component of the MPI-Earth system model in different CMIP5 experimental realizations". In: *Journal of Advances in Modeling Earth Systems* 5.2, pp. 287–315. DOI: 10.1029/2012MS000178.
- IPCC (2013). *Climate Change 2013: The Physical Science Basis. Contribution of Working Group I to the Fifth Assessment Report of the Intergovernmental Panel on Climate Change*. Cambridge University Press, Cambridge, United Kingdom and New York, NY, USA. 1535 pp. URL: <https://www.ipcc.ch/report/ar5/wg1/>.
- Jenkins, W. J. and J. C. Goldman (1985). "Seasonal oxygen cycling and primary production in the Sargasso Sea". In: *J. Mar. Res* 43, 465–491.
- Jones, S. D., C. Le Quéré, C. Rödenbeck, A. C. Manning, and A. Olsen (2015). "A statistical gap-filling method to interpolate global monthly surface ocean carbon dioxide data". In: *Journal of Advances in Modeling Earth Systems* 7.4, pp. 1554–1575. DOI: 10.1002/2014MS000416.
- Juranek, L. W., P. D. Quay, R. A. Feely, D. Lockwood, D. M. Karl, and M. J. Church (2012). "Biological production in the NE Pacific and its influence on air-sea CO₂ flux: Evidence from dissolved oxygen isotopes and O₂/Ar". In: *Journal of Geophysical Research: Oceans* 117 (C5). DOI: 10.1029/2011JC007450.
- Kalnay, E. et al. (1996). "The NCEP/NCAR 40-Year Reanalysis Project". In: *Bulletin of the American Meteorological Society* 77.3, pp. 437–472. DOI: 10.1175/1520-0477(1996)077<0437:TNYRP>2.0.CO;2.
- Keeling, C. D. (1993). "NATO Lecture 2: Surface Ocean CO₂". In: *The Global Carbon Cycle*. Tokyo: Springer, pp. 413–429. URL: <https://www.springer.com/de/book/9783642846106>.
- Keeling, C. D., H. Brix, and N. Gruber (2004). "Seasonal and long-term dynamics of the upper ocean carbon cycle at Station ALOHA near Hawaii". In: *Global Biogeochemical Cycles* 18.4. DOI: 10.1029/2004GB002227.
- Keppler, L. and P. Landschützer (2019). "Regional Wind Variability Modulates the Southern Ocean Carbon Sink". In: *Scientific Reports* 9.1, pp. 1–10. DOI: 10.1038/s41598-019-43826-y.
- Keppler, L., P. Landschützer, N. Gruber, S. K. Lauvset, and I. Stemmler (in review). "Seasonal carbon dynamics in the global ocean based on a neural network mapping of observations". In: *Global Biogeochemical Cycles*.
- Key, R. et al. (2015). *Global Ocean Data Analysis Project, Version 2 (GLODAPv2), ORNL/CDIAC-162, ND-P093*. type: dataset. DOI: 10.3334/CDIAC/OTG.NDP093_GLODAPv2.
- Khatiwala, S., F. Primeau, and T. Hall (2009). "Reconstruction of the history of anthropogenic CO₂ concentrations in the ocean". In: *Nature* 462.7271, 346–U110. DOI: 10.1038/nature08526.
- Kohonen, T. (1989). *Self-organization and Associative Memory: 3rd Edition*. Berlin, Heidelberg: Springer-Verlag. ISBN: 978-0-387-51387-4.
- Kohonen, T. (2001). *Self-Organizing Maps*. 3rd ed. Springer Series in Information Sciences. Berlin Heidelberg: Springer-Verlag. ISBN: 978-3-540-67921-9.
- Kwiatkowski, L., O. Aumont, L. Bopp, and P. Ciais (2018). "The Impact of Variable Phytoplankton Stoichiometry on Projections of Primary Production, Food Quality, and Carbon Uptake in the Global Ocean". In: *Global Biogeochemical Cycles* 32.4, pp. 516–528. DOI: 10.1002/2017GB005799.
- Körtzinger, A. et al. (2008). "The seasonal pCO₂ cycle at 49°N/16.5°W in the northeastern Atlantic Ocean and what it tells us about biological productivity". In: *Journal of Geophysical Research: Oceans* 113 (C4). DOI: 10.1029/2007JC004347.

- Landschützer, P., N. Gruber, D. C. E. Bakker, and U. Schuster (2014). "Recent variability of the global ocean carbon sink". In: *Global Biogeochemical Cycles* 28.9, pp. 927–949. DOI: 10.1002/2014GB004853.
- Landschützer, P. et al. (2013). "A neural network-based estimate of the seasonal to inter-annual variability of the Atlantic Ocean carbon sink". In: *Biogeosciences* 10.11, pp. 7793–7815. DOI: 10.5194/bg-10-7793-2013.
- Landschützer, P., N. Gruber, and D. C. E. Bakker (2016). "Decadal variations and trends of the global ocean carbon sink". In: *Global Biogeochemical Cycles* 30.10, pp. 1396–1417. DOI: 10.1002/2015GB005359.
- Landschützer, P., N. Gruber, D. C. E. Bakker, I. Stemmler, and K. D. Six (2018). "Strengthening seasonal marine CO₂ variations due to increasing atmospheric CO₂". In: *Nature Climate Change*, p. 1. DOI: 10.1038/s41558-017-0057-x.
- Landschützer, P. et al. (2015). "The reinvigoration of the Southern Ocean carbon sink". In: *Science* 349.6253, pp. 1221–1224. DOI: 10.1126/science.aab2620.
- Lauvset, S. K. et al. (2016). "A new global interior ocean mapped climatology: the 1° × 1° GLODAP version 2". In: *Earth System Science Data* 8.2, pp. 325–340. DOI: 10.5194/essd-8-325-2016.
- Le Quéré, C. et al. (2007). "Saturation of the Southern Ocean CO₂ sink due to recent climate change". In: *Science* 316.5832, pp. 1735–1738. DOI: 10.1126/science.1136188.
- Le Quéré, C. et al. (2018). "Global Carbon Budget 2017". In: *Earth System Science Data* 10.1, pp. 405–448. DOI: 10.5194/essd-10-405-2018.
- Lee, K. (2001). "Global net community production estimated from the annual cycle of surface water total dissolved inorganic carbon". In: *Limnology and Oceanography* 46.6, pp. 1287–1297. ISSN: 1939-5590. DOI: 10.4319/lo.2001.46.6.1287.
- Lenton, A. et al. (2013). "Sea-air CO₂ fluxes in the Southern Ocean for the period 1990-2009". In: *Biogeosciences* 10.6, pp. 4037–4054. DOI: 10.5194/bg-10-4037-2013.
- Lenton, A. and R. J. Matear (2007). "Role of the Southern Annular Mode (SAM) in Southern Ocean CO₂ uptake". In: *Global Biogeochemical Cycles* 21.2, GB2016. DOI: 10.1029/2006GB002714.
- Levenberg, K. (1944). "A method for the solution of certain non-linear problems in least squares". In: *Quarterly of Applied Mathematics* 2.2, pp. 164–168. DOI: 10.1090/qam/10666.
- Loon, H. van and R. L. Jenne (1972). "The zonal harmonic standing waves in the southern hemisphere". In: *Journal of Geophysical Research (1896-1977)* 77.6, pp. 992–1003. DOI: 10.1029/JC077i006p00992.
- Lovenduski, N. S., A. R. Fay, and G. A. McKinley (2015). "Observing multidecadal trends in Southern Ocean CO₂ uptake: What can we learn from an ocean model?" In: *Global Biogeochemical Cycles* 29.4, pp. 416–426. DOI: 10.1002/2014GB004933.
- Lovenduski, N. S., N. Gruber, and S. C. Doney (2008). "Toward a mechanistic understanding of the decadal trends in the Southern Ocean carbon sink". In: *Global Biogeochemical Cycles* 22.3, GB3016. DOI: 10.1029/2007GB003139.
- Lovenduski, N. S., N. Gruber, S. C. Doney, and I. D. Lima (2007). "Enhanced CO₂ outgassing in the Southern Ocean from a positive phase of the Southern Annular Mode". In: *Global Biogeochemical Cycles* 21.2, GB2026. DOI: 10.1029/2006GB002900.
- Marquardt, D. W. (1963). "An Algorithm for Least-Squares Estimation of Nonlinear Parameters". In: *Journal of the Society for Industrial and Applied Mathematics* 11.2, pp. 431–441.
- Marshall, G. J. (2003). "Trends in the Southern Annular Mode from Observations and Reanalyses". In: *Journal of Climate* 16.24, pp. 4134–4143. DOI: 10.1175/1520-0442(2003)016<4134:TITSAM>2.0.CO;2.
- Mauritsen, T. et al. (2019). "Developments in the MPI-M Earth System Model version 1.2 (MPI-ESM1.2) and Its Response to Increasing CO₂". In: *Journal of Advances in Modeling Earth Systems* 11.4, pp. 998–1038. DOI: 10.1029/2018MS001400.
- McNeil, B. I. and K. Matsumoto (2019). "1 - The changing ocean and freshwater CO₂ system". In: *Fish Physiology*. Ed. by M. Grosell, P. L. Munday, A. P. Farrell, and C. J. Brauner. Vol. 37. Carbon Dioxide. Academic Press, pp. 1–32. DOI: 10.1016/bs.fp.2019.10.001.
- McNeil, B. I. and T. P. Sasse (2016). "Future ocean hypercapnia driven by anthropogenic amplification of the natural CO₂ cycle". In: *Nature* 529.7586, pp. 383–386. DOI: 10.1038/nature16156.

- Michaels, A. F., N. R. Bates, K. O. Buesseler, C. A. Carlson, and A. H. Knap (1994). "Carbon-cycle imbalances in the Sargasso Sea". In: *Nature* 372.6506, pp. 537–540. DOI: 10.1038/372537a0.
- Mikaloff Fletcher, S. E. M. et al. (2006). "Inverse estimates of anthropogenic CO₂ uptake, transport, and storage by the ocean". In: *Global Biogeochemical Cycles* 20.2, GB2002. DOI: 10.1029/2005GB002530.
- Mongwe, N. P., M. Vichi, and P. M. S. Monteiro (2018). "The seasonal cycle of pCO₂ and CO₂ fluxes in the Southern Ocean: diagnosing anomalies in CMIP5 Earth system models". In: *Biogeosciences* 15.9, pp. 2851–2872. DOI: 10.5194/bg-15-2851-2018.
- Morel, A., Y. Huot, B. Gentili, P. J. Werdell, S. B. Hooker, and B. A. Franz (2007). "Examining the consistency of products derived from various ocean color sensors in open ocean (Case 1) waters in the perspective of a multi-sensor approach". In: *Remote Sensing of Environment* 111.1, pp. 69–88. DOI: 10.1016/j.rse.2007.03.012.
- Najjar, R. G. and R. F. Keeling (1997). *Analysis of the mean annual cycle of the dissolved oxygen anomaly in the World Ocean*. DOI: info:doi/10.1357/0022240973224481.
- Nevison, C. D. et al. (2016). "Evaluating CMIP5 ocean biogeochemistry and Southern Ocean carbon uptake using atmospheric potential oxygen: Present-day performance and future projection". In: *Geophysical Research Letters* 43.5, pp. 2077–2085. DOI: 10.1002/2015GL067584.
- Olden, J. D. and D. A. Jackson (2002). "Illuminating the "black box": a randomization approach for understanding variable contributions in artificial neural networks". In: *Ecological Modelling* 154.1, pp. 135–150. DOI: 10.1016/S0304-3800(02)00064-9.
- Olsen, A. et al. (2019). "GLODAPv2.2019 – an update of GLODAPv2". In: *Earth System Science Data Discussions*, pp. 1–39. DOI: 10.5194/essd-2019-66.
- Orsi, A. H., T. Whitworth, and W. D. Nowlin (1995). "On the Meridional Extent and Fronts of the Antarctic Circumpolar Current". In: *Deep-Sea Research Part I-Oceanographic Research Papers* 42.5, pp. 641–673. DOI: 10.1016/0967-0637(95)00021-w.
- Ostle, C. et al. (2015). "Net community production in the North Atlantic Ocean derived from Volunteer Observing Ship data". In: *Global Biogeochemical Cycles* 29.1, pp. 80–95. DOI: 10.1002/2014GB004868.
- O'Kane, T. J., R. J. Matear, M. A. Chamberlain, J. S. Risbey, B. M. Sloyan, and I. Horenko (2013). "Decadal variability in an OGCM Southern Ocean: Intrinsic modes, forced modes and metastable states". In: *Ocean Modelling* 69, pp. 1–21. DOI: 10.1016/j.ocemod.2013.04.009.
- Panassa, E. et al. (2018). "Variability of nutrients and carbon dioxide in the Antarctic Intermediate Water between 1990 and 2014". In: *Ocean Dynamics* 68.3, pp. 295–308. DOI: 10.1007/s10236-018-1131-2.
- Pearl, J. (2016). *Causal Inference in Statistics - A Primer*. 1. Chichester, West Sussex: Wiley. 156 pp. ISBN: 978-1-119-18684-7.
- Plant, J. N. et al. (2016). "Net community production at Ocean Station Papa observed with nitrate and oxygen sensors on profiling floats". In: *Global Biogeochemical Cycles* 30.6, pp. 859–879. DOI: 10.1002/2015GB005349.
- Pope, A., P. Wagner, R. Johnson, J. Shutler, J. Baeseman, and L. Newman (2017). "Community review of Southern Ocean satellite data needs". In: *Antarctic Science* 29.2, pp. 97–138. DOI: 10.1017/S0954102016000390.
- Quay, P., J. Stutsman, and T. Steinhoff (2012). "Primary production and carbon export rates across the subpolar N. Atlantic Ocean basin based on triple oxygen isotope and dissolved O₂ and Ar gas measurements". In: *Global Biogeochemical Cycles* 26.2. DOI: 10.1029/2010GB004003.
- Quay, P. and J. Stutsman (2003). "Surface layer carbon budget for the subtropical N. Pacific: $\delta^{13}\text{C}$ constraints at station ALOHA". In: *Deep Sea Research Part I: Oceanographic Research Papers* 50.9, pp. 1045–1061. DOI: 10.1016/S0967-0637(03)00116-X.
- Quintanar, A. I. and C. R. Mechoso (1995). "Quasi-Stationary Waves in the Southern Hemisphere. Part I: Observational Data". In: *Journal of Climate* 8.11, pp. 2659–2672.
- Raphael, M. N. (2004). "A zonal wave 3 index for the Southern Hemisphere". In: *Geophysical Research Letters* 31.23. DOI: 10.1029/2004GL020365.

- Reichstein, M. et al. (2019). "Deep learning and process understanding for data-driven Earth system science". In: *Nature* 566.7743, p. 195. DOI: 10.1038/s41586-019-0912-1.
- Resplandy, L. et al. (2018). "Revision of global carbon fluxes based on a reassessment of oceanic and riverine carbon transport". In: *Nature Geoscience*, p. 1. DOI: 10.1038/s41561-018-0151-3.
- Rintoul, S. R. (2018). "The global influence of localized dynamics in the Southern Ocean". In: *Nature* 558.7709, pp. 209–218. DOI: 10.1038/s41586-018-0182-3.
- Rintoul, S. R., M. P. Meredith, O. Schofield, and L. Newman (2012). "The Southern Ocean Observing System". In: *Oceanography* 25. DOI: 10.5670/oceanog.2012.76.
- Riser, S. C. and K. S. Johnson (2008). "Net production of oxygen in the subtropical ocean". In: *Nature* 451.7176, pp. 323–325. DOI: 10.1038/nature06441.
- Ritter, R. et al. (2017). "Observation-Based Trends of the Southern Ocean Carbon Sink". In: *Geophysical Research Letters* 44. DOI: 10.1002/2017GL074837.
- Rodgers, K. B., O. Aumont, C. Menkes, and T. Gorgues (2008). "Decadal variations in equatorial Pacific ecosystems and ferrocline/pycnocline decoupling". In: *Global Biogeochemical Cycles* 22.2. DOI: 10.1029/2006GB002919.
- Roemmich, D., J. Church, J. Gilson, D. Monselesan, P. Sutton, and S. Wijffels (2015). "Unabated planetary warming and its ocean structure since 2006". In: *Nature Climate Change* 5.3, pp. 240–245. DOI: 10.1038/NCLIMATE2513.
- Roemmich, D. and J. Gilson (2009). "The 2004-2008 mean and annual cycle of temperature, salinity, and steric height in the global ocean from the Argo Program". In: *Progress in Oceanography* 82.2, pp. 81–100. DOI: 10.1016/j.pocean.2009.03.004.
- Roobaert, A., G. G. Laruette, P. Landschützer, N. Gruber, L. Chou, and P. Regnier (2019). "The Spatiotemporal Dynamics of the Sources and Sinks of CO₂ in the Global Coastal Ocean". In: *Global Biogeochemical Cycles* 33.12, pp. 1693–1714. DOI: 10.1029/2019GB006239.
- Rödenbeck, C. et al. (2015). "Data-based estimates of the ocean carbon sink variability – first results of the Surface Ocean pCO₂ Mapping intercomparison (SOCOM)". In: *Biogeosciences* 12.23, pp. 7251–7278. DOI: 10.5194/bg-12-7251-2015.
- Sabine, C. L. et al. (2004). "The oceanic sink for anthropogenic CO₂". In: *Science* 305.5682, pp. 367–371. DOI: 10.1126/science.1097403.
- Sabine, C. L. et al. (2013). "Surface Ocean CO₂ Atlas (SOCAT) gridded data products". In: p. 9.
- Sabine, C. L. and T. Tanhua (2010). "Estimation of anthropogenic CO₂ inventories in the ocean". In: *Annual Review of Marine Science* 2, pp. 175–198. DOI: 10.1146/annurev-marine-120308-080947.
- Sallée, J.-B., R. J. Matear, S. R. Rintoul, and A. Lenton (2012). "Localized subduction of anthropogenic carbon dioxide in the Southern Hemisphere oceans". In: *Nature Geoscience* 5.8, pp. 579–584. DOI: 10.1038/NGE01523.
- Sallée, J.-B., K. G. Speer, and S. R. Rintoul (2010). "Zonally asymmetric response of the Southern Ocean mixed-layer depth to the Southern Annular Mode". In: *Nature Geoscience* 3.4, pp. 273–279. DOI: 10.1038/NGE0812.
- Sarmiento, J. L. and N. Gruber (2006). "Carbon Cycle, CO₂, and Climate; the Anthropogenic Perturbation". In: *Ocean Biogeochemical Dynamics*. Princeton University Press, pp. 399–417. ISBN: 978-0-691-01707-5.
- Sasse, T. P., B. I. McNeil, and G. Abramowitz (2013). "A new constraint on global air-sea CO₂ fluxes using bottle carbon data". In: *Geophysical Research Letters* 40.8, pp. 1594–1599. DOI: 10.1002/grl.50342.
- Sauzède, R. et al. (2017). "Estimates of Water-Column Nutrient Concentrations and Carbonate System Parameters in the Global Ocean: A Novel Approach Based on Neural Networks". In: *Frontiers in Marine Science* 4. DOI: 10.3389/fmars.2017.00128.
- Schlosser, E., F. A. Haumann, and M. N. Raphael (2018). "Atmospheric influences on the anomalous 2016 Antarctic sea ice decay". In: *The Cryosphere* 12.3, pp. 1103–1119. DOI: 10.5194/tc-12-1103-2018.
- Takahashi, T. et al. (2002). "Global sea-air CO₂ flux based on climatological surface ocean pCO₂, and seasonal biological and temperature effects". In: *Deep-Sea Research Part II-Topical Studies in Oceanography* 49.9, pp. 1601–1622. DOI: 10.1016/S0967-0645(02)00003-6.

- Takahashi, T., J. Olafsson, J. G. Goddard, D. W. Chipman, and S. C. Sutherland (1993). "Seasonal variation of CO₂ and nutrients in the high-latitude surface oceans: A comparative study". In: *Global Biogeochemical Cycles* 7.4, pp. 843–878. DOI: 10.1029/93GB02263.
- Takahashi, T. et al. (1997). "Global air-sea flux of CO₂: An estimate based on measurements of sea-air pCO₂ difference". In: *Proceedings of the National Academy of Sciences* 94.16, pp. 8292–8299. DOI: 10.1073/pnas.94.16.8292.
- Takahashi, T. et al. (2009). "Climatological mean and decadal change in surface ocean pCO₂, and net sea-air CO₂ flux over the global oceans". In: *Deep-Sea Research Part II-Topical Studies in Oceanography* 56.8, pp. 554–577. DOI: 10.1016/j.dsr2.2008.12.009.
- Talley, L. et al. (2016). "Changes in Ocean Heat, Carbon Content, and Ventilation: A Review of the First Decade of GO-SHIP Global Repeat Hydrography". In: *Annual Review of Marine Science* 8.1, pp. 185–215. DOI: 10.1146/annurev-marine-052915-100829.
- Talley, L. D., G. L. Pickard, W. J. Emery, and J. H. Swift (2011). *Descriptive Physical Oceanography*. Elsevier. ISBN: 978-0-7506-4552-2.
- Thompson, D. W. J. and S. Solomon (2002). "Interpretation of recent Southern Hemisphere climate change". In: *Science* 296.5569, pp. 895–899. DOI: 10.1126/science.1069270.
- Thompson, D. W. J. and J. M. Wallace (2000). "Annular modes in the extratropical circulation. Part I: Month-to-month variability". In: *Journal of Climate* 13.5, pp. 1000–1016. DOI: 10.1175/1520-0442(2000)013<1000:AMITEC>2.0.CO;2.
- Thompson, D. W. J., J. M. Wallace, and G. C. Hegerl (2000). "Annular modes in the extratropical circulation. Part II: Trends". In: *Journal of Climate* 13.5, pp. 1018–1036. DOI: 10.1175/1520-0442(2000)013<1018:AMITEC>2.0.CO;2.
- Trull, T., S. R. Rintoul, M. Hadfield, and E. R. Abraham (2001). "Circulation and seasonal evolution of polar waters south of Australia: Implications for iron fertilization of the Southern Ocean". In: *Deep-Sea Research Part II-Topical Studies in Oceanography* 48.11, pp. 2439–2466. DOI: 10.1016/S0967-0645(01)00003-0.
- Velo, A., F. F. Pérez, T. Tanhua, M. Gilcoto, A. F. Ríos, and R. M. Key (2013). "Total alkalinity estimation using MLR and neural network techniques". In: *Journal of Marine Systems* 111–112, pp. 11–18. DOI: 10.1016/j.jmarsys.2012.09.002.
- Verdy, A. and M. R. Mazloff (2017). "A data assimilating model for estimating Southern Ocean biogeochemistry". In: *Journal of Geophysical Research: Oceans* 122.9, pp. 6968–6988. DOI: 10.1002/2016JC012650.
- Vesanto, J., J. Himberg, E. Alhoniemi, and J. Antonov (2000). *SOM Toolbox for Matlab* 5. A57. SOM Toolbox Team, Helsinki University of Technology, Finland.
- Wanninkhof, R. (1992). "Relationship between wind speed and gas exchange over the ocean". In: *Journal of Geophysical Research: Oceans* 97 (C5), pp. 7373–7382. DOI: 10.1029/92JC00188.
- Wanninkhof, R. et al. (2013). "Global ocean carbon uptake: magnitude, variability and trends". In: *Biogeosciences* 10.3, pp. 1983–2000. DOI: 10.5194/bg-10-1983-2013.
- Williams, N. L. et al. (2017). "Calculating surface ocean pCO₂ from biogeochemical Argo floats equipped with pH: An uncertainty analysis". In: *Global Biogeochemical Cycles* 31.3, pp. 591–604. DOI: 10.1002/2016GB005541.
- Wu, Y., M. P. Hain, M. P. Humphreys, S. Hartman, and T. Tyrrell (2019). "What drives the latitudinal gradient in open-ocean surface dissolved inorganic carbon concentration?" In: *Biogeosciences* 16.13, pp. 2661–2681. DOI: 10.5194/bg-16-2661-2019.
- Xue, L. et al. (2018). "Climatic modulation of surface acidification rates through summertime wind forcing in the Southern Ocean". In: *Nature Communications* 9.1, p. 3240. DOI: 10.1038/s41467-018-05443-7.
- Zeebe, R. and D. Wolf-Gladrow (2001). *CO₂ in Seawater: Equilibrium, Kinetics, Isotopes*. ISBN: 978-0-444-50946-8.
- Zeng, J., Y. Nojiri, P. Landschützer, M. Telszewski, and S. Nakaoka (2014). "A Global Surface Ocean fCO₂ Climatology Based on a Feed-Forward Neural Network". In: *Journal of Atmospheric and Oceanic Technology* 31.8, pp. 1838–1849. DOI: 10.1175/JTECH-D-13-00137.1.
- Zickfeld, K., J. C. Fyfe, O. A. Saenko, M. Eby, and A. J. Weaver (2007). "Response of the global carbon cycle to human-induced changes in Southern Hemisphere winds". In: *Geophysical Research Letters* 34.12. DOI: 10.1029/2006GL028797.

Declaration of Oath

Versicherung an Eides statt

Hiermit versichere ich an Eides statt, dass ich die vorliegende Dissertation mit dem Titel: "Variability of the Contemporary Southern Ocean Carbon Fluxes and Storage" selbstständig verfasst und keine anderen als die angegebenen Hilfsmittel – insbesondere keine im Quellenverzeichnis nicht benannten Internet-Quellen – benutzt habe. Alle Stellen, die wörtlich oder sinngemäß aus Veröffentlichungen entnommen wurden, sind als solche kenntlich gemacht. Ich versichere weiterhin, dass ich die Dissertation oder Teile davon vorher weder im In- noch im Ausland in einem anderen Prüfungsverfahren eingereicht habe und die eingereichte schriftliche Fassung der auf dem elektronischen Speichermedium entspricht.

Hamburg, den 04.03.2020

Lydia Keppler

Hinweis / Reference

Die gesamten Veröffentlichungen in der Publikationsreihe des MPI-M
„Berichte zur Erdsystemforschung / Reports on Earth System Science“,
ISSN 1614-1199

sind über die Internetseiten des Max-Planck-Instituts für Meteorologie erhältlich:
<http://www.mpimet.mpg.de/wissenschaft/publikationen.html>

*All the publications in the series of the MPI -M
„Berichte zur Erdsystemforschung / Reports on Earth System Science“,
ISSN 1614-1199*

*are available on the website of the Max Planck Institute for Meteorology:
<http://www.mpimet.mpg.de/wissenschaft/publikationen.html>*

